TU Delft

DIMPLE

Turbulent flow over liquid-infused superhydrophobic surfaces

An experimental investigation into the drag performance and flow mechanics

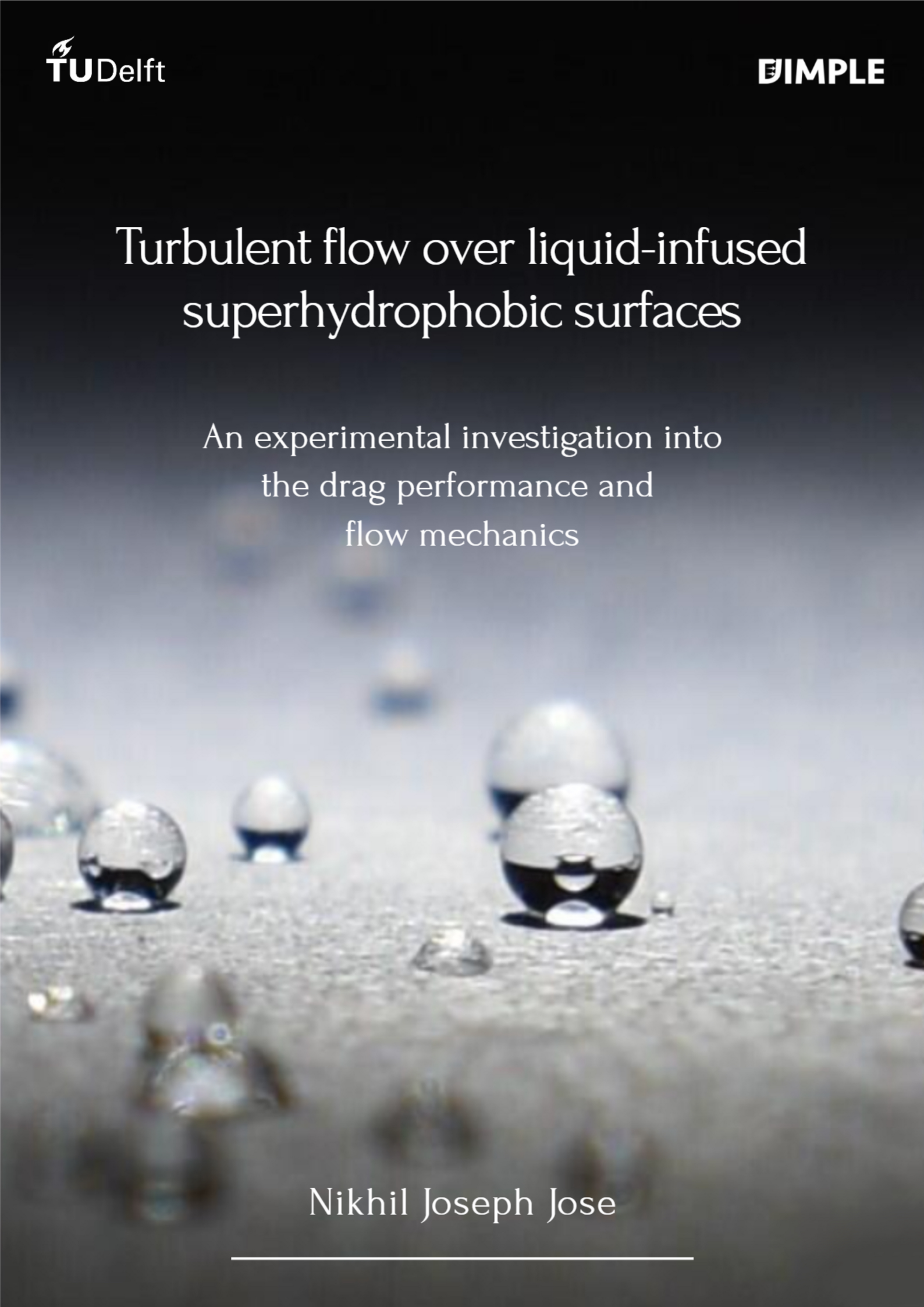

Nikhil Joseph Jose

Turbulent flow over liquid-infused superhydrophobic surfaces

An experimental investigation into the drag performance and flow mechanics

Master of Science Thesis

by

N. J. (Nikhil) Jose

in partial fulfilment of the requirements for the degree of

Master of Science
in Aerospace Engineering

at the Delft University of Technology

To be defended on Tuesday, February 28 at 09:30

Student number:	5321913	
Thesis committee:	Dr. ir. B. W. (Bas) van Oudheusden	Delft University of Technology
	Dr. ir. F. F. J. (Ferry) Schrijer	Delft University of Technology
	Dr. D. (Daniele) Ragni	Delft University of Technology
	ir. M. (Michiel) van Nesselrooij	Dimple Aerospace B.V.

TU Delft DIMPLE

Delft University of Technology

Faculty of Aerospace Engineering
Department of Flow Physics and Technology

The undersigned hereby certify that they have read and recommend to the Faculty of Aerospace Engineering for acceptance the thesis titled **Turbulent flow over liquid-infused superhydrophobic surfaces** by **N. J. (Nikhil) Jose** in partial fulfilment of the requirements for the degree of **Master of Science** in **Aerospace Engineering**.

Dated: February 28, 2023

Chair of supervisory committee:

Dr. ir. B. W. (Bas) van Oudheusden

Supervisors:

Dr. ir. F. F. J. (Ferry) Schrijer

ir. M. (Michiel) van Nesselrooij

Reader:

Dr. D. (Daniele) Ragni

Preface

This work signifies not just the end of an exciting period of research but a wonderful two and a half years at TU Delft, and there are a tonne of people without whom I could not have made the journey.

Firstly, I must thank my family. Without my parents' belief that I should follow my dreams, I wouldn't have even been here. Their faith in me throughout this period has been unwavering. My younger brother always found ways to keep our calls entertaining and reminded me often that I was the favourite child. Along with them, the love and support from my grandparents, cousins, aunts and uncles who kept in touch reminded me of the number of people cheering me on.

With regards to my thesis, I would first like to thank Michiel van Nesselrooij, my daily supervisor at Dimple Aerospace. Michiel was present every step of the way, and diligently knew when to let me make decisions and when I needed a spark or a bit of a push. I would also like to thank Professors Bas and Ferry, my supervisors at the university, for their their approachability and subject matter expertise. The important deliberation points that they raised during our update meetings kept my work going in the right direction. Coming back to the team at Dimple, I am deeply obliged to Olaf van Campenhout. His contagious enthusiasm is what attracted me to performing this thesis and the trip to NLR's facilities in Marknesse is one that I will cherish. I am grateful to Friso for setting the benchmark for us students on how elegantly research can be carried out, and for assisting me with the setup and post-processing of the PIV test. I would also like to thank Julio, Sahana, Bastiaan, Max, Bharadwaj, Wouter and Jop for the shared time in the wind tunnel and the discussions we've had over lunch and immeasurable litres of coffee.

The execution of the experimental part of this work would not have been possible without the contributions of the technical staff at the Low Speed and High Speed Laboratories of TU Delft. In particular, I am grateful to Emiel, Stefan and Frits for their assistance with the setup of the campaigns and the preparation of the surfaces. I would also like to give a shout-out to Miisa for helping me carry out contact angle measurements at the Delft Aerospace Structures and Materials Laboratory.

Next, I wish to thank my friends and classmates for keeping my spirits up. From my boys who celebrated my highs and took care of me during my lows, to my classmates with whom I discussed aerodynamic theories, the F1 fanatics with whom I rooted for Seb, the foodies with whom I cooked delicious dishes, the travellers with whom I saw glimpses into the beauty of this country, and the ones who partied like there was no tomorrow, I owe several of my happiest days here to them. I am also deeply indebted to my friends back home in India. Their regular calls and texts to check in on me showed me that distance and annoying time zone differences were not an issue for the people who truly value you.

I cannot miss mentioning my teammates at Formula Student Team Delft, where I worked part-time alongside my thesis. Designing and building the DUT22 was a project that I found a deep passion in, and this kept me going on the days when my progress with the thesis wasn't going favourably. The amazing Aero team, the time spent in the lamination and CNC rooms, the road trips to Austria and Germany and the competitions themselves - these are all core memories for me. Ahoo!

I know that there are more folks who deserve a word of appreciation, but to them and everyone listed above, I look forward to the day when I can meet you in person, embrace you and introduce myself as an *ingenieur*. Until then, I will leave you with my favourite quote from the TV series *The Good Place*:

> *I'll say this to you, my friend, with all the love in my heart and all the wisdom of the universe:*
> *Take it sleazy.*

Nikhil Joseph Jose
Delft, February 17, 2023

Abstract

Surfaces that induce slip at the wall have been shown to reduce skin friction drag in the turbulent regime. One approach is through superhydrophobic surfaces (SHSs), which use air trapped in random or organised roughness elements to create slip, thereby reducing the velocity gradient at the fluid-fluid interface. Liquid-infused surfaces (LISs) are an evolution of these surfaces, substituting air with a low-viscosity liquid. Doing so improves the durability of LISs against increasing shear stress and hydrodynamic pressure. While SHSs and LISs have been shown to work in turbulent hydrodynamic flows (Rosenberg et al., 2016; Park et al., 2021), neither would be feasible in aerodynamic applications due to the added roughness and the minuscule slip lengths created by the unfavourable viscosity ratio between the liquid and air. This thesis explores the novel idea of liquid-infused superhydrophobic surfaces (LISHySs), conceptualised for flows with air as the external medium. These surfaces use liquid droplets held in superhydrophobic features to induce slip at the air-liquid interface while reducing resistance to the motion of the liquid within the cavity.

Since no framework existed on the drag-reducing mechanism of such a surface, this was devised and the parameters of importance were identified. These were seen to be the area of the air-liquid interface, the exposed and submerged areas of the droplets in the cavities, and the degree of superhydrophobicity of the surface. Two types of liquid-infused superhydrophobic surfaces (LISHySs) were consequently designed - one with spherical droplets and the other with cylindrical droplets oriented in the spanwise direction. These were produced by 3D printing surfaces with cavities and applying an industrial superhydrophobic coating. Water was infused into the cavities using a sprayer.

Three tests were carried out to assess the performance of the surfaces. First, direct force measurements were used to calculate drag characteristics. Particle image velocimetry (PIV) was then used to quantify the flow over the LISHySs. In both tests, the results of the produced surfaces were compared against that of a smooth wall for reference. Finally, the behaviour of the air-liquid interface was closely observed. Drag measurements showed that the infused surface with spherical cavities had a higher drag coefficient (varying between 10% and 17%) with respect to the smooth surface. While PIV for the flow over this surface showed an increase in mean streamwise velocity and a decrease in Reynolds stress in the overlap layer, the high degree of reflection produced by the surface meant that meaningful near-wall data could not be obtained. Observations of the air-liquid interface demonstrated that the hypothesised steady rolling motion of liquid droplets occurred at low freestream velocities, indicating that the surface was capable of locally producing slip. However, higher velocities created chaotic motion at the interface with spanwise flow being observed. Pressure drag due to droplets acting as roughness elements, among other reasons, further contributes to the drag produced by the surface.

While the results showed that the current implementation of LISHySs was unsuccessful in the context of drag reduction, the lessons from this first attempt show the directions in which future studies could be made. Investigations using spherical droplets are unlikely to be successful due to the low area that is exposed to air and the microscopic size of the droplets needed, offering challenges in manufacturing the surfaces. The effect of evaporation is also more pronounced in this case due to smaller volumes. If a method for retention is devised, cylindrical droplets that are oriented in the streamwise direction offer higher potential than the tested surfaces due to the creation of streamwise slip. Advancements in the fields of material science and hydrophobicity would allow for the production of surfaces that exhibit higher superhydrophobicity with finer cavities. Measures such as these would pave the way for the passive reduction of turbulent drag through the novel concept of LISHySs.

Table of Contents

List of Figures

List of Tables

Nomenclature

Acronyms and Abbreviations

AE	Aerospace Engineering
AoA	Angle of attack
BL	Boundary layer
CC	Cross-correlation
CNC	Computer Numerical Control
DASML	Delft Aerospace Structures and Materials Laboratory
DFM	Direct force measurement
DNS	Direct numerical simulation
DR	Drag reduction
FOV	Field of view
HSL	High Speed Laboratory
IPA	Isopropyl alcohol
LCD	Liquid-crystal display
LE	Leading edge
LF	Liquid fraction
LSL	Low Speed Laboratory
MAT	Micro Alignment Telescope
MSLA	Masked Stereolithography Apparatus
PIV	Particle image velocimetry
PTU	Programmable timing unit
px	Pixels
rms	Root mean square
RMSE	Root-mean-square error
RPM	Rotations per minute
SLA	Stereolithography
STL	Standard Tessellation Language
TBL	Turbulent boundary layer
TE	Trailing edge
TPM	Tripropylene glycol monomethyl ether
TU Delft	Delft University of Technology
UV	Ultraviolet
WT	Wind tunnel
ZPG	Zero pressure gradient

Dimensionless Groups

C_D	Drag coefficient
C_f	Skin friction coefficient
Re	Reynolds number
Re_δ	Reynolds number based on boundary layer thickness
Re_τ	Friction Reynolds number based on wall shear stress
Re_θ	Reynolds number based on momentum thickness
Re_x	Reynolds number based on streamwise distance from boundary layer starting point

Greek Symbols

Δ	Difference
δ	Boundary layer thickness
δ^*	Displacement thickness
δ_v	Viscous length scale
ϵ	Standard error
κ	von Kármán constant
λ	Slip length
μ	Dynamic viscosity, mean
ν	Kinematic viscosity
Π	Wake strength
ρ	Density
τ	Shear stress
τ_w	Wall shear stress
θ	Momentum thickness

Latin Symbols

A	Area
a	Opening radius
B	Turbulent boundary layer wall law intercept constant
d	Cavity depth
F	Force
f	Frequency
F_p	Pressure force
F_{null}	Null force
GF	Gas fraction
H	Shape factor
h	Protrusion height
L	Characteristic length scale, length
$O()$	In the order of
OR	Opening ratio
p	Pressure
p_a	Absolute pressure
q	Dynamic pressure
r	Cavity radius
R_{xy}	Reynolds stress
S	Surface area
t	Thickness, time
u	Velocity (vector)
u, v, w	Velocity in streamwise, wall-normal and spanwise directions
u', v', w'	Velocity fluctuation in streamwise, wall-normal and spanwise directions
U_∞	Freestream velocity
x, y, z	Coordinates in streamwise, wall-normal and spanwise directions
x_{TP}	Streamwise distance w.r.t. test plate leading edge

Superscripts

$+$	Expressed in viscous units

Subscripts

ext	External/bulk medium
int	Internal/lubricating medium

1

Introduction

Nature has always been one of the greatest sources of inspiration for human innovation. From the bullet train with its nose shaped like a kingfisher's beak to wind turbine blades resembling whale fins, biomimetics has been used to solve modern problems. With the ongoing climate crisis, efforts need to be taken immediately to make human activities more sustainable. In the context of aviation, passive flow control techniques offer a contribution to this objective. This thesis aims to experimentally explore the potential of using slip-inducing surfaces, a category of passive flow control techniques, to reduce the turbulent viscous drag of objects in air.

1.1. Relevance of drag reduction

One of the greatest challenges that exists today is the climate crisis, with a rise in temperatures being reported across the world caused by human activities. According to IEA (2022b), the transport industry alone, due to its heavy reliance on fossil fuels, accounted for 37% of CO_2 emissions in 2021. While road transport accounts for the bulk of this, aviation has played a significant role, producing over 1 billion tonnes of CO_2 annually as shown in Figure 1.1. This makes it responsible for 3.5% of global warming effects when non-CO_2 effects are also taken into account (Ritchie, 2020). This means that the aviation industry is currently not on track to meet its sustainability target of Net Zero Emissions by 2050 (IEA, 2022a).

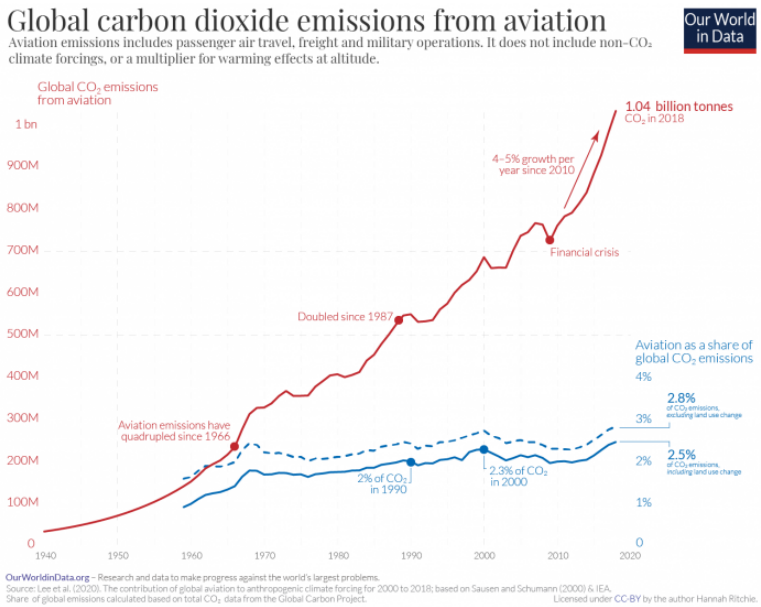

Figure 1.1: Global CO_2 emissions from aviation (Ritchie, 2020)

While governmental and non-governmental agencies have been pushing for electrification and sustainable aviation fuels to reduce aircraft emissions, another solution is to reduce the drag of aircraft as they fly through the air. Schrauf et al. (2006) determined that viscous drag alone accounted for around 55% of the total drag of a commercial transport aircraft in cruise. Thus, targeting this component of drag alone would result in notable fuel savings. An analysis by Grau (2022) estimated that the implementation of a technique that reduced viscous drag by 10% in laboratory conditions would result in fuel burn savings of approximately 2.5%. This is due to the following factors:

1. The surface area of the aircraft over which a technique could be implemented, which would reduce its effectiveness by 30%
2. The higher frictional Reynolds numbers of the flow over an aircraft, which would further decrease its performance by 40%
3. The contribution of skin friction to the total drag of an aircraft, which is around 55%
4. The change to flight altitude to balance viscous and pressure drag due to reduced skin friction, which increases drag reduction by 3.33%
5. The reduced weight of the aircraft due to the need for lesser fuel, which improves drag reduction by 16.67%

Even a drag reduction of merely 1% on a commercial aircraft such as the A340-300 would result in preventing 400,000 litres of fuel burn annually (Kornilov, 2015). While research on drag reduction techniques that can be retrofitted on existing aircraft will have significant impacts in the short term by reducing emissions, they will also affect the design of the next generation of aerial vehicles, allowing for greater passenger loads while reducing the amount of space required to store fuel on board, possibly in the form of battery units or hydrogen tanks.

1.2. Significance of flow control

Flow control is the artificial modification of the flow over a surface in order to improve its performance in terms of lift production, drag reduction or both. One of the first demonstrations of this concept was made by Prandtl (1904) through the use of wall suction to delay transition. Once the concept of the boundary layer was understood, and connections were made between Prandtl's theoretical and experimental work, German scientists were fairly active in this field in the 1930s. Following the Second World War, research in flow control was not a priority due to the low price of petroleum and low reliability of experimental equipment. The Arab oil embargo in the 1970s and the resulting skyrocketing fuel prices restarted efforts in this field. Currently, research is driven by the need to make aviation sustainable.

Flow control techniques can be broadly classified as passive or active (Gad-el-Hak, 2000). Passive flow control techniques are those that do not need an input of energy to alter the flow. They are commonly in the form of geometric modifications to a surface and are always operational. A simple example is a vortex generator, which enhances mixing of the flow by shedding longitudinal vortices. This keeps the flow attached at higher adverse pressure gradients due to the greater energy content, improving stall characteristics. On the other hand, active flow control techniques require auxiliary power and can be used when needed, providing greater flexibility. An example is the introduction of a substance, such as a long-chain molecule, into the flow. By suppressing the production of Reynolds stress in the buffer layer between the viscous sublayer and the logarithmic layer of the boundary layer, turbulent mixing is reduced, leading to drops in wall shear stress and the drag produced. Reactive flow control techniques, a category within active flow control, make use of a feedback or feedforward control system. By monitoring the state of the flow through sensors, an actuator can alter it to achieve optimum conditions over the surface.

Comparing these methods, it can be seen that passive flow control techniques offer a relatively simple solution without the necessity for the installation or operation of a more complex system. While they are less flexible than active systems in adapting to variable operating conditions, there are no weight or energy penalties for additional systems that are necessary in the case of the latter. Also, maintenance is simplified due to the lack of moving components. Thus, there is value in investigating known passive flow control techniques further to identify knowledge gaps and derive new ideas from these to meet climate targets.

1.3. Introduction to slip-inducing surfaces

In a wall-bounded flow, the no-slip condition at the wall causes a velocity gradient at the interface between the fluid and the solid wall. This velocity gradient results in shear stress at the wall, which is responsible for skin friction drag. Slip-inducing surfaces reduce this drag by allowing for a non-zero velocity of the fluid at the interface.

Inspired by the manner in which water beads up and rolls smoothly on the surface of lotus leaves (shown in Figure 1.2), superhydrophobic surfaces (SHSs) use micro- or nano-pores that trap pockets of air in them. This results in slip of the external fluid, typically water, close to the surface at the macro-scale level. At the micro-scale level, the no-slip condition is present at the interface between the trapped air and the wall. SHSs have been studied extensively in the last few decades and observed to produce drag reduction of up to 75% (Park et al., 2014). Lafuma and Quéré (2003) theorised that superhydrophobicity was based on the models developed by Wenzel (1936) and Cassie and Baxter (1944), which explained the wetting of a surface by a liquid droplet. They stated that the smooth-surface contact angle of the material would have to be greater than the contact angle at which the Wenzel and Cassie models intersect, known as the critical angle. Hydrophobic surfaces with microscopic roughness could trap air in pores, giving rise to a surface with air-water and solid-water interfaces. This drastically reduces the skin-friction drag on a submerged surface in laminar and turbulent flows. A key measure of the longevity of the surfaces is their capability to retain air in their pores due to mass diffusion (Ling et al., 2017) and instability of the gas pockets (Fairhall et al., 2019).

Figure 1.2: A droplet on a lotus leaf (Bhushan and Jung, 2011)

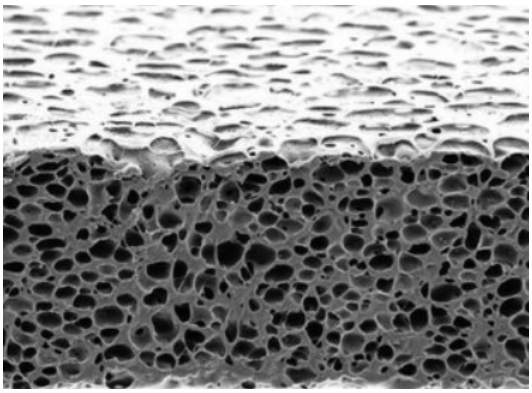

Figure 1.3: An isotropic porous surface (Gloukhovski et al., 2018)

Liquid-infused surfaces (LISs) substitute the air in the pores of SHSs with a liquid that is immiscible with the external medium. This liquid, typically an oil, creates a slip effect and reduces drag in laminar and turbulent flows (Fu et al., 2017). While LISs typically do not produce as high drag reduction as SHSs, they offer better working under hydrodynamic pressure and lower diffusion of the lubricant into the external flow, meaning that they remain operable in conditions where SHSs would fail. However, the retention of the lubricant is still a concern, with studies being carried out to examine the effects of parameters including viscosity ratio, cavity geometry, Reynolds number and Weber number (Rosenberg et al., 2016; van Buren and Smits, 2017).

Porous surfaces are yet another type of slip-inducing surface. Due to the open pores, a slip boundary condition can be applied at the surface. These surfaces are characterised on the basis of their porosity and permeability, and can be isotropic (as shown in Figure 1.3) or anisotropic (Suga et al., 2010). The flow within a porous surface can described by an empirical relation derived by Darcy (1856), with flow at the interface being accounted for by a modification proposed by Brinkman (1949). Gómez-de-Segura et al. (2018) numerically showed that anisotropic porous surfaces with a preferred permeability in the streamwise direction were optimal for turbulent skin friction reduction. This was validated by Rosti and Brandt (2017), who simulated a turbulent channel flow with varying streamwise to surface-normal permeability ratios. A net drag reduction was observed when the ratio was larger than 1, with a maximum skin friction reduction of 20%. However, a recent study by Hartog (2021) found an increase in drag between 0 and 8% for a permeable 3D-printed surface with no mesaured slip velocity at the substrate-flow interface. Additionally, the physical realisation of the theoretical framework was deemed questionable, due to the mismatch between the pore size and permeability necessary for drag reduction.

While these surfaces are not the only examples of slip-inducing surfaces, the limited research carried out

on LISs presents high promise for further development. The current work explores the potential of a newly conceptualised idea derived from LISs, in the form of liquid-infused superhydrophobic surfaces (LISHySs). These utilise liquid volumes held in superhydrophobic cavities, which reduce the friction of the fluid as they flow within the cavities. Thus, it may be possible to further enhance the drag-reducing capability of LISs, especially in aerodynamic applications.

1.4. Research goals

This section establishes the scope for the work to be carried out in the current research endeavour. This is done by determining the objectives of the study, followed by listing the questions that need to be answered to provide comprehensive insight into LISHySs.

Research objectives

The main research objective for the thesis has been determined as:

> *To explore the potential of **liquid volumes trapped in superhydrophobic features** for **turbulent viscous drag reduction** in external flows in **air** and **identify the parameters** that govern drag reduction by performing **direct force measurements** and **quantifying the flow field** through particle image velocimetry.*

This objective has been decomposed into the following sub-objectives to clearly identify the tasks at hand. These have been stated as goals, followed by the means needed to accomplish them.

1. To **develop a theoretical framework** for the drag reduction mechanism.
   Through the principles that create drag reduction in SHSs and LISs, a theoretical description of the drag reduction mechanism needs to be presented.

2. To **design and produce** LISHySs.
   Specimens with varying cavity geometries need to be designed and an appropriate manufacturing process will have to be chosen to create them. These specimens will need to be made superhydrophobic, either through the manufacturing process or a separate treatment process. Finally, a method to trap liquid droplets in the surface must be identified.

3. To **measure the drag** produced by the surfaces.
   The specimens need to be placed in a purpose-built force balance in a wind tunnel and subject to a determined velocity sweep. The drag readings will have to be compared against those of a smooth flat plate in order to establish the change in drag due to the presence of the liquid-filled cavities.

4. To **observe the changes** to the **turbulent boundary layer** formed over the surface.
   Boundary layer data of the flow close to the surface needs to be captured. Particle image velocimetry (PIV) is an effective way to do this. This will be used to infer the presence of slip at the surface and the alteration of turbulent structures.

5. To **verify the behaviour of droplets** inside the cavities.
   A microscopic study of the motion of the liquid inside the cavities needs to be carried out. This will provide further clarity into the results of the drag measurement and flow visualisation campaigns.

Research questions

The research questions have been conceived in order to address all aspects of the research objective. For each research question, sub-questions have been defined to provide well-rounded answers. They are as follows:

1. What factors must be addressed in order to develop the theoretical framework?
   (a) What are the key parameters responsible for drag reduction?
   (b) How do the identified parameters relate to one another?

2. How can LISHySs be manufactured?
   (a) What are the most promising cavity designs?
   (b) What are the possible base materials and the appropriate manufacturing processes that could be used?
   (c) Which combination of readily available coatings and liquids produces highly spherical droplets that easily roll off a flat surface?
   (d) Which liquid has the least rate of evaporation in order to increase retention inside the cavities?
   (e) How can the geometry of the finished product be verified against the planned model?
3. How can LISHySs be effectively tested, and what do the results indicate?
   (a) Which velocity range would be the most appropriate for this study? Do the results show drag reduction within this range?
   (b) How close to the wall can boundary layer data be gathered from? How much of an inhibiting factor will reflections from the liquid and surface cavities be?
   (c) To what extent can slip at the air-liquid interface be inferred from the acquired data?
   (d) What is the variation in the results observed due to different cavity designs?
   (e) What is the extent of liquid retention inside the cavities after the tests?
4. Can the hypothesised working principle be verified from observations of the flow over them?
   (a) What is the experimental setup necessary to observe the motion of the liquid inside a cavity?
   (b) Can the existing LISHyS samples be used or will new ones need to be made? If the latter option is chosen, what part of the design needs to be changed?
   (c) Do the observations justify the results of the drag measurement and PIV campaigns?

1.5. Report overview

The report is divided into six chapters to methodically study the performance of liquid-infused superhydrophobic surfaces in an aerodynamic setting. The first two chapters introduce the topics of interest and the fundamental principles involved in order to understand them. Following Chapter 1, an overview of the concepts relevant to turbulent flows over slip-inducing surfaces, with particular attention to SHSs and LISs, is provided in Chapter 2. The concept of liquid-infused superhydrophobic surfaces (LISHySs) is also introduced in this chapter. Chapter 3 discusses the considerations and calculations made while creating the surfaces. This chapter also describes the procedure by which the superhydrophobic surfaces were created and infused with liquid droplets. The following two chapters go over the experiments carried out on LISHySs to assess their performance. Chapter 4 elaborates on the experimental setup facilitating the wind tunnel tests. Chapter 5 reports the results of these tests and discusses the reasons behind the observations. Finally, Chapter 6 closes the report, answering the research questions and suggesting means by which future studies on LISHySs can be made more effective as a means of achieving drag reduction.

2

Turbulent boundary layers over slip-inducing surfaces

Turbulent boundary layers

Since the proposed application of the flow control technique of interest is in the turbulent regime, this chapter begins by looking into turbulent boundary layers in greater detail. Section 2.1 goes over the fundamental concepts related to the development and characterisation of turbulent boundary layers. Coherent structures, which are turbulent flow structures that are spatially and temporally repeated, are briefly discussed in Section 2.2. This is followed by a discussion of the analysis techniques suited to characterising turbulent boundary layers in Section 2.3.

2.1. Boundary layer fundamentals

For a fluid flowing past a wall, the no-slip condition imposes a zero velocity condition on the fluid at the wall due to viscous effects. Moving away from the wall, the local velocity increases and eventually approaches the freestream velocity at a certain distance from the wall. This region of fluid having a velocity between zero and the freestream value is called the boundary layer (BL), and the resulting streamwise velocity profile in this region is referred to as the boundary layer profile.

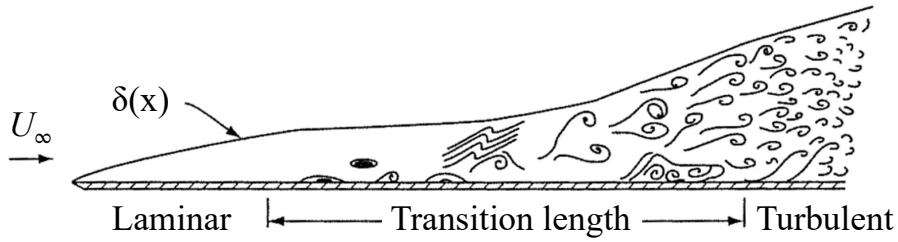

Figure 2.1: Boundary layer development over a flat plate, adapted from White (2006)

Boundary layers can be classified as laminar or turbulent. In a laminar BL, distinct layers of fluid do not penetrate each other. A turbulent BL sees the mixing of fluid layers, resulting in greater mass and momentum transfer. This also means that it has higher energy content since it brings energy from the freestream close to the wall where there is low energy flow. The process by which a laminar BL evolves into a turbulent BL is known as transition. This begins with the development of unstable 2D Tollmien-Schlichting (TS) waves, which distort and grow into 3D spanwise variations and hairpin eddies. In regions of high shear, vortex breakdown occurs, creating strong 3D fluctuations. This leads to the formation of turbulent spots, which are pockets of strong turbulent activity. The coalescence of these spots results in fully turbulent flow.

2.1.1. Boundary layer properties

In order to characterise it, the boundary layer is described through a number of mean properties. The equations that have been listed are based on White (2006) unless stated otherwise.

Boundary layer thickness

The boundary layer thickness δ is defined as the distance y from the wall where the streamwise flow velocity u is 99% of the freestream velocity U_∞. It is expressed as:

$$\delta = y\big|_{u/U_\infty=0.99} \tag{2.1}$$

For turbulent flow over a flat plate, the boundary layer thickness is estimated from Prandtl's power law approximation as:

$$\frac{\delta}{x} \approx \frac{0.16}{Re_x^{1/7}} \tag{2.2}$$

with the Reynolds number Re_x defined as

$$Re_x = \frac{\rho U_\infty x}{\mu} = \frac{U_\infty x}{\nu} \tag{2.3}$$

where ρ is the density, μ is the dynamic viscosity, ν is the kinematic viscosity, and x is the streamwise distance from the start of the boundary layer ($\delta = 0$ at $x = 0$). Note that Equation (2.2) is valid for a zero pressure gradient flow.

Displacement thickness

The displacement thickness δ^* is thickness of flow moving at freestream velocity that has a flow rate equal to the loss in flow rate due to boundary layer formation. In other words, it is the distance by which the wall should be displaced to compensate for the reduction in flow rate. It is calculated as the integrated velocity deficit of the boundary layer, expressed as:

$$\delta^* = \int_0^{y\to\infty} \left(1 - \frac{u}{U_\infty}\right) dy \tag{2.4}$$

Momentum thickness

The momentum thickness θ is an indication of the momentum loss due to friction forces within the boundary layer. It can be interpreted as the theoretical thickness of a fluid layer in the freestream carrying the amount of momentum equal to that lost in the boundary layer, and is calculated as:

$$\theta = \int_0^{y\to\infty} \frac{u}{U_\infty}\left(1 - \frac{u}{U_\infty}\right) dy \tag{2.5}$$

For flow over a flat plate, the momentum thickness directly relates to the friction drag via:

$$C_f = 2\frac{d\theta}{dx} \tag{2.6}$$

Scaled variables

In order to compare BL profiles for varying flows, it is useful to non-dimensionalise terms such as the flow velocity and wall distance. This is done using the friction velocity u_τ, expressed as:

$$u_\tau = \sqrt{\frac{\tau_w}{\rho}} \tag{2.7}$$

where τ_w is the wall shear stress. Using this, the non-dimensionalised flow velocity u^+ and wall distance y^+ are calculated as:

$$u^+ = \frac{u}{u_\tau} \qquad y^+ = \frac{y u_\tau}{\nu} \tag{2.8a, 2.8b}$$

A variable with the superscript '+' is represented in viscous units (also called wall units). The length of a viscous unit length is determined as:

$$\delta_\nu = \frac{\nu}{u_\tau} \tag{2.9}$$

The friction Reynolds number Re_τ associated with the friction velocity is given by:

$$Re_\tau = \frac{u_\tau \delta}{\nu} \tag{2.10}$$

Skin friction drag

In a turbulent flow, the total shear stress τ is the sum of the contribution of the viscous stress and the Reynolds shear stress and is given by:

$$\tau = -\rho \overline{u'v'} + \mu \frac{\partial u}{\partial y} \tag{2.11}$$

where the first term represents the Reynolds shear stress and the second term represents the viscous stress. At the wall, the first term is zero since there are no fluctuations in the velocity components. Thus, the shear stress at the wall τ_w, also known as the skin friction, is given by:

$$\tau_w = \mu \left. \frac{\partial u}{\partial y} \right|_{y=0} \tag{2.12}$$

In order to compare the friction experienced by different surfaces under varying flow conditions, the skin friction coefficient is computed as:

$$C_f = \frac{\tau_w}{\frac{1}{2}\rho U_\infty^2} = 2\left(\frac{u_\tau}{U_\infty}\right)^2 \tag{2.13}$$

The skin friction coefficient for turbulent flow over a flat plate can be estimated from a power law approximation as:

$$C_f \approx \frac{0.027}{Re_x^{1/7}} \tag{2.14}$$

2.1.2. Regions in a turbulent boundary layer

The boundary layer in turbulent flow can be divided into two main regions: the inner layer and the outer layer. While the flow in the inner layer is dependent on conditions near the wall, the outer layer is more dependent on freestream conditions. The streamwise velocity profiles for these regions have differing mathematical descriptions so a third region that partially overlaps the two, as shown in Figure 2.2, is introduced.

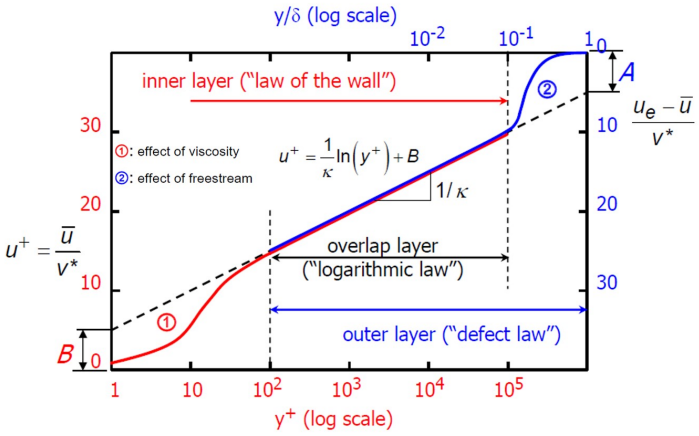

Figure 2.2: A schematic of the boundary layer (van Oudheusden, 2020)

The inner layer can be further divided into three sublayers as:

1. Viscous sublayer: $y^+ \leq 5$
   Viscous forces are dominant, causing the velocity profile to be linear ($u^+ = y^+$).

2. Buffer layer: $5 \leq y^+ \leq 30$
   Viscous and Reynolds shear stresses are of the same order. The velocity profile here smoothly transitions from linear to logarithmic.

3. Overlap layer: $30 \leq y^+ \leq 0.1\delta^+$
   This velocity here is dependent on flow conditions both near the wall and in the freestream, and is given as:
   $$u^+ = \frac{1}{\kappa}\ln y^+ + B$$
   where κ is the von Kármán constant (typically 0.41) and B is a constant (typically 5.0) for a zero pressure gradient TBL. δ^+ is the BL thickness calculated in wall units.

2.2. Coherent structures

Among the chaos inherent in turbulent flows, there exist organized structures or regions in the flow that persist for a relatively long period of time. These are known as coherent structures, and can be defined as "a connected turbulent fluid mass with instantaneously phase-correlated vorticity over its spatial extent" (Hussain, 1983). They are characterized by high vorticity and kinetic energy, and play a significant role in the transport of quantities such as heat, mass and momentum within the boundary layer. Examples of coherent structures include vortices, jets and shear layers.

Coherent structures originate from the growth and interactions of small perturbations in the flow field. Vortical structures are characterized by high vorticity and are typically associated with large-scale eddies. Streamwise structures have high velocity gradients, as in the case of streaks or large-scale rollers. Streaky structures, such as hairpin vortices, are indicated through high Reynolds stresses.

One of the mechanisms that drive the formation of coherent structures is the instability of shear layers, which are regions with abrupt velocity changes. The instability of these layers leads to the formation of structures such as vortices. The von Kármán vortex street (von Kármán and Rubach, 1912) is a well-known example of this. Formed in the wake of a circular cylinder, A series of vortices is observed as being shed alternately from diametrically opposite sides.

Another mechanism that creates coherent structures is the nonlinear interaction of vortices. This is known as vortex pairing, and results in the creation of large-scale vortices. These vortices can have a significant impact on the transport of properties within the flow such as transporting momentum from the near-wall region to the outer region.

2.3. Boundary layer analysis

In the analysis of turbulent boundary layers, the most important parameters that need to be assessed are the profiles of the mean streamwise velocity (u), the root mean square of the streamwise and spanwise velocity fluctuations (u_{rms} & v_{rms}) and Reynolds stress ($-\overline{u'v'}$). u indicates the mean state of the BL while the other terms point to the degree of turbulence in it.

In order to plot BL profiles in terms of the scaled variables, an approximation of the friction velocity u_τ is required. The methods to perform this vary from direct linear interpolation in the viscous sublayer and the indirect method via the log-layer (Clauser's method) to Spalding's law of the wall. The method of Rodríguez-López et al. (2015) fits the entire BL profile based on all the parameters of interest: δ, u_τ, κ, Π and Δy, where Π is wake strength and Δy allows for a wall-normal shift of the entire profile in case of uncertainty in the estimated wall location. The canonical description of the boundary layer is given by:

$$u^+ = \begin{cases} u^+_{\text{musker}} + u^+_{\text{bump}} + \frac{2\Pi}{\kappa}\mathcal{W}(y/\delta) & 0 \leq y \leq \delta \\ U^+_\infty & \delta \leq y \leq \infty \end{cases}$$

u^+_{musker} is the profile in the buffer layer that adapts the inner and logarithmic layers as defined by Musker (1979). It is obtained by integrating:

$$\frac{du^+}{dy^+} = \frac{\frac{(y^+)^2}{K} + \frac{1}{s}}{(y^+)^3 + \frac{(y^+)^2}{\kappa} + \frac{1}{s}}$$

where s is a constant relating the eddy viscosities in the inner and overlap regions.

u^+_{bump} was first described by Monkewitz et al. (2007) and accounts for an overshoot over the logarithmic law on the buffer layer. It is expressed as

$$u^+_{\text{bump}} = \frac{\exp\left[-\log^2\left(y^+/M_1\right)\right]}{M_2}$$

where $M_1 = 30$ and $M_2 = 2.85$.

$\mathscr{W}(y/\delta)$ is the exponential wake function as described by Chauhan et al. (2009), written as:

$$\mathscr{W}(y/\delta) = \frac{1-\exp\left[-(1/4)\left(5a_2+6a_3+7a_4\right)(y/\delta)^4 + a_2(y/\delta)^5 + a_3(y/\delta)^6 + a_4(y/\delta)^7\right]}{1-\exp\left[-(1/4)\left(a_2+2a_3+3a_4\right)\right]} \times \left(1 - \frac{1}{2\Pi}\ln(y/\delta)\right)$$

where $a_2 = 132.8410$, $a_3 = -166.2041$ and $a_4 = 71.9114$.

The canonical velocity profile is defined only as a function of κ, s, Π, δ and y. Defining the velocity at specific points, which is done through experimental measurements, allows for this to be related to u_τ and Δy.

Slip-inducing surfaces

Section 1.3 briefly discussed the concept of slip-inducing surfaces. The following sections look into these surfaces in greater detail. First, superhydrophobic surfaces, which have seen an extensive amount of research being carried out on them, are discussed in Section 2.4. Liquid-infused surfaces, which have been derived from these in order to improve their resilience to flow conditions, are covered in Section 2.5. Due to the incapability of LISs to reduce drag in air, a novel concept that integrates learnings from SHSs and LISs, namely liquid-infused superhydrophobic surfaces, is presented in Section 2.6.

2.4. Superhydrophobic surfaces

Superhydrophobic surfaces contain roughness elements that trap pockets of air or a layer of it, known as plastron (Brocher, 1913), when submerged in water. This creates fluid-fluid interfaces that cause an effective slip of the external fluid over the surface, instead of the no-slip boundary condition that is traditionally present in viscous flows over fluid-solid interfaces. The no-slip condition still exists inside the cavity, between the solid surface and the trapped air, but due to the lower velocity of air circulating in the cavity and the directions in which the stresses act, there is a net drag reduction.

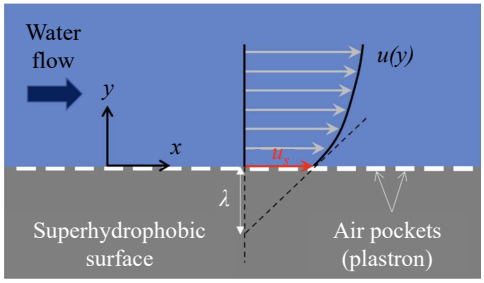

Figure 2.3: Velocity distribution over an SHS (Park et al., 2021)

Figure 2.3 shows the parameters that are useful in defining flows over SHSs. The slip velocity, u_s, is the non-zero velocity of the liquid-air interface. The slip length, λ, (from the Navier slip model) is used to quantify

the measure of slip. To visualise this parameter, consider the linear extrapolation of the velocity gradient at the interface into the surface. At some point, this will result in the slip velocity u_s being equal to zero. The slip length is calculated as the distance between the interface and this point. The slip length and slip velocity are related as:

$$u_s = \lambda \frac{\partial u}{\partial y}\bigg|_{y=0}$$

Common water flows have viscous sublayer thicknesses of O(10-100) μm (Yeginbayeva and Atlar, 2018). SHSs have been shown to provide λ of O(10) μm (Ou et al., 2004; Choi and Kim, 2006; Truesdell et al., 2006; Lee et al., 2008), which is able to alter the dynamics of such flows. Thus, there is notable interest in their potential for hydrodynamic drag reduction.

Numerical investigations, such as those by Busse and Sandham (2012), Park et al. (2013), and Liu et al. (2016) showed that the effective slip alone could not answer why turbulent flows experienced more skin friction reduction than laminar flows over the same surfaces. It was seen that the streamwise slip would suppress the formation of near-wall turbulence structures (streaky structures with higher streamwise vorticity), resulting in decreased turbulence intensity and Reynolds stress near the SHS (Jelly et al., 2014; Im and Lee, 2017). This is demonstrated in Figure 2.4. Martell et al. (2010) proposed a different mechanism, claiming that the SHS would shift near-wall structures away from the wall, which could also reduce drag. Spanwise slip had a countering effect to drag reduction because of the strengthening of the dynamics of streamwise streaky structures, mitigating the slip effect (Min and Kim, 2004; Fukagata et al., 2006).

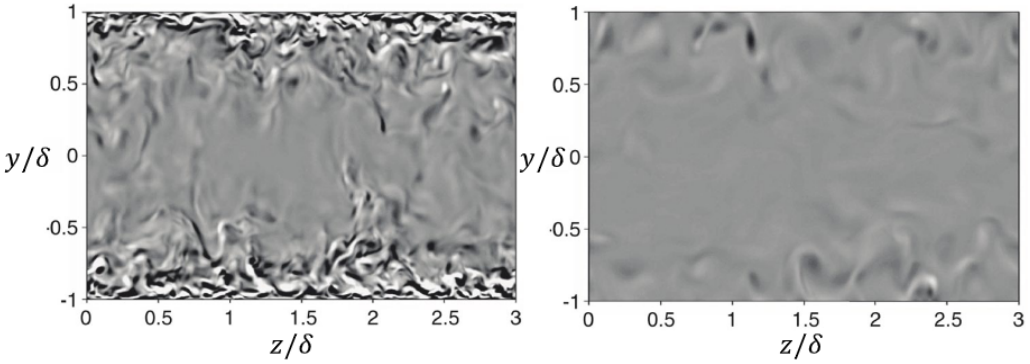

Figure 2.4: Streamwise vorticity contours in y–z plane for turbulent channel flow in x (i.e., flowing into the page) at Re_τ = 590: smooth walls (left) and SHS walls of longitudinal grooves with 93.75% GF and pitch P^+ = 220 wall units (right) (Park et al., 2013)

Rastegari and Akhavan (2015) proposed modelling the drag reduction ratio as $u_s/u_{bulk} + \Delta\varepsilon$, where u_s and u_{bulk} represent the slip velocity and bulk velocity in an uncontrolled channel flow, respectively. (u_s/u_{bulk}) is the contribution from the direct slip effect while $\Delta\varepsilon$ corresponds to that of turbulence modification. They found that the latter is positive (but not more than 20% of the total drag reduction) in the case of longitudinal grooves but negative in the cases of transverse grooves and posts, even resulting in an overall drag increase.

Experimental studies have brought forth evidence of turbulence suppression on SHSs. Haibao et al. (2015) and Tian et al. (2015) measured the the decomposition of time-resolved velocity and found reduced occurrences of vortex bursting in the near-wall region. Vajdi Hokmabad and Ghaemi (2016) saw that due to the plastron, the vortex dynamics of sweep and ejection were suppressed, and the spanwise distance between low and high speed streaks were increased. They also confirmed that spanwise slip acted against the the drag reduction caused by streamwise slip due to the enhancement of spanwise turbulence intensities.

2.4.1. Drag reduction observed in experiments

Park et al. (2021) gathered an extensive collection of experimental research carried out on SHSs. They found that most studies used randomly distributed roughness morphology, done through either spray coating or chemical etching due to convenience and scalability. Fewer studies made use of well-defined and ordered morphology like grooves and posts that required precision machining. To compare experiments that had differing characteristic length scales, the frictional Reynolds number (Re_τ) was used instead of (Re_L).

The advantage of using organised roughness is that the influence of the geometrical parameters of the roughness structures, such as their width and depth, could be studied more accurately, as opposed the averaging of properties that is assumed on a surface with random roughness.

Henoch et al. (2006) conducted measurements on an SHS with an array of tall posts spaced in nanoscale (diameter: 400 nm, periodicity: 1.25 μm , $w^+ \approx 0.03$, $Re_\tau = 150$), as seen in Figure 2.5a, in boundary-layer flows inside a water tunnel. Drag reduction was seen to be much higher in laminar flows (as much as 50%) than in turbulent flows (10%).

Most of the studies that followed used SHSs with grooves, since these provide the highest values of streamwise slip lengths. Woolford et al. (2009) used PIV measurements over grooved SHSs, shown in Figure 2.5b, in turbulent channel flows for $Re_H = 4800$–48000 ($Re_\tau = 100$) to study the importance of slip direction. Here, H is the channel height. An SHS with streamwise grooves and $GF = 0.8$ produced less turbulence ($\approx 11\%$) than the smooth surface, but spanwise grooves were seen to increase turbulence by 6.5%.

In the same year, Daniello et al. (2009) measured the pressure drop in turbulent channel flows with an SHS having longitudinal grooves to obtain $Re_H = 2000$–9500 ($Re_\tau = 180$). While GF was fixed at 0.5, Re_H was varied by changing the space width (w) of the groove. No discernible drag reduction was noticed in the laminar regime but for $Re_H > 3000$ (turbulent), the rate of drag reduction increased as Re_H increased. This led them to conclude that effective drag reduction in turbulent flows can occur when the space width of the groove is comparable to the thickness of a typical viscous sublayer in turbulent boundary layer flows. Thus, $w^+ = w/l_v \approx 5$ wall units. The viscous length scale ($l_v = \nu/u_\tau$), measured in wall units, generally decreases as the Reynolds number increases, so higher Re allows a given groove width to reduce drag better. This is under the constraint that the plastron should be retained despite the increased shear and turbulence.

Park et al. (2014) achieved a drag reduction of 75% on longitudinally grooved SHSs, seen in Figure 2.5c, while directly measuring skin-friction drag in a water tunnel with GF = 0.97 at $Re_\tau = 250$. They also found that drag reduction would increase exponentially when $GF > 0.9$.

One of the latest experiments on SHS was carried out by Xu et al. (2021), who achieved up to 30% reduction in drag in a high speed towing tank experiment. Longitudinally grooved SHSs with $GF = 0.9$, as seen in Figure 2.5d, were tested for $Re_\tau = 2000$ - 5800, corresponding to $w^+ = 4$ - 16 wall units. However, they also observed plastron depletion for $Re_\tau > 4000$, which resulted in shear-driven wetting of the surface and caused a decrease in drag reduction.

In general, tests with longitudinal grooves were seen to produce consistent drag reduction, which increased with increasing Re. However, beyond a certain Re, plastron depletion caused this to decrease.

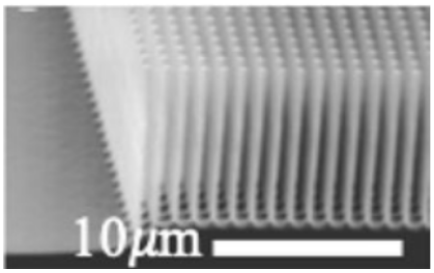

(a) Roughness used by Henoch et al. (2006)

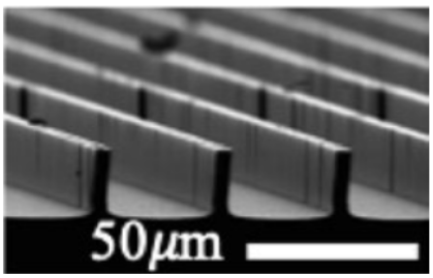

(b) Roughness used by Woolford et al. (2009)

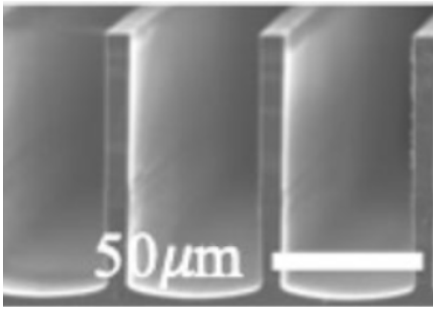

(c) Roughness used by Park et al. (2014)

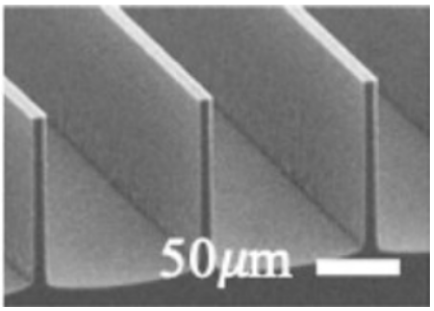

(d) Roughness used by Xu et al. (2021)

Figure 2.5: Images of surfaces with organised roughness (Park et al., 2021)

Since large surfaces can be made more easily with random roughness than with ordered roughness, many studies opted to use SHSs with random roughness.

Zhao et al. (2007) measured turbulent friction on an anodised aluminium oxide plate in a water tunnel but found no change in drag. Aljallis et al. (2013) used a plate of the same base material (aluminium) but coated it in silica nanoparticles and placed it in a high-speed towing tank with Re_τ varying from 1000 and 7000. While a maximum drag reduction of 30% was found, higher values of Re_τ saw an increase in drag due to surface wetting. The same surface was used by Zhang et al. (2015) in a turbulent boundary layer flow at Re_τ between 300 and 500. A drag reduction of 10 to 24% was observed. To understand the contribution of slip, Vajdi Hokmabad and Ghaemi (2016) measured the near-wall mean velocity profile on this surface compared to a smooth surface in a channel flow and noted a 3-5% increase.

Another type of coating that was used was fluorosilane. Bidkar et al. (2014) carried out turbulent boundary layer flow experiments at high Re_τ (2000 - 4000), noticing a 20-30% decrease in drag. They claimed that drag reduction was possible when the non-dimensional surface roughness (the ratio of the average roughness height to the viscous length scale) was at least an order of magnitude less than the viscous sublayer thickness. Srinivasan et al. (2015) tested this surface in a Taylor-Couette flow with Re_τ varying from 480 to 1310. They noticed higher drag reduction with increasing Re_τ and observed that by keeping the surface partially exposed to air, the plastron was kept intact for longer.

The widest variation in the drag reduction potential of SHSs was found by Gose et al. (2018). By placing SHSs with different random textures in a turbulent channel flow, drag reduction was seen to be as large as 90% and as low as -90%. A scaling relation was proposed between drag reduction and the product of roughness height (k^+) and contact-angle hysteresis (discussed further in Section 2.5.3), and it was concluded that both of these terms would need to be minimised in order to obtain noteworthy turbulent drag reduction.

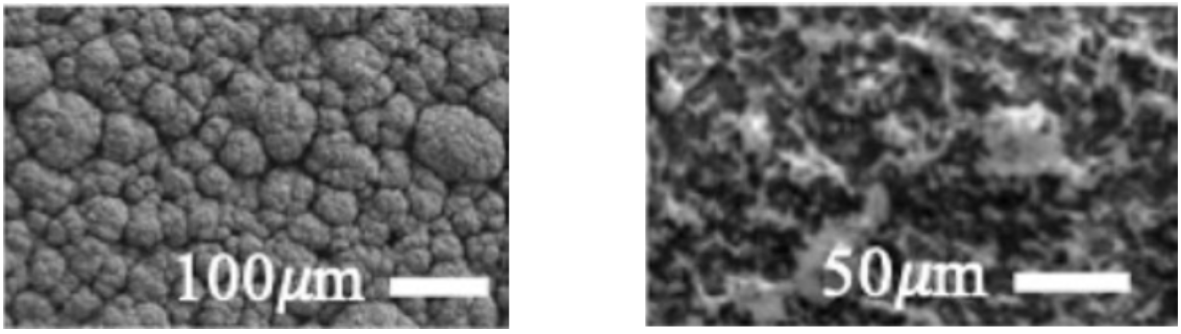

(a) Roughness used by Bidkar et al. (2014)

(b) Roughness used by Gose et al. (2018)

Figure 2.6: Images of surfaces with random roughness (Park et al., 2021)

2.4.2. Disadvantages of Superhydophobic Surfaces

Superhydrophobic surfaces can be manufactured relatively easily as compared to other passive flow control techniques and can offer a high degree of drag reduction. For this reason, SHSs could be used to reduce the energy consumption, and thus emissions of oceanic transportation and long-range liquid tansport pipe systems, among others (Ceccio, 2010; Murai, 2014; Berghout et al., 2021). Tests by Xu et al. (2020) using an SHS on a passenger motorboat cruising in sea water showed a drag reduction of nearly 30%, demonstrating that this technology works in the real world. However, as has been mentioned earlier, the state of the plastron is key to the magnitude of drag reduction. Thus, experiments where the plastron has degraded have shown decreased or no drag reduction, even causing a drag increase in some cases.

The integrity of the water–air interface of an SHS depends on surface tension. The primary reason for the failure of the interface is increased shear stress (Samaha et al., 2012a; Wexler et al., 2015). When the cavities are flooded with water, instead of acting as drag-reduction sites, they act as roughness elements. This causes an increase in drag instead of the desired drag decrease (Aljallis et al., 2013). Studies have also shown that an increase in turbulent pressure fluctuations (Piao, 2015; Seo et al., 2015) and an increase in hydrostatic pressure, caused by a change in depth, can lead to failure of the interface (Poetes et al., 2010). This effect is pronounced at larger Reynolds numbers (Samaha et al., 2012a).

Yet another factor to take into account is the condition of water in the environment in which the surface is deployed (Xu et al. (2020)). The presence of chemicals that act as surfactants or particulate matter would

degrade the surface and reduce its capability for drag reduction. The physical conditions of the water body (e.g. temperature and salinity) are also factors that could work against SHSs.

While it is obvious that a superhydrophobic surface cannot be used in aerodynamic applications due to the necessity for a liquid-air interface, the points mentioned above make it less lucrative even for applications in water. This is where LISs could bridge the gap, offering reasonably high drag reduction while staying more resilient to flow conditions.

2.5. Liquid-infused surfaces

A carnivorous plant is an unlikely source of inspiration for a drag reduction technique but the *Nepenthes* pitcher plant offers one such idea. Its rim, called the peristome, has a uniform microstructure that captures highly hygroscopic nectar and rainwater within it. This results in high wettability in humid environments, creating a continuous slippery liquid film on the surface. Insects that are lured by the smell emanated by the plant land or walk onto the rim, aquaplane across it and fall into the digestive juices in the cup at the bottom (Bohn and Federle, 2004). The idea of a slippery surface that operates on this principle of liquid-filled cavities has inspired research into using these surfaces in a variety of fields, ranging from anti-fouling, anti-icing and anti-corrosion to drag reduction.

The operation of liquid-infused surfaces fundamentally relies on the same underlying principles as superhydrophobic surfaces. Instead of air trapped in random or organised roughness, this space is now filled by a liquid, thus creating a fluid-fluid interface in the region where it is in contact with the bulk medium. This means that the non-slip boundary condition is eliminated at several points across the surface of the solid, resulting in an effective slip velocity. This has the effect of lowering the velocity gradient of the bulk medium, thereby reducing skin friction drag as it flows over the surface.

2.5.1. Governing parameters

The performance of LISs is governed by properties of both the liquid and the surface it flows over. van Buren and Smits (2017) summarised that the performance of LISs was based on the forces of viscosity, inertia, buoyancy and surface tension. These are the viscosity ratio, Reynolds number, Bond number and Weber number. Since the latter two are responsible for lubricant retention and not the actual drag reduction mechanism, these will be discussed further in Section 2.5.4. Additionally, properties of the surface, such as the shape of the cavities and the area covered by the liquid are also influential.

Viscosity ratio

The viscosity ratio is defined as the ratio of the dynamic viscosity of the external fluid to that of the infused liquid, and is mathematically expressed as:

$$N = \frac{\mu_{\text{ext}}}{\mu_{\text{int}}} \tag{2.15}$$

Viscosity ratios of LISs are typically of $O(1)$, as compared to SHSs that have a value closer to 50. Higher viscosity ratios produce greater drag reduction, and this can be explained in the following manner.

At the interface, both fluids must exhibit the same slip velocity and shear stress.

$$\begin{aligned} \tau_{\text{ext}} &= \tau_{\text{int}} \\ \implies \mu_{\text{ext}} \left.\frac{\partial u_{\text{ext}}}{\partial y}\right|_{y=0} &= \mu_{\text{int}} \left.\frac{\partial u_{\text{int}}}{\partial y}\right|_{y=0} \\ \implies \left.\frac{\partial u_{\text{ext}}}{\partial y}\right|_{y=0} &= \frac{\mu_{\text{int}}}{\mu_{\text{ext}}} \left.\frac{\partial u_{\text{int}}}{\partial y}\right|_{y=0} \\ \implies \left.\frac{\partial u_{\text{ext}}}{\partial y}\right|_{y=0} &= \frac{1}{N} \left.\frac{\partial u_{\text{int}}}{\partial y}\right|_{y=0} \end{aligned} \tag{2.16}$$

In the ideal scenario, skin friction drag could be altogether eliminated if the slip velocity at the interface can be made equal to the freestream velocity of the external fluid.

$$u_s = U_\infty$$

This would result in no velocity gradient at the interface. Thus,

$$\left.\frac{\partial u_{\text{ext}}}{\partial y}\right|_{y=0} = 0$$

Substituting this into Equation (2.16), the condition obtained for maximum drag reduction is:

$$N \to \infty$$

This is akin to the fluid-fluid interface behaving as a shear-free boundary. While this relation is also true for SHSs, the external medium (water) and internal medium (air) are fixed, meaning that N is, for the most part, a constant. With LISs, there is more scope to test the performance of various liquids within the cavities.

Reynolds number

Similar to the observations made using SHSs, high Reynolds numbers induce greater streamwise slip, which causes increased drag reduction. However, this is only true up to a point, after which the high Reynolds number contributes to shear-driven drainage of the lubricant from the surface.

Liquid area fraction

Apart from the properties of the liquid, the surface geometry also has a significant impact on the drag reduction capacity of an LIS. When a larger portion of the surface is covered by fluid, the no-slip condition is removed at more locations. The liquid area fraction a is the ratio of the surface area of the exposed liquid to the total surface area and is used to quantify this. Fu et al. (2017) found that surfaces with equal a but larger features were more effective at drag reduction due to the presence of fewer areas transitioning from a solid to a liquid boundary or vice versa. Regions of high local stresses, where the no-slip condition exists, are thus reduced. However, larger features are also more prone to wetting by the external liquid due to shear-driven failure of the interface, causing a drop in drag reduction capabilities.

Geometry of surface cavities

The geometry of the cavities in the surface holding the lubricating liquid is another factor that determines the drag reduction capability. The most common shapes of these cavities used are in the form of grooves, with studies by Fu et al. (2017) and Arenas et al. (2019) finding that streamwise grooves would provide higher drag reduction than spanwise grooves. The higher streamwise slip induced in the flow in the case of streamwise grooves is the primary mechanism of achieving drag reduction. However, the disadvantage is that the same mechanism will contribute to draining the liquid from the grooves. Kim and Lee (2021), who tested spherical cavities filled with a liquid exposed to a laminar channel flow, noted that the shape of the meniscus (interface) is an important factor. When the deflection of the meniscus is low at low Re, the internal vortex flow rotates in the streamwise direction. However, as the deflection increases with increasing Re, the strength of rotational flow is drastically decreased, and eventually, the rotational direction of the internal flow reverses. Since the motion of the liquid is only driven by the motion of the external flow, this is indicative of flow separation in the external flow above the meniscus, causing an increase in the total drag.

2.5.2. Flow inside a cavity

The net flow that occurs inside the cavity of an LIS is the sum of the contribution from the slip velocity and that from the pressure distribution (p_{int}) in the trapped liquid (Liu et al., 2016). Applying an approximate normal stress balance gives the pressure contributions in the groove as:

$$p_{\text{int}} = p_e + p_L$$

where p_e is the external pressure and p_L is the Laplace pressure. The latter is caused by surface tension and the deformation of the fluid-fluid interface, and is defined as:

$$p_L = -\frac{\gamma}{r}$$

γ is the surface tension and r is the radius of curvature of the interface.

Thus, the total flow profile can be decomposed into three components, driven by:

1. The slip velocity at the interface
2. The pressure gradient caused by the external flow
3. The Laplace pressure gradient

The positive Laplace pressure gradient drives a back flow and works to retain the oil within a groove.

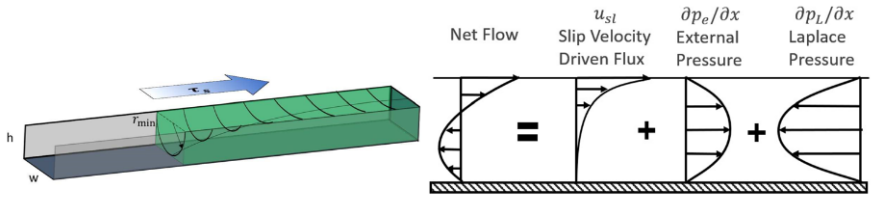

Figure 2.7: Visualisation of the flow inside a cavity, showing the schematic of one groove and the decomposition of the velocity profile at the centre of the groove (Liu et al., 2016)

According to Chang et al. (2019), since the lubricant layer is shear-driven, the skin friction at the interface is equal to the sum of skin frictions on the side and bottom surfaces of the cavity. Fu et al. (2017) goes on to add that the drag reduction effect can be attributed to the presence of the interface. This changes the method of dissipation from turbulent dissipation in the bulk flow to Stokes flow dissipation inside the cavity. Thus, a lubricant, even when $N \approx 1$, can provide a drag reduction so long as the drag reduction as a result of the streamwise slip exceeds the additional viscous drag caused by the lubricant flow within the cavity.

2.5.3. The fundamentals of wetting

In order to understand the interaction between the bulk medium and the liquid-infused surface better, this subsection looks into the underlying mechanism behind surface wetting.

Wetting is a measure of the interaction or contact between a liquid and solid. The more wet a surface is, the larger is the area of the liquid-solid interface. How a surface is wetted depends on the inter-molecular forces between the solid and the liquid (Brown and Mazumder, 2021). These forces can be classified as chemical or physical forces. The chemical forces lead to the formation of ionic or covalent bonds or bonds between atoms, molecules and other functional groups (e.g. metallic bonds) . The physical forces (also known as van der Waals forces) are mostly electrostatic and quantum electrodynamic and have a significantly lower bond energy compared to the chemical forces, around $O(10^2)$ to $O(10^3)$ less.

Solid surfaces themselves can be distinguished as high energy or low energy surfaces. High energy surfaces, such as metals and glass, have strong chemical bonds that require a lot of energy to be broken up. On the other hand, low energy surfaces such as fluorocarbons are bound by weak physical forces.

Liquids can either completely wet or wet only a portion of such surfaces with the interaction being determined through van der Waals forces (Johnson, 1993). These forces have three components:

- Polar interactions between molecules with permanent dipoles
- Induced interactions between molecules with permanent dipoles and non-polar molecules
- Dispersion interactions between all molecules regardless of their polarity

Since the induced interaction is the weakest of the three (Wu, 1982), this can be neglected. Using the Hamaker approach (Israelachvili, 2011), the interaction energy can be used to define the surface tension of a liquid (Equation 2.17), surface free energy of the solid (Equation 2.18) and the reversible adhesion energy between the two (Equation 2.19) as expressed below:

$$\gamma_L = \frac{A_{LL}}{24\pi d_0^2} \tag{2.17}$$

$$\gamma_S = \frac{A_{SS}}{24\pi d_0^2} \tag{2.18}$$

$$E_{SL} = -\frac{A_{SL}}{12\pi d_0^2} \tag{2.19}$$

Here, A is the Hamaker constant with LL, SS and SL representing cohesive self-interactions between the liquid and between the solid, and adhesive solid-liquid interactions respectively. d_0 is the intermolecular spacing.

The degree of wetting between a liquid and a solid surface can be characterised using 2 parameters - the contact angle and hysteresis. While the contact angle defines how a stationary droplet wets a surface, hysteresis indicates how a droplet would move on a surface.

Conceptualised by Young (1805), the contact angle is an equilibrium angle caused by the balance of interaction forces along the three-phase contact line, as seen in Figure 2.9a. It is expressed as

$$\cos\theta_\gamma = \frac{\gamma_S - \gamma_{SL}}{\gamma_L} \tag{2.20}$$

where

$$\gamma_{SL} = \gamma_S + \gamma_L - 2\left(\sqrt{\gamma_S^D \gamma_L^D} + \sqrt{\gamma_S^P \gamma_L^P}\right)$$

Here, P and D represent the polar and dispersion components. For low energy surfaces, there is no polar component ($\gamma_S = \gamma_S^D$). Thus, Equation 2.20 is reduced to

$$\cos\theta_\gamma = -1 + \frac{2}{\gamma_L}\left(\sqrt{\gamma_S \gamma_L^D}\right) \tag{2.21}$$

Thus, surfaces with lower surface energy yield higher contact angles. A surface is considered hydrophilic when the contact angle is less than 90° and hydrophobic when it is above this value. On flat surfaces, the highest contact angle that can be achieved is around 120°. The volume of the droplet whose contact angle is measured is typically between 3 and 10 μm (Huhtamäki et al., 2018).

(a) Wenzel state (b) Cassie state

Figure 2.8: Sketched modes of the wetting behaviour of a droplet on a rough surface (Deng et al., 2018)

In the presence of roughness, the droplet can assume either a wetting state or a suspended state. In the wetting state, formally known as the Wenzel state, the liquid completely wets the solid surface with no air trapped between them. In the suspended state, called the Cassie-Baxter state, air is trapped between the solid and liquid, causing the meniscus to be suspended over the roughness. The contact angle is then given by

$$\cos\theta_c = \sigma_1 \cos\theta_1 + \sigma_2 \cos\theta_2 \tag{2.22}$$

where σ_1 is the fractional area of the surface in contact with the liquid, θ_1 is the contact angle corresponding to a liquid droplet on a flat surface of the same material, σ_2 is the fractional area of the air-filled cavities and θ_2 is the contact angle between the liquid and air. Since

$$\sigma_2 = 1 - \sigma_1 \tag{2.23}$$

and

$$\theta_2 = 180° \tag{2.24}$$

Equation (2.22) can be written as

$$\cos\theta_c = \sigma_1(\cos\theta_1 + 1) - 1 \tag{2.25}$$

Equation (2.25) is known as the Cassie-Baxter equation (Cassie and Baxter, 1944).

The other parameter of importance, hysteresis, characterises the degree of adhesion between the liquid and the surface by placing a droplet on it and tilting it until the drop begins to slide due to gravity. The contact angle hysteresis (CAH) is the difference between the contact angles at the front (advancing angle θ_A) and rear (retreating angle θ_R) of the droplet. Shown in Figure 2.9b, it is expressed as

$$\Delta\theta_{CAH} = \theta_A - \theta_R \tag{2.26}$$

(a) Young's contact angle

(b) Contact angle hysteresis

Figure 2.9: Parameters to characterise the degree of wetting (Brown and Mazumder, 2021)

While the Wenzel state can give high contact angles, it also has a high hysteresis since the liquid penetrates and sticks to the roughness. Thus, SHSs and LISs aim to keep the liquid in the Cassie-Baxter state with a high contact angle and low hysteresis, allowing for droplets to slide easily off them.

2.5.4. Principles behind lubricant retention

Since the depletion of fluid from within the cavities causes the bulk medium to wet the surface and degrade its performance, it is important to understand what the driving factors for lubricant retention are.

van Buren and Smits (2017) identified the Bond number and the Weber number as two key parameters that kept the infused liquid inside the cavities. The Bond number (*Bo*) is the ratio of the buoyancy force to the capillary force. Due to their different densities, the buoyancy force from the external fluid can overcome the capillary force holding the liquid inside the cavity. It is expressed as

$$Bo = \frac{(\rho_{\text{ext}} - \rho_{\text{int}}) g w^2}{\gamma} \tag{2.27}$$

where w is the characteristic length scale (usually groove width), g is the acceleration due to gravity, γ is the interfacial tension, and ρ_o and ρ_i are the densities of the external and internal fluid respectively.

The Weber number (*We*) is the ratio of the inertial force to the capillary force. If the capillary force is not strong enough, the inertia of the external medium allows for the escape of the infused liquid. This is expressed as:

$$We = \frac{\rho_{\text{ext}} {U_\infty}^2 w}{\gamma} \tag{2.28}$$

Thus, having a low *Bo* and a low *We* indicates a system with lower likelihood of failure.

Another important factor is the viscosity ratio N. Liu et al. (2016) found that N affects the retention length of lubricants in longitudinal grooves through the drainage driving force, i.e. the shear stress at the fluid-fluid interface, in laminar flows. This shear stress is related to the viscosity ratio as

$$\tau \approx \frac{1}{1+2DN} \tau_\infty$$

where τ_∞ is the macroscopic wall shear stress and D is the normalised maximum slip length (the ratio of the slip length to the width of the groove).

2.5.5. Experimental investigations for drag reduction

With research on LISs still in a nascent stage, not many experiments have been carried out to verify their drag reduction capabilities in turbulent flows.

Rosenberg et al. (2016) tested the performance of liquid infused surfaces in a Taylor-Couette flow, as shown in Figure 2.10a. A threaded aluminium cylinder (pitch = 106 μm) was used in three configurations - first as a hyrdophilic surface, then as a superhydrophobic surface and finally as a liquid infused surfaces. The liquids used were 2 perfluorinated synthetic oils, which have a higher dynamic viscosity than water, and heptane which is 2.7 times less viscous than water.

The surfaces were tested by spinning the outer cup and measuring the torque on the inner cylinder. Test were carried out at Reynolds numbers from 1700 to 9000, with the flow transitioning to the turbulent state at $Re = 4000$. The Reynolds number was calculated as $Re = \rho_w u(R_o - R_i)/\mu_w$, wherein the subscript w signifies the corresponding values of water. The viscous length scale was calculated to decrease from 19 μm at $Re =$

5900 to 14 μm at $Re = 9000$, meaning that there could have been a riblet effect due to the microscopic size of the threads. However, the authors estimated that this would reduce drag by no more than 2%. To assess the magnitude of drag reduction achieved in the Taylor-Couette setup, the authors calculated it as:

$$DR\,(\%) = \frac{T_0 - T}{T_{0,a}} \times 100 \tag{2.29}$$

where T_0 and T are the torques measured for the control (hydrophilic) and SHS/LIS cylinders, and $T_{0,a}$ is the torque of the control cylinder where the contribution from the fluid it has been subtracted.

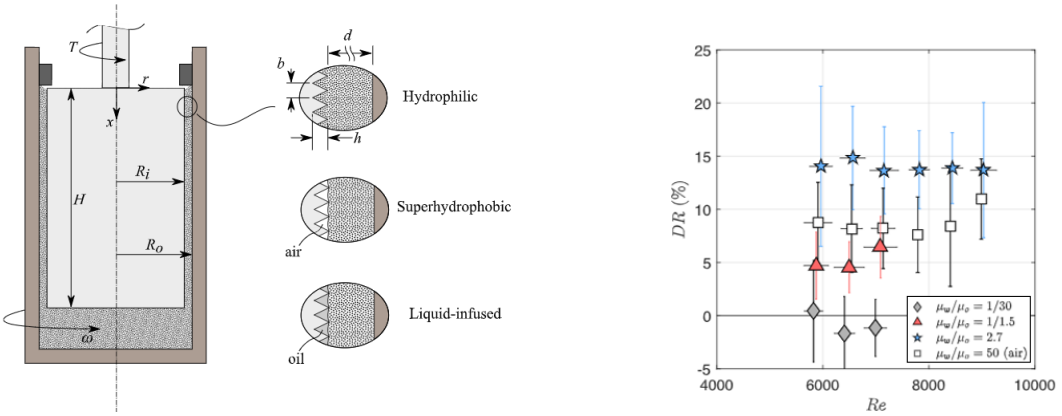

(a) Apparatus

(b) Drag reduction over the SHS and LISs

Figure 2.10: LIS study by Rosenberg et al. (2016)

The results have been shown in Figure 2.10b. It was observed that among the three LISs, heptane, the liquid with the lowest viscosity, produced the largest drag reduction. This value was roughly 14%, as compared to a 5% reduction and a slight increase in the case of the other oils. The SHS gave a reduction of only 10%, which was attributed to surface failure due to the observation of distinct dry and wet patches.

The authors also calculated the slip length of the surfaces by using a semi-empirical logarithmic friction law and applying an offset to the velocity profile in the viscous sublayer. This yielded slip lengths of 71 ± 48 μm for the SHS, 38 ± 33 μm for the less viscous synthetic oil and 138 ± 55 μm for heptane.

Another test in a Taylor-Couette facility was carried out by van Buren and Smits (2017), who used inner steel cylinders that were dip-coated in various alkanes to test the effects of different viscosity ratios. Additionally, the cylinders used had square grooves of width 100 μm, 200 μm, 400 μm and 800 μm to compare drag reduction caused by varying cavity sizes.

Drag reduction was determined as per Equation 2.29, with $T_{0,a}$ being replaced by T_0. The general trend seen for all groove sizes was that higher viscosity ratios produce greater drag reduction. Contrary to what was expected, a few cases appeared where low N produced larger drag reduction. It was believed that, for the lower viscosity oils (implying higher N), instabilities that appeared on the interface caused surface failure (Mohammadi and Smits, 2016). Another trend seen was that larger groove sizes offered greater drag reduction. However, this seemed to be true up to a point because the largest drag reduction was observed at $w^+ \approx 35$. For the largest groove size, at high Reynolds numbers, the drag reduction was seen to decrease with increasing Reynolds number. Visual inspection showed that a portion of the surface had been wetted, implying a partial surface failure. It was concluded that the buoyancy and inertial forces overpowered the capillary force keeping the fluid inside the grooves, causing water to enter them and reduce the magnitude of drag reduction.

2.5.6. Feasibility of LISs in air

Since comprehensive data was not found for investigations carried out using air as the bulk medium, this section analyses whether drag reduction can be expected in air.

A reason why research had not been carried out in air was speculated to be the low viscosity ratio that would be achieved in aerodynamic applications. As explained in Section 2.5.1, greater drag reduction can be achieved when the viscosity ratio N is higher. This would mean that the dynamic viscosity of the bulk

medium should be as high as possible while that of the liquid in the cavity should be as low as possible. With air, this is quite difficult to achieve due to its low viscosity of 1.849×10^{-5} Pa·s at 25 °C. In comparison, most liquids typically have a viscosity that is one or 2 orders higher. Some of the least viscous liquids are n-alkanes, such as hexane (2.949×10^{-4} Pa·s) and heptane (3.890×10^{-4} Pa·s) (at 25 °C). This yields viscosity ratios of 0.063 with hexane and 0.047 with heptane. These values are far lower than the viscosity ratios that have been tested. A comparison can be made to numerical studies, such as the one by Fu et al. (2017), to estimate the possible slip length and hence the possible drag reduction.

Since the lubricant in the cavity moves as per Stokes flow, an expression for the effective slip length is obtained from Schönecker et al. (2014) as:

$$\lambda = \frac{l \ln\left(sec\left(\frac{\pi a}{2}\right)\right)}{\left(c\pi + \frac{1}{2aDN} \ln\left(\frac{1+\sin\left(\frac{\pi a}{2}\right)}{1-\sin\left(\frac{\pi a}{2}\right)}\right)\right)}$$

where l is the periodicity of grooves in the transverse direction, a is the exposed area fraction (ratio of wetted area to total area), c is a constant that is 1 for streamwise grooves or 2 spanwise grooves and D is the normalised local slip length and represents the depth of uppermost eddy inside cavity.

The gas fraction a was set to 0.5, representing equal areas of fluid-fluid and fluid-solid interfaces seen by the bulk medium. Due to D also being directly proportional to λ, this was set at its maximum value of 1. For the analysis, the liquids considered were water, hexane and heptane while the bulk medium was air.

The values of λ/l that were computed were verified against the values present in Schönecker et al. (2014) and a close match was found using comparable viscosity ratios. Using these, the normalised slip length was calculated as

$$\lambda^+ = \frac{\lambda u_\tau}{\nu_{\text{ext}}}$$

In the M Tunnel at TU Delft, which is where the experimental campaigns are scheduled to be run, the maximum value of u_τ is around 1.2 m/s. The kinematic viscosity of air at 25 °C is 1.562×10^{-5} m^2/s. For the value of l, since it is directly proportional to the slip length, it was set to the rather large value (compared to those used in LIS experiments) of 2 mm. Knowing these, the normalised slip lengths were found to be as shown in Table 2.1.

Table 2.1: Expected values for normalised slip length for tests in air in TU Delft's M-Tunnel

Liquid	N	λ/l	λ^+
Water	0.021	0.0012	0.0019
Heptane	0.048	0.0028	0.0042
Hexane	0.063	0.0036	0.0056

Comparing these to the values of expected drag reduction for given normalised slip lengths obtained by Fu et al. (2017), it is seen that the numbers listed above are so small that they are not covered in the discussed range. Very low λ^+ values correspond to minuscule drag reduction, if not a drag increase.

If this exercise were to be repeated for an application in commercial aviation, one would reach a similar conclusion. At cruise altitude, where the temperature is around -50 °C, the dynamic viscosity of air is 3.565×10^{-5} Pa·s. Water-filled grooves would be frozen at this temperature. Assuming that the grooves are filled with hexane, with a viscosity of 7.64×10^{-4} Pa·s, this would result in a viscosity ratio of 0.019. This is even lower than the viscosity ratios analysed earlier, meaning that finding drag reduction is even more unlikely. Thus, it is safe to say that even under ideal conditions, a liquid-infused surface will not be able to produce noteworthy drag reduction for turbulent flow in air.

2.6. Liquid-infused superhydrophobic surfaces

Superhydrophobic surfaces are inherently not capable of operating in flows where air is the bulk medium since the air-filled cavities will merely act as roughness. Also, it has been seen that liquid-infused surfaces cannot produce a discernible level of drag reduction in air. This presents a gap in the design space wherein a concept combining the strengths of these surfaces could be explored. Since a fluid-fluid interface is necessary

for the creation of slip, liquid volumes would need to exist in organised or random cavities on the surface. The mean flow would cause liquid to circulate within the cavities. By making these cavities superhydrophobic, the resistance to the motion of the liquid is significantly decreased, allowing for higher slip velocities at the interface. This concept would thus offer more drag reduction potential than a conventional LIS could. A macroscopic visualisation of the cross section of a LISHyS is provided in Figure 2.11. In this case, the liquid volumes are stored in spherical or cylindrical cavities, thereby creating droplets of the same shape.

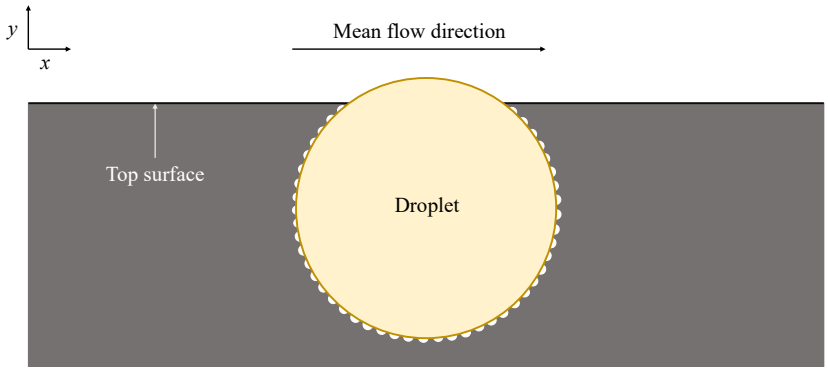

Figure 2.11: Visualisation of the cross-section of a LISHyS

2.6.1. Theoretical framework

While the idea that the presence of slip at the liquid-air interface can lead to drag reduction is supported by results from tests on SHSs and LISs, it is necessary to establish the mechanism by which drag reduction could be achieved for this novel concept. This will help in the identification of the relevant parameters in the design and operation of LISHyS.

Consider two flat surfaces - one with a smooth finish and the other with liquid volumes trapped in it (LISHyS), as shown in Figure 2.12. Let both of them have equal area A that is exposed to the flow. In order to perform a systematic study, let the liquid exist in the form of spheres of defined geometry uniformly distributed over the surface in spherical cavities.

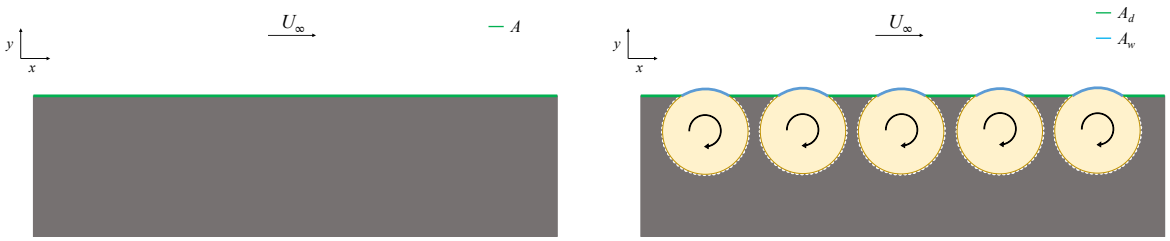

(a) Smooth surface

(b) LISHyS

Figure 2.12: Cross-sections of surfaces for comparison

For the smooth surface, the friction force acting on it can be written as:

$$F_{f,S} = \tau_w A$$

$$\implies F_{f,S} = \mu_{\text{air}} \frac{\partial u}{\partial y}\bigg|_{S,y=0} A$$

For the LISHyS, the friction force can be written as the sum of the friction over the dry portions and that over the wet portions. Let the dry portions exposed to the flow occupy an area A_d and the shear stress over them be $\tau_{w,d}$. Similarly, let the wet portions of the top surface occupy an area A_w and experience a shear stress of $\tau_{w,w}$. Then, the total frictional force acting on the surface is:

$$F_{f,L} = \tau_{w,d} A_d + \tau_{w,w} A_w$$

$$\implies F_{f,L} = \mu_{\text{air}} \frac{\partial u}{\partial y}\bigg|_{L,y=0} A_d + \mu_{\text{air}} \frac{\partial u}{\partial y}\bigg|_{L,a-l} A_w$$

Here, $(\partial u/\partial y)\big|_{L,y=0}$ is the velocity gradient over the dry portion of the surface and $(\partial u/\partial y)\big|_{L,a-l}$ is the velocity gradient over the portion of the surface where an air-liquid interface exists. If the LISHyS is capable of drag reduction, the frictional force over it should be less than that over the smooth surface.

$$\therefore F_{f,L} < F_{f,S}$$

$$\implies \mu_{\text{air}} \frac{\partial u}{\partial y}\bigg|_{L,y=0} A_d + \mu_{\text{air}} \frac{\partial u}{\partial y}\bigg|_{L,a-l} A_w < \mu_{\text{air}} \frac{\partial u}{\partial y}\bigg|_{S,y=0} A \tag{2.30}$$

Since μ_{air} is the same over both surfaces and $A = A_d + A_w$, Equation (2.30) can be rearranged as:

$$\left(\frac{\partial u}{\partial y}\bigg|_{L,y=0} - \frac{\partial u}{\partial y}\bigg|_{S,y=0} \right) A_d < \left(\frac{\partial u}{\partial y}\bigg|_{S,y=0} - \frac{\partial u}{\partial y}\bigg|_{L,a-l} \right) A_w \tag{2.31}$$

Due to the slip velocity over the liquid volumes, air near the dry sections of the LISHyS will be at a higher velocity than over the smooth surface. This would result in a higher velocity gradient over the LISHyS. Assuming that the difference in velocity gradients over the smooth surface and the dry portions of the LISHyS is negligible, the terms on the left side of Equation (2.31) cancel out. This equation then becomes:

$$\frac{\partial u}{\partial y}\bigg|_{L,a-l} < \frac{\partial u}{\partial y}\bigg|_{S,y=0} \tag{2.32}$$

In order to estimate the velocity gradient over the wet portion of the LISHyS (the term on the left in Equation (2.32)), consider the rotation of a droplet inside a cavity in the LISHyS. With the given frame of reference, the effect of the external flow is to rotate the droplet clockwise. This rotation is opposed by the friction inside the cavity (τ_{SHS}). This friction will be smaller than in the case of a smooth surface due to the superhydrophobic coating. The torques acting on the droplet are shown in Figure 2.13.

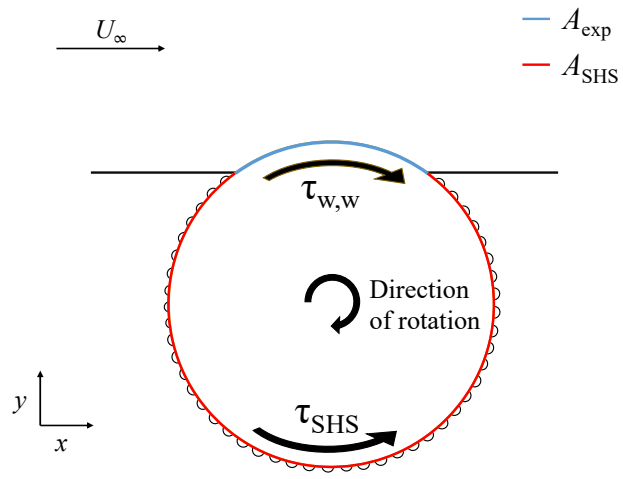

Figure 2.13: Torque acting on a droplet inside a cavity

The torque balance equation for the the droplet is:

$$\tau_{w,w} A_{\text{exp}} r - \tau_{\text{SHS}} A_{\text{SHS}} r = I\alpha \tag{2.33}$$

where A_{exp} is the area of the droplet that is exposed to the flow, A_{SHS} is the area of the superhydophobic surface in the cavity, I is the moment of inertia of the droplet and α is its angular acceleration. Once the system has reached a steady state, the droplet does not experience a change in angular velocity ($\alpha = 0$). Note that a turbulent flow does not reach a steady state, so this is an assumption made to simplify the analysis. Thus, Equation (2.33) becomes:

$$\tau_{w,w} A_{\text{exp}} r = \tau_{\text{SHS}} A_{\text{SHS}} r \tag{2.34}$$

Note that this relation is in agreement with Chang et al. (2019), who found that, for a liquid-infused surface, the skin friction at the interface is equal to the sum of skin frictions on the side and bottom surfaces of a cavity shaped as a longitudinal groove. Equation (2.34) shows that the friction at the the air-liquid interface at the top of the droplet is equal to the friction experienced by it inside the cavity. This equation can be rewritten to show:

$$\tau_{w,w} = \frac{\tau_{\text{SHS}} A_{\text{SHS}}}{A_{\text{exp}}} \tag{2.35}$$

$$\implies \left.\frac{\partial u}{\partial y}\right|_{L,a-l} = \frac{\tau_{\text{SHS}} A_{\text{SHS}}}{A_{\text{exp}} \mu_{\text{air}}}$$

Substituting this relation in Equation (2.32),

$$\frac{\tau_{\text{SHS}} A_{\text{SHS}}}{A_{\text{exp}} \mu_{\text{air}}} < \left.\frac{\partial u}{\partial y}\right|_{S,y=0}$$

or

$$\frac{\tau_{\text{SHS}} A_{\text{SHS}}}{A_{\text{exp}}} < \tau_w \tag{2.36}$$

Due to the directions in which the stresses act on the droplet, a net force in the streamwise direction is created. Referring to Figure 2.13, while the forces along the left and right sides of the cavity would cancel out due to their equal magnitudes and opposite directions, the streamwise components of the forces along the exposed area and the region of the cavity directly below this area would align. The magnitude of the resulting force is given by:

$$F = \left(\tau_{w,w} + \tau_{\text{SHS}}\right) A_{\text{exp}}$$

The effect of this force is to push the droplet into the surface, creating another component of drag. Factoring this into Equation (2.36),

$$\frac{\tau_{\text{SHS}} A_{\text{SHS}}}{A_{\text{exp}}} A_w + n\left(\tau_{w,w} + \tau_{\text{SHS}}\right) A_{\text{exp}} < \tau_w A_w$$

where n is the number of liquid droplets on the surface. Substituting the value of $\tau_{w,w}$ from Equation (2.35),

$$\frac{\tau_{\text{SHS}} A_{\text{SHS}}}{A_{\text{exp}}} A_w + n\left(\frac{\tau_{\text{SHS}} A_{\text{SHS}}}{A_{\text{exp}}} + \tau_{\text{SHS}}\right) A_{\text{exp}} < \tau_w A_w$$

$$\implies \frac{\tau_{\text{SHS}} A_{\text{SHS}}}{A_{\text{exp}}} A_w + n\tau_{\text{SHS}}\left(A_{\text{SHS}} + A_{\text{exp}}\right) < \tau_w A_w \tag{2.37}$$

The wetted area A_w can also be expressed as $A_w = nA_{\text{exp}}$. Substituting this in Equation (2.37):

$$\frac{\tau_{\text{SHS}} A_{\text{SHS}}}{A_{\text{exp}}} nA_{\text{exp}} + n\tau_{\text{SHS}}\left(A_{\text{SHS}} + A_{\text{exp}}\right) < \tau_w nA_{\text{exp}}$$

$$\implies \tau_{\text{SHS}} A_{\text{SHS}} + \tau_{\text{SHS}}\left(A_{\text{SHS}} + A_{\text{exp}}\right) < \tau_w A_{\text{exp}}$$

$$\implies \tau_{\text{SHS}}\left(2A_{\text{SHS}} + A_{\text{exp}}\right) < \tau_w A_{\text{exp}}$$

$$\implies \tau_{\text{SHS}}\left(\frac{2A_{\text{SHS}}}{A_{\text{exp}}} + 1\right) < \tau_w \tag{2.38}$$

Equation (2.38) states the condition necessary for the LISHyS to be capable of drag reduction. The conclusions that are drawn from this relation are as follows:

1. The degree of superhydrophobicity of the cavity is an essential part of the drag reduction mechanism. High hydrophobicity will result in less friction within the cavity, decreasing the value of τ_{SHS}.

2. From the previous statement, it follows that the viscosity ratio between the liquid in the cavities and air within the superhydrophobic features should be as large as possible. As seen in Section 2.5.1, a higher viscosity ratio results in lower friction between the external fluid (the droplet in this case) and the fluid in the roughness elements (air).

3. The contact area between the droplet and the cavity should be minimised. This will occur if a high contact angle can be achieved, once again indicating the need for a high degree of hydrophobicity.

4. The exposed area of the droplet should be increased, decreasing the area that is in contact with the cavity. This has to be done within the constraint that the exposed height of the droplet should not exceed $y^+ = 5$ in order to prevent diverging pressure drag.

5. From Equation (2.31), the area of the portion of the surface that is wetted, i.e. covered by liquid volumes, should be maximised.

The assumptions made in the derivation of this framework are:

- The liquid completely fills the cavity, apart from the air trapped in the superhydrophobic elements.
- The effect of pressure drag is negligible. Drag could arise due to the pressure difference between the upstream and downstream sides of exposed portion of the droplet and air pockets in improperly filled cavities.
- The droplet does not deform and remains in its position within the cavity during rotation. This also means that gravity does not induce torque to affect the rotation of the droplet because the centre of mass remains constant and aligns with the centre of rotation.
- The rotation of the droplet in the cavity reaches a steady state (uncharacteristic of turbulent flow).
- There is no change to the velocity gradient over the dry portions of the LISHyS due to the higher velocity of air present over its wetted portions.

In reality, all of these will act against the drag reduction potential of LISHySs. Thus, the combined effect of the droplets and superhydrophobic surface should be strong enough to counteract these in order to produce a net reduction in drag.

The maximum amount of drag reduction is possible when the droplets rotate at the same velocity as the freestream. In this case, there is no velocity gradient at the air-liquid interface, meaning that the frictional force experienced by the surface would be zero in the wetted portions. Thus, considering the assumptions stated earlier, the drag acting on the surface is only due to the contribution of the frictional force on the dry portions of the surface. A crude estimate of the drag reduction that is possible can made by calculating the maximum portion of the surface that can be covered by liquid volumes. The derivation of this fraction will be carried out in Section 3.2, and is seen to be around 16% for spherical droplets and 40% for cylindrical droplets. Therefore, under ideal conditions, it is expected that LISHySs with cylindrical droplets could experience up to 40% less drag than comparable smooth, flat surfaces, with the expected drag reduction for LISHySs with spherical droplets being significantly lesser.

3

Design and production of surfaces

This chapter discusses the steps involved in the creation of LISHySs. Since it must be ensured that the surfaces are compatible with the testing environment, the aspects relevant to it are covered in Section 3.1. The geometry of the cavities in the surface is detailed in Section 3.2. Then, an assessment of the most suitable techniques to produce LISHySs is carried out in Section 3.3. This is followed by the methodology used to manufacture the surfaces in Section 3.4.

3.1. Considerations for experimental setup

The testing facility where the experimental campaigns were to be carried out was the M-Tunnel at the Low Speed Laboratory (LSL) at TU Delft. The tunnel's test section has a cross-section of 400 mm × 400 mm and a maximum freestream velocity of 35 m/s. The force balance to be used was The Hill, a patented system designed by Dimple Aerospace B.V. that is purpose-designed for skin-friction measurements on flat plates. No velocities lower than 5 m/s would be tested due to the low absolute force on the plate at these velocities (< 0.01 N) and unstable boundary layers in prior experiments. The surfaces to be tested in The Hill (referred to as test plates) would need to be 881.3 mm × 366.1 mm × 5.0 mm in size. The leading edge of a test plate inserted in the Hill is located approximately 0.6 m downstream from the point where the flow is tripped and a fresh TBL starts.

For the design of the surfaces and the experiments, it is important to estimate a few properties of the expected boundary layer over the test plates. δ_v is necessary for inner scaling and predicting the height to which liquid droplets can protrude from the surface. δ is useful in determining the field of view (FOV) in the flow visualisation measurements. Using the relations listed in Section 2.1, contour plots showing the predicted values for these quantities over a flat plate in The Hill are obtained. These are shown in Figure 3.1. A zero pressure gradient (ZPG) TBL and standard atmospheric conditions ($\rho = 1.225 \times 10^3$ kg/m^3, $\mu = 1.81 \times 10^{-5}$ Ns/m^2 and $\nu = 1.51 \times 10^{-5}$ m^2/s) are assumed. $x_{TP} = x + 0.6$, where $x = 0$ is the streamwise coordinate of the start of the TBL.

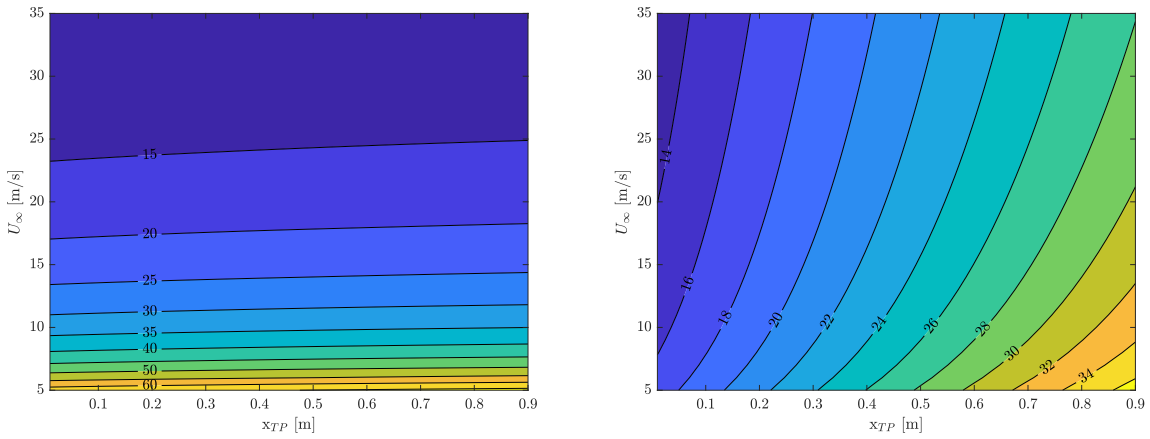

(a) δ_ν [μm] (b) δ [mm]

Figure 3.1: Theoretical values of TBL parameters for a smooth flat plate in The Hill in the M-Tunnel

3.2. Determination of cavity dimensions

An important constraint around which the cavities holding the liquid droplets need to be designed is the height of the exposed portion of the droplets, referred to as the protrusion height (h). Exceeding $y+ = 5$ wall units is expected to cause diverging pressure drag. To allow for a satisfactory tradeoff between ease of manufacturing (favouring larger h) and testing over a higher range of velocities (favouring smaller h), a protrusion height of 100 μm is chosen.

In order to determine the size of the cavity with the required protrusion height, the expressions for the volume of a spherical cap are used. When a plane is passed through a sphere, the shape with lesser volume between the two resulting shapes is known as a spherical cap. This is highlighted in Figure 3.2.

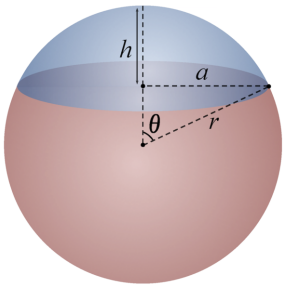

Figure 3.2: Geometry of a spherical cap, shown in blue (Jhmadden, 2015)

Here, h is the height of the cap, a is the radius of its circular base, r is the radius of the sphere and θ is the angle between the top of the cap and the edge of its base, measured at the centre of the sphere. The volume of the spherical cap is given by the following equations:

$$V = \frac{1}{3}\pi h^2(3r - h) \tag{3.1}$$

and

$$V = \frac{1}{6}\pi h(3a^2 + h^2) \tag{3.2}$$

From the right hand sides of Equations (3.1) and (3.2),

$$h(3r - h) = \frac{1}{2}(3a^2 + h^2)$$

$$\implies 6rh - 2h^2 = 3a^2 + h^2$$

$$\implies 3h^2 + 3a^2 - 6rh = 0$$
$$\implies h^2 + a^2 - 2rh = 0 \tag{3.3}$$

The opening ratio OR is defined as the ratio of the radius of the cap to that of the sphere. Thus,

$$OR = a/r$$
$$\implies a = OR \cdot r$$

Substituting this in Equation (3.3),

$$h^2 + (OR \cdot r)^2 - 2rh = 0$$

Solving this as a quadratic equation in r,

$$r = \frac{2h \pm \sqrt{4h^2 - 4h^2 \cdot OR^2}}{2OR^2}$$
$$\implies r = \frac{2h \pm 2h\sqrt{1 - OR^2}}{2OR^2}$$
$$\implies r = \frac{h\left(1 \pm \sqrt{1 - OR^2}\right)}{OR^2} \tag{3.4}$$

Thus, apart from the protrusion height, the radius of the cavity depends upon the selected opening ratio.

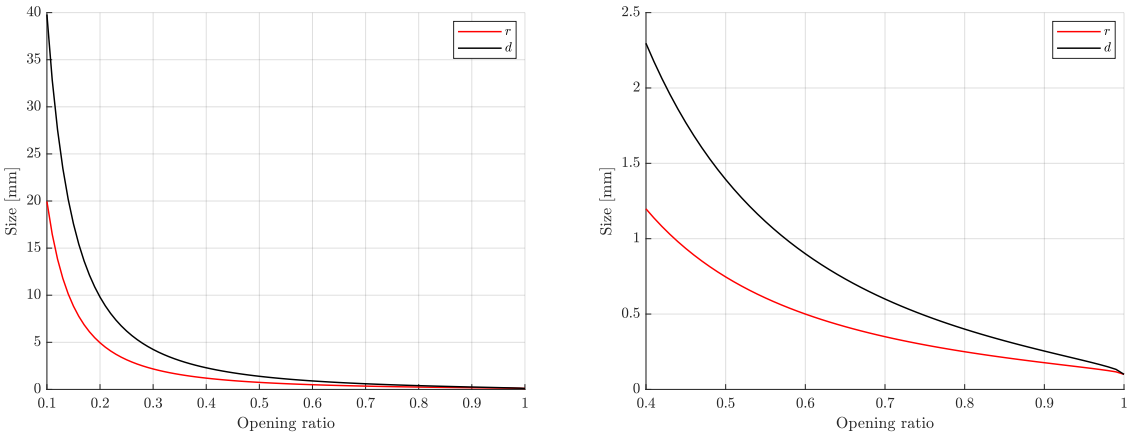

(a) For $0.1 < OR < 1$

(b) For $0.4 < OR < 1$

Figure 3.3: Possible cavity dimensions (r: Radius, d: Depth)

Figure 3.3a shows the dimensions of the cavity as a function of the opening ratio. The cavity depth d is the distance from the bottom of the cavity to the the base of the spherical cap, and is calculated as:

$$d = 2r - h$$

To show the dimensions for higher opening ratios more clearly, Figure 3.3b has been plotted. The calculations use the sum instead of the difference of the terms in the brackets in Equation (3.4) because the latter results in cavity radii in the order of $O(10^{-7})$ to $O(10^{-4})$ m. These would pose a bigger challenge during the manufacturing of the surface.

Both figures show a rapid drop in the sizes of the necessary cavity with increasing OR, decreasing from $O(10^{-2})$ to $O(10^{-4})$ m. This is because a cavity that is more exposed (higher OR) must have a smaller radius in order for the sphere it holds to stay within the protrusion height.

With this knowledge, it is possible to calculate the total area available on a test plate in the selected drag measurement setup that can be covered by such cavities. Apart from their dimensions, the arrangement of the cavities and the distance between them are important for this calculation. The options when it comes to the pattern in which the cavities are arranged are as follows:

- A square pattern, in which cavities are equally spaced laterally and longitudinally
- A staggered pattern, in which cavities of one row are laterally offset by half the periodicity of the pattern from the previous row
- A hexagonal pattern, in which one cavity is surrounded by six cavities at the nodes of a regular hexagon

Note that in all three cases, the minimum centre-to-centre distance between the cavities remains the same.

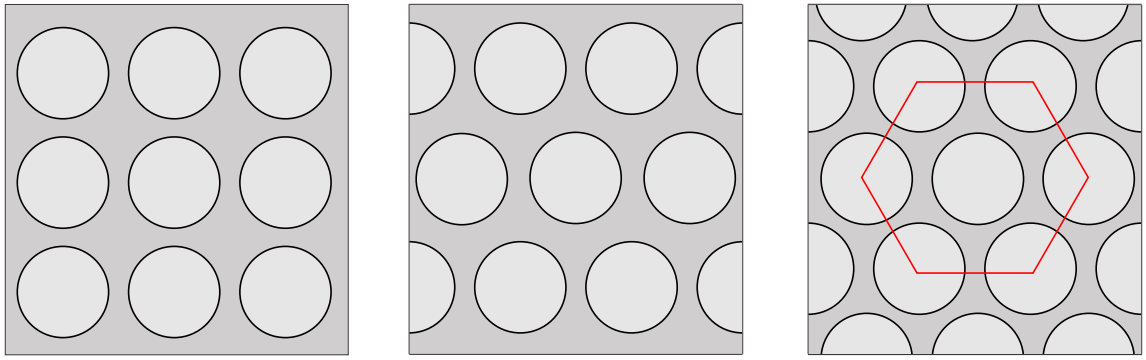

(a) Square pattern (b) Staggered pattern (c) Hexagonal pattern

Figure 3.4: Patterns for cavity arrangement

Figure 3.4 shows how these arrangements would look like when the cavities are viewed from above. It is evident that the hexagonal pattern packs the cavities as closely as is possible; Figure 3.4c incorporates the highest number of cavities in the same area. This allows for a larger number of cavities on the surface, increasing the area that is covered by liquid.

The final factor that must be considered in the calculation of liquid area is the distance between neighbouring cavities. This is essentially the minimum thickness of the wall that separates adjacent cavities. In order to increase the area of the surface that is covered by liquid, a low wall thickness is desirable as this brings the cavities closer together, allowing for more of them on the surface. However, if the walls are too thin, there is a risk of these structures failing. This would change the geometry of the cavities and disrupt the motion of the liquid within them. Thus, the wall thickness is fixed at 0.5 mm to keep options open with regards to manufacturing techniques.

Figure 3.5 shows the liquid fraction as a percentage of the total area of the plate, expressed as a function of the opening ratio. The circular area is the combined planar area of the top of the cavities. The circular liquid fraction CLF, indicated in red, is then calculated as:

$$CLF = \frac{\text{Number of cavities} \times \pi a^2}{\text{Area of the corresponding flat plate}} \times 100$$

The spherical area is the total area of all the spherical caps that are present on the surface. In order to account for the additional area created due to the non-planar geometry, the spherical liquid fraction SLF, shown in black, is calculated as:

$$SLF = \frac{\text{Number of cavities} \times \pi(a^2 + h^2)}{\left(\text{Area of the corresponding flat plate} \times \left(1 - \frac{CLF}{100}\right)\right) + \text{Number of cavities} \times \pi(a^2 + h^2)} \times 100$$

It is observed that the liquid fraction increases up to $OR = 0.7$ when considering the circular area and $OR = 0.8$ when the spherical area is considered, following which a reduction occurs. Thus, referring to Figure 3.3b, the ideal cavity dimensions would correspond to a radius of 250 μm and height of 400 μm. There are some clear concerns with having such a geometry. These are:

1. Using a high OR exposes more of the spherical droplet to the flow. Due to the shallower cavity, there is a higher chance of the droplet being carried away with the flow.

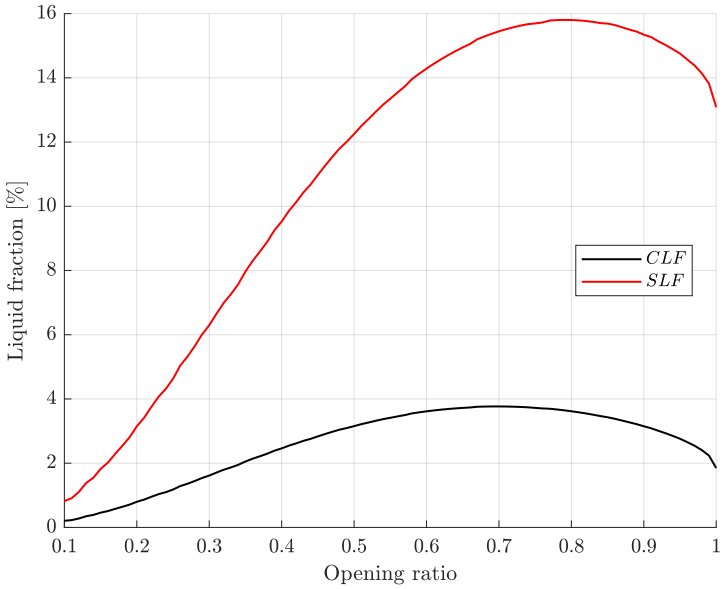

Figure 3.5: Liquid fraction obtained using a hexagonal pattern

2. A droplet of radius 250 μm has a volume of 0.065 μl. To get an idea of how small this figure is, it is the quantity of 1 of 7.5 million parts of water in a teaspoon. As a lower mass of liquid will evaporate more quickly, the plate may be devoid of liquid before any meaningful test has been carried out.

3. Having such a fine geometry severely restricts the options for manufacturing because the number of techniques that can be used to accurately produce a feature this small is low. Additionally, the tolerance needed to produce such a feature would be in the order of a few micrometres, which would drive up production costs.

Thus, a trade-off needs to be made between achieving a high liquid fraction and creating a feasible design. It is decided that using cavities with $OR = 0.5$ would result in a manufacturable design while allowing for a large liquid fraction. In terms of cavity dimensions, this corresponds to a radius of 746 μm and depth of 1392 μm. The liquid fraction achievable will then be around 12.25% (SLF).

Since previous studies (Fu et al., 2017; van Buren and Smits, 2017) on LISs have shown that surfaces with a higher liquid fraction have higher drag reduction potential, it is of interest to test whether this relationship holds for LISHySs as well. A surface with grooves oriented normal to the freestream velocity, i.e. along its span, would allow for the rolling motion of liquid volumes within them. Instead of rolling spheres in the cavities, the grooves would be filled with cylindrical fluid volumes. Doing so considerably increases the liquid fraction for all opening ratios, as seen in Figure 3.6.

The rectangular liquid fraction is equivalent to CLF, and is calculated as the ratio of the sum of the rectangular areas at the top of all cavities to the area of the corresponding flat plate. This is expressed as:

$$RLF = \frac{\text{Number of grooves} \times 2al_g}{\text{Area of corresponding flat plate}} \times 100$$

where l_g is the length of a groove and is calculated as:

$$l_g = \text{Test plate breadth} - (2 \times \text{Wall thickness})$$

The cylindrical liquid fraction is equivalent to SLF and uses the area of the exposed portions of the cylindrical liquid volumes. It is expressed as:

$$CyLF = \frac{\text{Number of grooves} \times 2\theta r l_g}{\left(\text{Area of the corresponding flat plate} \times \left(1 - \frac{RLF}{100}\right)\right) + \left(\text{Number of grooves} \times 2\theta r l_g\right)} \times 100$$

Figures 3.5 and 3.6 show similar trends with maximum values of the liquid fraction corresponding to an opening ratio of around 0.7. For the reasons given in the design of spherical cavities, $OR = 0.5$ is decided as

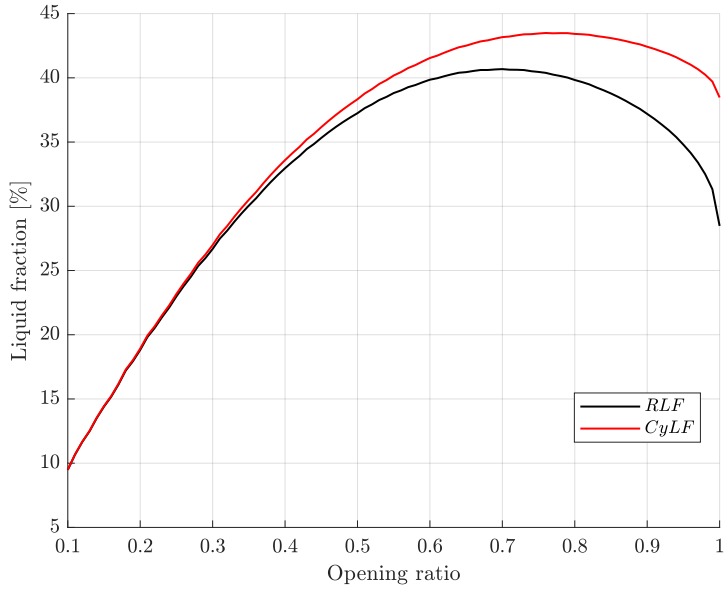

Figure 3.6: Liquid fraction obtained using cylindrical spanwise cavities

being ideal for manufacturing while potentially allowing for drag reduction. This will also enable for a comparison to be made between spherical cavities and cylindrical cavities with similar geometrical parameters. The liquid fractions corresponding to $OR = 0.5$ are $RLF = 37.27\%$ and $CyLF = 38.33\%$. Looking at these numbers, it is immediately evident that a test plate with cylindrical droplets would have significantly higher liquid coverage than one with spherical droplets.

3.3. Selection of manufacturing technique

The production of a liquid-infused superhydrophobic surface is a three stage process:

1. The production of the geometry with macroscopic cavities
2. The conversion of this geometry into a superhydrophobic surface
3. The infusion of the lubricating liquid

This process can be reduced to two steps by making the initial geometry out of a superhydrophobic material but due to the complexities and high costs involved in creating a test plate of the required size, it is simpler to build a LISHyS in three steps.

3.3.1. Base surface

The first step is the production of the cavity-laden geometry. Since the aim is to create surfaces that are compatible with The Hill, two flat plates - one with spherical cavities and another with cylindrical, spanwise cavities - would need to be created. The following manufacturing techniques were considered:

- **Milling**
  A Computer Numerical Control (CNC) milling machine uses instructions in the form of G-code to accurately move a machining tool and/or workpiece to create the desired geometry. From one block of a material such as aluminium, a tool like a ball end mill can be used to create grooves. In order to create spherical cavities, the surface could be made in 2 pieces, one containing the upper portion of the cavity and the other with the lower portion. These could then be fastened together to ensure that the upper and lower portions are aligned. Using a milling machine ensures a smooth finish on every surface.

- **Chemical etching**
  Chemical etching is the process of removing material from a surface using a reagent. Certain portions of the surface are covered by a material that is non-reactive to the reagent and protects the surface, while the rest of it is "eaten away". While it is not possible to create a macroscopic 3D feature such as a spherical cavity or a groove in this manner, it could be used to create patterns in sheets of material. For example, a spherical cavity could be made by creating circular holes of increasing and then decreasing sizes in successive sheets, which would then be placed one on top of the other. The sheets could be glued or fastened together in order to maintain the alignment of the holes.

- **Laser cutting**
  A CNC laser cutter uses a focused beam of light to melt and vaporise material from a workpiece. This process can be used to create cylindrical or cuboidal slots in a sheet of acrylic or wood. A plain sheet of acrylic would have to be placed below this to close the slots because the laser removes material from the entire depth of the sheet that is being cut. If sheets of the desired thickness cannot be acquired, these would need to be face milled using a milling machine. In order to ensure that only the desired portion of the liquid volume is exposed to the flow, a thin sheet of vinyl or acrylic with smaller circular holes or slots would need to be placed on top of the slotted sheet.

- **3D printing**
  Unlike the processes mentioned above that remove material from a workpiece, 3D printing is an additive process. G-code is used to control the locations where material is to be deposited in a layer by layer manner. There are several categories of this technique, ranging from Fused Deposition Modeling (FDM) and Selective Laser Sintering (SLS) to Stereolithography (SLA). SLA, in particular, can achieve very fine tolerances as it uses a light source to cure liquid resin into hardened plastic. Since finding an SLA printer with the capability to print the entire plate in one operation is infeasible, it would need to be made in smaller pieces that are then joined together.

Renderings of the surfaces produced by these techniques have been provided in Appendix A for more clarity. Among the processes mentioned above, milling and 3D printing would be able to replicate the ideal design of the plate most closely. The plates created by etching and laser cutting would leave spaces between the surface and the droplet. This would be detrimental to maintaining the shape of the droplet and could act as a source of pressure drag. Additionally, due to the fine size of the features, any misalignment during the sheet stacking process using either technique would result in a deformed droplet. Thus, chemical etching and laser cutting were ruled out. While an attempt was made to mill the plates, acquiring a specialised ball end mill tool to create the cavities proved to be difficult. An estimated cost upward of €2700 to mill a single plate was quoted by a supplier, further discouraging the usage of this method. Thus, it was decided to 3D print both plates using an SLA printer. While being able to produce detailed features, 3D printing provided the additional advantage of maintaining complete control over the manufacturing process. This would reduce the chances for a part to be produced incorrectly or a delay to occur during shipping.

3.3.2. Superhydrophobic coating

The second step of the LISHyS production process is to make the printed surface superhydrophobic. This is done by the application of a sprayed coating. This is also connected to the third step, which involves the infusion of the liquid, because the selection of the liquid and the coating cannot be made independently. The advantage of using an oil, such as silicone oil or commercial lubricants, over water is that it would not be as susceptible to evaporation. However, SHSs are usually not as effective against oils, apart from the aforementioned silicone oil. Oils also have the potential to destroy the superhydrophobicity of the surface if they cannot be completely removed after application. Four coatings were assessed, which were as follows:

- **Clothing spray** (SMW Anti-Rain Protector)
  Ideally suited for shoes, bags and jackets made from polyester and leather, this is the most economical option. Once coated with a thin layer of silicone, the surface turns hydrophobic within 30 minutes. However, its adherence is low, meaning that the surface must be resprayed often.

- **Automotive spray** (Wowo's Crystal Sealant)
  This spray forms a cross-linking nanosiloxane mesh on the exterior panels of cars, rendering them hydrophobic. The spraying process is simple and the coat adheres strongly with a single application.

- **Marine hull spray** (Profluid Marine PF Protec 206)
  Intended for usage on plastic, metallic and rubber surfaces on the hulls and other parts of boats, this silica spray can be used in both freshwater and saltwater environments. This coating is also extremely durable.

- **Industrial coating** (Ultra Ever Dry)
  This coating is applied in the form of two layers and gives the surface a hazy white finish. It can be applied on a multitude of surfaces, including metals, glass, textiles and concrete. However, it is the most expensive option and requires the longest drying time.

Tests for hydrophobicity were done on flat aluminium samples. The surfaces were sanded with 240 grit sandpaper to remove any surface defects and then separately sprayed with each coating. After 2 hours of waiting time, a syringe was used to place fine droplets of distilled water on them.

(a) Clothing spray

(b) Automotive spray

(c) Marine spray

(d) Industrial coating

Figure 3.7: Samples with trial coatings

As seen Figure 3.7, it is evident that only the industrial coating produced a surface that can be deemed to be superhydrophobic. The clothing and automotive sprays produced droplets with contact angles close to 90°. Droplets on the surface coated with marine spray were seen to completely wet the surface. Following this, tests were also carried out with silicone oils of different viscosities on the same surfaces. While the oil drops were still present a full day after they were placed on the samples, they were seen to wet the surfaces. More significantly, they destroyed the effectiveness of the coatings locally, causing them to be hydrophilic in those regions.

A trial was also made on the usage of sandpaper to increase hydrophobicity. It was hypothesised that the inherent roughness of sandpaper would further increase the contact angles formed between the liquid droplets and the surface. Images of these tests can be found in Appendix B. While there was a visible improvement in the shape of the droplets, incorporating sandpaper into the production of the base material proved to be too big of a challenge. Thus, it was decided that the 3D printed base pieces would be sprayed with the industrial coating.

3.3.3. Liquid infusion

The last step in the creation of a LISHyS is infusing the liquid into the superhydrophobic cavities in the base material. This is expected to be the most challenging part of the process because the aim is to force water into features that are specifically built to resist them. Additionally, because the cavity geometry "closes in" on itself, it is hard for water droplets to enter the cavities.

Several studies that created LISs (Rosenberg et al., 2016; van Buren and Smits, 2017; Sun et al., 2021) first created a superhydrophobic surface that was then coated in an oil. In these cases, the wetting of the microscopic cavities by the oils was preferred because this enhanced their retention. This is in line with the criteria determined by Wong et al. (2011) necessary for the manufacture of LISs, which are:

1. The lubricating liquid must wick into, wet and stably adhere within the substrate.
2. The solid must be preferentially wetted by the lubricating liquid rather than by the liquid one wants to repel.
3. The lubricating and impinging test liquids must be immiscible.

In the current study, water cannot be allowed to wet the surface so an alternative method of infusion was needed. The vaccuum impregnation technique used by Wu et al. (2019) to infuse an anodised alumnium oxide (AAO) surface with mineral oil was considered. While their technique was used to suck oil deep into nanochannels, it may have been possible to use this to suck water into the spherical or cylindrical cavities on the surface. Figure 3.8 shows the setup and process of the technique. The apparatus consisted of a cylindrical container, which held the substrate, and was connected to a vacuum pump, an air-exhaling valve, an air-inlet valve, and an oil-inlet valve. After placing the surface in the container, the air-inlet valve was closed, the exhaling valve was opened and the container was vacuumed to remove the air in the container and in the nanochannels. The oil-inlet valve was then opened till the sample was submerged in mineral oil. Soaking under vacuum for 1 hour allowed the lubricant to thoroughly fill the nanochannels. The air-inlet valve was then opened, allowing air into the container and pushing the lubricant deep into the channels. Finally, the surface was placed at 45° for 5 minutes to remove the excess lubricant on the surface.

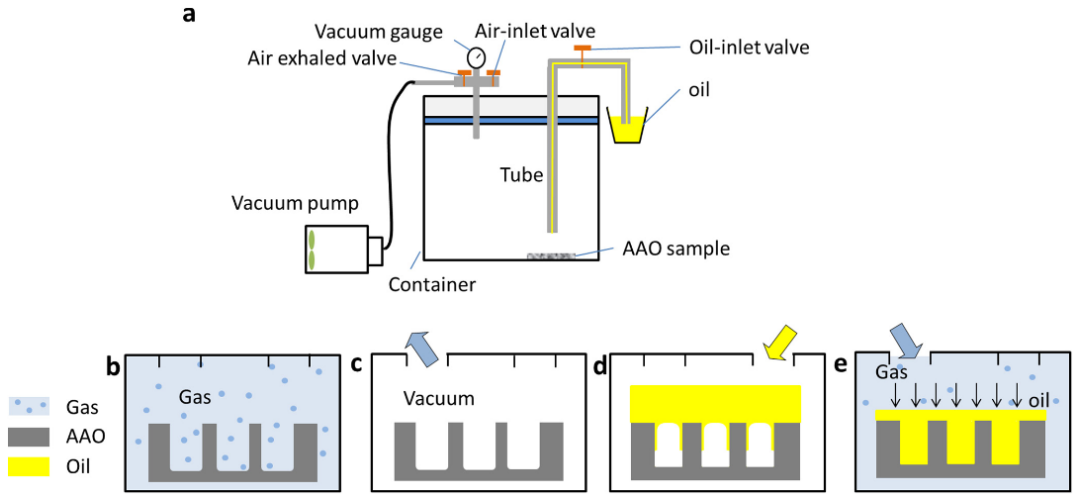

Figure 3.8: Lubricant impregnation. Figure (a) shows the setup and Figures (b) to (e) show the steps in the process (Wu et al., 2019)

While this technique was initially lucrative, there was also the strong possibility of the loss of superhydrophobicity from the cavities. During the vacuuming process, if air was sucked out of not just the cavities but also the microscopic features of the coating, it would no longer repel water. Any droplets that would then flow into the cavities would then merely wet them, turning the surface into a LIS with added internal roughness.

Finally, it was decided to infuse the surface with water by spraying it as a fine mist using a plant sprayer. Tiny water droplets were expected to aggregate inside the cavities, creating droplets of the necessary size inside them. Excess water on the parts of the surface that need to be dry could be removed by tilting the surface and letting them roll off.

3.4. Production of surfaces

This section discusses the production of the LISHySs needed for the experimental campaigns. Having identified the most suitable techniques to manufacture the test plates in Section 3.3, the printing of the base surface is covered in Section 3.4.1. This is followed by the process of making the printed surface superhydrophobic via the chosen coating in Section 3.4.2. The assembly of the test plates is described in Section 3.4.3 and the infusion of water into them is covered in Section 3.4.4. Finally, Section 3.4.5 determines whether the finished surfaces meet expectations from the point of view of production. For convenience, future references to the test plates are henceforth denoted by P-SC for the plate with spherical cavities and P-CC for the one with cylindrical cavities.

3.4.1. 3D printing

The 3D printer used to make the base surface was the Prusa SL1S Speed. This printer uses the technique of Masked Stereolithography Apparatus (MSLA) to create finely-detailed geometries. Similar to SLA printing, MSLA cures photosensitive resin held in a tank by exposing it to ultraviolet light in a layer-by-layer manner, building the part from the bottom upwards. The difference between the two is that while SLA uses a controlled laser beam to trace each layer, MSLA uses a large UV light source which is selectively masked with an LCD screen, allowing for only a certain portion to be cured. The material out of which the surfaces were made was Prusament Tough resin.

The first step in the 3D printing process is the design of the individual pieces that need to be printed. This was done using CATIA 3DEXPERIENCE. Using the geometrical parameters arrived at in Section 3.2, designs were created through the Part Design interface. Since the entire test plate could not be produced at once, smaller pieces, called tiles, were individually printed and then assembled together to form test plates. The sizes of the tiles were restricted by the printer's build volume. In all, 6 designs were created - 3 each for P-SC and P-CC. Along with a square tile, 2 designs with one corner being rounded were created. This allowed the assembled test plate to fit perfectly inside the tray of the force balance. In all, one test plate was created with 17 square tiles and 4 tiles with one corner rounded. The dimensions for these tiles were determined based on trials with smaller samples, and have been shown in Figure 3.11.

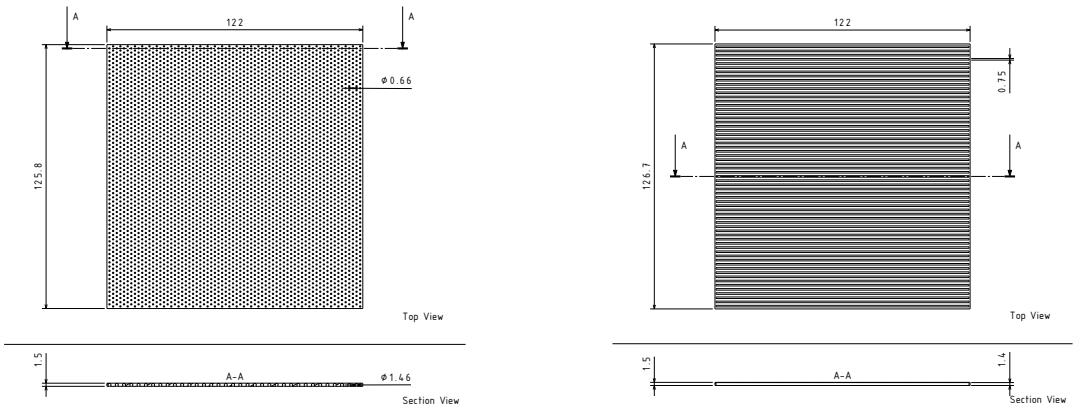

(a) Spherical cavities

(b) Cylindrical cavities

Figure 3.9: Test plate tile dimensions

After exporting these designs as STL files, PrusaSlicer was used to virtually place the tiles on the build plate of the printer, as seen in Figure 3.10. A layer height of 25 μm was used to produce the cavities with the highest resolution. Supports at the base of the prints were found to be necessary as the tiles were seen to detach from the bed otherwise due to the small contact area. The settings used have been listed in Table 3.1. In order to optimise print time, 5 tiles were printed at once. More could not be placed due to the printer's build volume constraints.

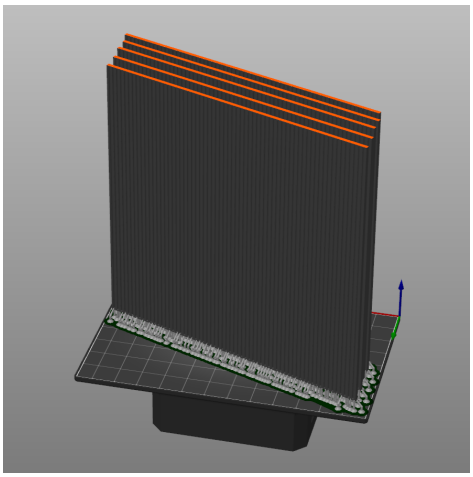

Figure 3.10: Virtually placed tiles in PrusaSlicer

Table 3.1: Print settings on PrusaSlicer

Parameter	Value
Layer height	25 μm
Layer exposure time	2 s
Initial exposure time	25 s
Pad wall thickness	1 mm
Support pinhead width	3 mm
Support pinhead penetration	0.5 mm

Once the prints were complete, the excess resin was wiped off using paper towels. Next, the tiles were dipped in a TPM (Tripropylene glycol monomethyl ether) bath, followed by a rinse in the TPM ultrasonic cleaner for 10 minutes. This allowed for the removal of excess resin from inside the cavities. Next, they were dipped in an IPA (Isopropyl alcohol) bath to remove the TPM. This was necessary because if the TPM samples were directly washed with water, a white residue was deposited on the surfaces. A water wash for 10 minutes was then carried out to remove any remaining TPM and IPA. After wiping the prints with paper towels again, they were dried in an oven at 35° for 6 hours to remove any remaining moisture. While the post-processing of an MSLA print typically ends by curing the part in the UV curing machine, it was decided not to do this as it could have led to stiff, curved tiles, which would have hindered their assembly. Images of the apparatus can be seen in Figure 3.11. In all, the time needed to produce 5 tiles was close to 14 hours, as outlined in Table 3.2.

Table 3.2: Time required to produce a printed tile

Step	Activity	Time (minutes)
1	Print	420
2	Wipe with paper towels	5
3	Dip in TPM bath	5
4	Ultrasonic wash in TPM	10
5	Dip in IPA	5
6	Rinse in water wash	20
7	Wipe with paper towels	5
8	Dry in oven	360
	Total	830

(a) (b) (c) (d) (e)

Figure 3.11: 3D printing apparatus: (a) Prusa SL1S Speed printer and Prusament Tough resin, (b) IPA and TPM baths, (c) HBM GL Serie 4 Litre ultrasonic cleaner, (d) Formlabs Form wash, (e) Hendi 229064 drying oven

3.4.2. Application of the superhydrophobic coating

The coating chosen was Ultra-Ever Dry, an industrial superhydrophobic and oleophobic coating that repels most water-based and some oil-based liquids. This is applied in the form of 2 layers. The bottom layer is a mixture of xylenes, tert-butyl acetate, acetone, polymers and additives. It bonds to the base material and acts as a primer, providing a consistent surface for the top layer to adhere to. The top layer is a similar mixture of acetone, amorphous silica and additives. When this is sprayed, it interacts with the bottom layer to create a finely textured surface with billions of interstitial spaces. The peaks of the patterns in the surface help in lowering its surface energy, decreasing the contact area between the droplets of water and the coating. The portion of the droplet that does not touch a peak is held together by intermolecular cohesive forces. This results in nearly spherical droplets, as seen in Figure 3.12.

Figure 3.12: Droplets on a flat surface coated with Ultra-Ever Dry

Figure 3.13: Constituents of the coating's test kit

The coating was purchased as a test kit, which included 500 ml each of the bottom and top coats, two Preval sprayers and 420 ml of xylene, as shown in Figure 3.13. The application procedure was as follows:

1. The bottom coat was shaken for 10 minutes to evenly distribute any solids that may have settled in the container.
2. The coat was poured into the fluid cup attached to the sprayer until it was two-thirds full.
3. Three thin coats were applied to each piece of the plates. Between passes, the fluid cup was swirled to maintain agitation. The direction of application was changed for each pass to reach into as much of the cavities as was possible, and efforts were made to avoid pooling.
4. The pieces were allowed for dry for 1 hour. During this time, the excess liquid in the fluid cup was poured back into its container, and the sprayer was cleaned with xylene and allowed to dry.
5. The top coat was shaken for 5 minutes. This was poured into the fluid cup of the other sprayer in order to avoid any chance of the coats mixing inside it and clogging it up.
6. 3 coats were sprayed onto the pieces in the same manner as for the bottom layer, followed by a cleanup of the apparatus. A hazy white layer was seen to begin forming as soon as the top coat came into contact with the surface.
7. For maximum hydrophobicity, the pieces were allowed to dry overnight.

Spraying of the coating was done at the spray booth in the student workshop at the High Speed Laboratory in TU Delft. Since the booth was not large enough to accommodate the entire test plate at once, tiles were sprayed with the coating once they had been taken out of the oven. Necessary protection, namely latex gloves, a face mask and glasses, were worn during the process to prevent contact between the coating and skin.

3.4.3. Assembly of test plates

An acrylic plate of thickness 3.4 mm was used as the surface on which the tiles were assembled. This provided a solid base for the tiles while also reducing the amount of resin needed by decreasing the required thickness of the tiles. This plate was made slightly smaller than the dimensions of the tray of the drag measurement

device to provide leeway during assembly and while being fit into the device. Clear double-sided 3M tape of thickness approximately equal to 0.1 mm was used to stick the tiles to the acrylic. Strips of tape were cut and laid in the spanwise orientation adjacent to one another so that the entire acrylic plate was covered with tape. Once all the tiles had been placed approximately, the test plate was placed in the device and the tiles were adjusted such that there were no gaps between their outer edges and the walls of the tray.

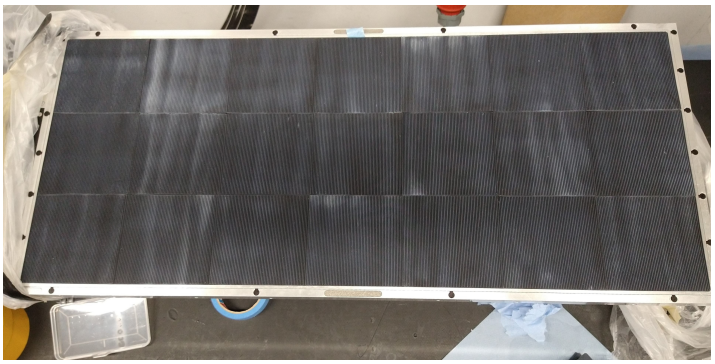

(a) A view of the entire test plate

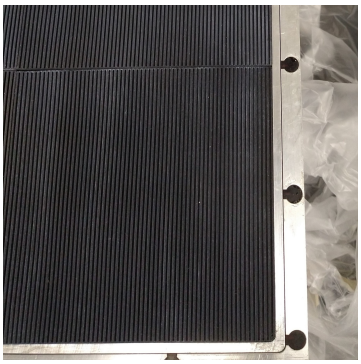

(b) Zoomed-in view at the leading edge

Figure 3.14: Checking the fit of P-CC in the drag measurement device

The internal gaps between the tiles were then filled with acrylic kit (Wekem Multiflex). This is commonly used as a sealant in home applications to make spaces watertight. Painter's tape and a cartridge gun were used to guide the kit into the gaps between the tiles, preventing it from spilling onto the superhydrophobic surface. Figure 3.15 shows the assembled plate prior to and after application of acrylic kit.

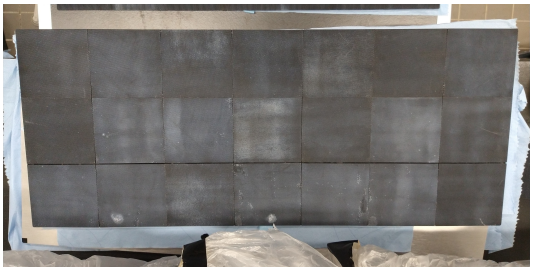

(a) Before application

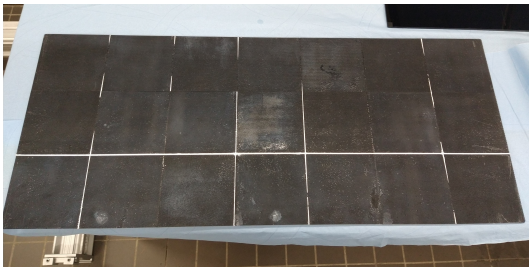

(b) After application

Figure 3.15: Application of acrylic kit on P-SC

3.4.4. Infusion of water

The cavities in the two test plates were filled with distilled water in order to prevent their contamination with mineral salts or organic compounds upon evaporation. This was sprayed using a commonly available plant sprayer. To minimise the loss of water from the cavities due to evaporation, spraying was performed immediately before they were subject to the tests.

P-SC was tilted about the streamwise axis by close to 90° for spraying. This forced water into the cavities while allowing for the excess to drain off. The droplets that remained on the top surface were removed using a handheld air blow gun fitted with a pressure regulator. Views of the water-infused tile are shown in Figure 3.16.

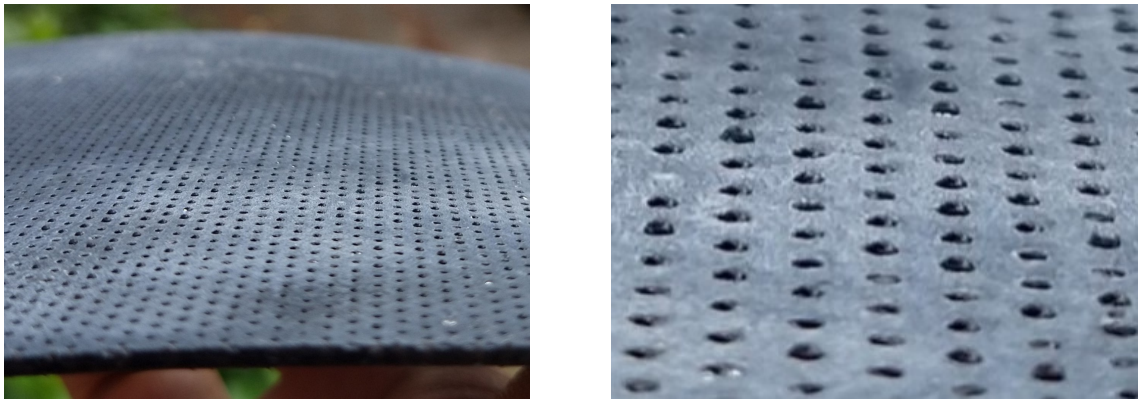

(a) Wide view (b) Zoomed-in view

Figure 3.16: A tile with water infused

For P-CC, it was observed that tilting the plate caused the water in the cavities to coalesce at one end and escape from them. Thus, this plate needed to be kept as level as possible once it had been filled with water. The ideal method involved spraying the plate once it had been installed in the measurement device. Thus, the exposed portions of the wooden boards that made up the wind tunnel walls in the vicinity of the measurement device were covered with duct tape prior to spraying.

3.4.5. Validation of surfaces

In order to check how well the produced surfaces compared against the ones that were designed, it was necessary to measure a few parameters. Firstly, the dimensions of the cavities in the test plates were checked using a Keyence VR-5000 wide-area 3D measurement system at the Physics Lab in Delft Aerospace Structures and Materials Laboratory (DASML). As seen in Figure 3.17a, the diameter of the spherical cap was seen to be close to that of the designed surface (0.75 mm). Figure 3.17b shows that the diameters of the produced cylindrical cavities was almost identical to the design value of 1.5 mm. While the measurement system is capable of measuring the depth of features, the bottom of the cavities could not be seen clearly due to the manner in which the curved and reflective surfaces scattered light rays from the system.

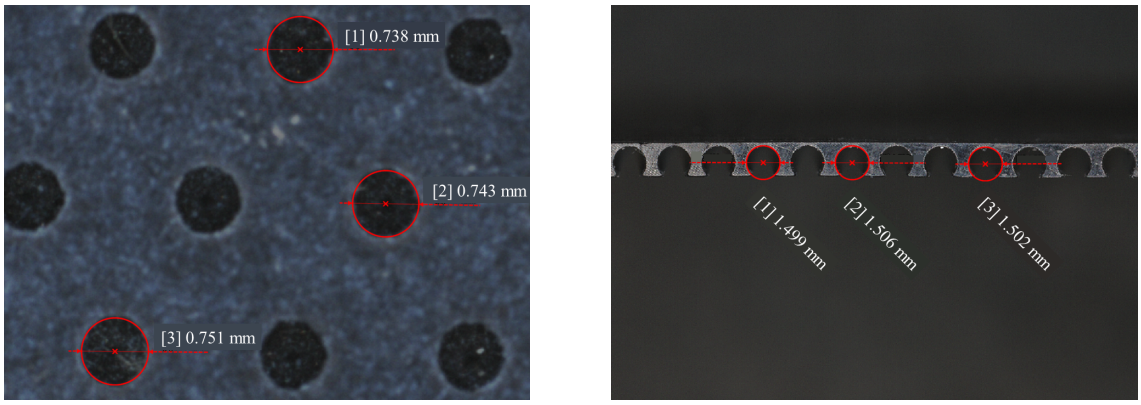

(a) Diameters of the spherical caps (b) Diameters of the cylindrical cavities

Figure 3.17: Cavity dimensions

The diameter of the spheres could not be accurately measured because their fine size meant that it was difficult to cut a section perfectly along the centreline of the spheres. However, making one such cut showed the presence of spherical features as shown in Figure 3.18. Another observation made was that a small number of cavities had excess resin in them that had not been removed during the cleaning of the tiles and had solidified. This was visible when the tile was observed with a strong light source behind it, as seen in Figure 3.19. The consequence of this is that these cavities would not be perfectly spherical in shape.

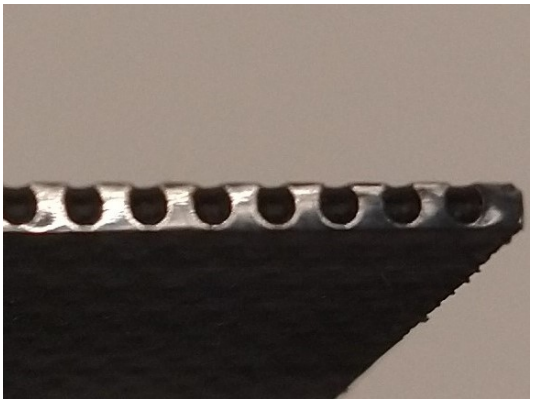

Figure 3.18: Cross-section of a tile with spherical cavities

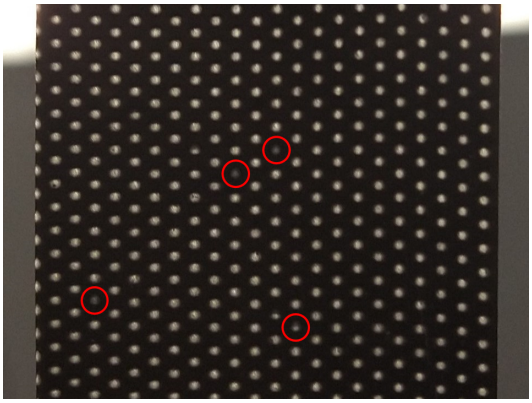

Figure 3.19: A tile with spherical cavities viewed from the bottom

To quantify the degree of superhydrophobicity achievable from the coating, the KSV CAM 200 goniometer in DASML was used. A pipette was used to place 8 μL of distilled water on flat uncoated and coated surfaces, following which the static contact angle of the droplet was measured. Flat surfaces were used as measurements on curved surfaces could not be made with the available setup. Images of droplets on the flat surfaces are shown in Figure 3.20.

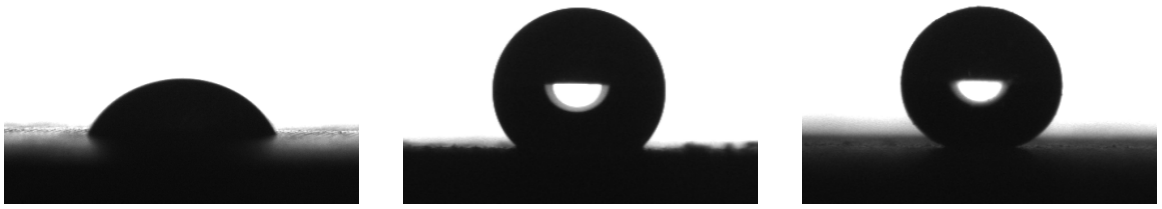

(a) Uncoated 3D-printed surface (b) Coated 3D-printed surface (c) Coated aluminium surface

Figure 3.20: Contact angle measurements on uncoated and coated surfaces

The average contact angle on the uncoated 3D printed surface was measured to be 65.88°. The average contact angle achieved on a coated aluminium surface was 162.14°, indicating that the coating was capable of creating superhydrophobicity. However, on the coated 3D printed surface, an average angle of 143.61° was obtained. While this is highly hydrophobic, it is below the threshold of 150° to be deemed a superhydrophobic surface. It is to be noted that this measurement was carried out approximately 6 months after the surfaces were prepared and tested, which could hint at a deterioration in hydrophobicity over time.

The goniometer also showed the alteration to the shape of the meniscus due to the presence of the superhydrophobic coating. Water in uncoated cylindrical cavities formed a concave meniscus, as seen in Figure 3.21a. In coated cavities, a convex meniscus was observed as displayed in Figure 3.21b, showing that cylindrical droplets were being formed as desired. The convex menisci observed in P-SC (refer Figure 3.16b) indicate that the coating was able to enter the cavities and allow for the creation of spherical water droplets.

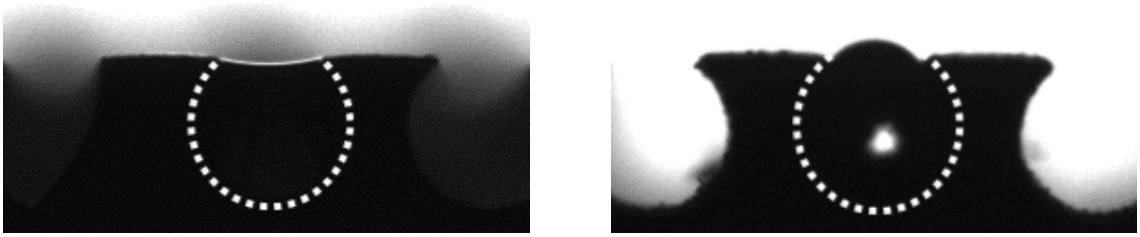

(a) Uncoated (b) Coated

Figure 3.21: Shape of the meniscus in a tile with cylindrical cavities

4

Experimental methodology

This chapter discusses the experimental campaigns used to analyse the performance of LISHySs. Section 4.1 explores the layout of the direct force measurements (DFM) used to quantify the drag performance of the plates. The flow over the plates is characterised using particle image velocimetry (PIV), which is reviewed in Section 4.2. The third campaign, which aims to study the motion of the air-liquid interface, is explained in Section 4.3.

4.1. Direct force measurements

The total force experienced by a body subject to an airflow can be measured via force sensors. This is the method of direct force measurement and it is useful in assessing the overall drag of the body. In order to prioritise the viscous drag contribution, a direct drag measurement device capable of measuring turbulent drag with low uncertainties was developed by van Nesselrooij et al. (2022). This device was to be used to compute the drag of the manufactured surfaces.

4.1.1. Setup

The wind tunnel used for all three experimental campaigns was the M-Tunnel. Located in the LSL at TU Delft, the maximum fan speed of 2900 RPM creates a freestream velocity of 35 m/s in the 400 mm × 400 mm test section when it is in its open circuit configuration, seen in Figure 4.1. The maximum freestream turbulence intensity is roughly 0.7%. The bottom and rear wall of the test section are wooden while the top and front panels are made of transparent acrylic to provide optical access. In order to have a controlled and developed turbulent boundary layer at the test plate, a strip of carborundum lies 600 mm in front of its leading edge. A program written in LabView controls the operation of the wind tunnel, including the option to carry out a controlled velocity sweep.

Force measurements were performed using The Hill, a patented device to measure the friction drag of flat plates, developed and designed by Dimple Aerospace B.V (van Nesselrooij et al., 2022). The measurements have an uncertainty in C_D lower than 0.5% and a confidence of level of 95%. A root mean square error in repeatability of less than 0.2% for drag values greater than 1 N is also ensured.

Figure 4.2 shows some of the key components of The Hill. The test plates are placed in an aluminium and carbon-fibre reinforced polymer connector tray. A ME-systeme KD40S series force sensor with a sampling frequency of 25kHz and range of ± 2N is used to measure loads. An air gap of 0.3 mm ± 0.1 mm along the edges between the core and the connector tray allow the test plate to swing freely. Pressure taps in this gap monitor pressure variations to correct for additional forces. Additional data such as the total pressure, static pressure, WT and ambient temperature, and humidity is collected by sensors in the periscope and the control box. Data from the core is transmitted through a wiring loom to the data acquisition system.

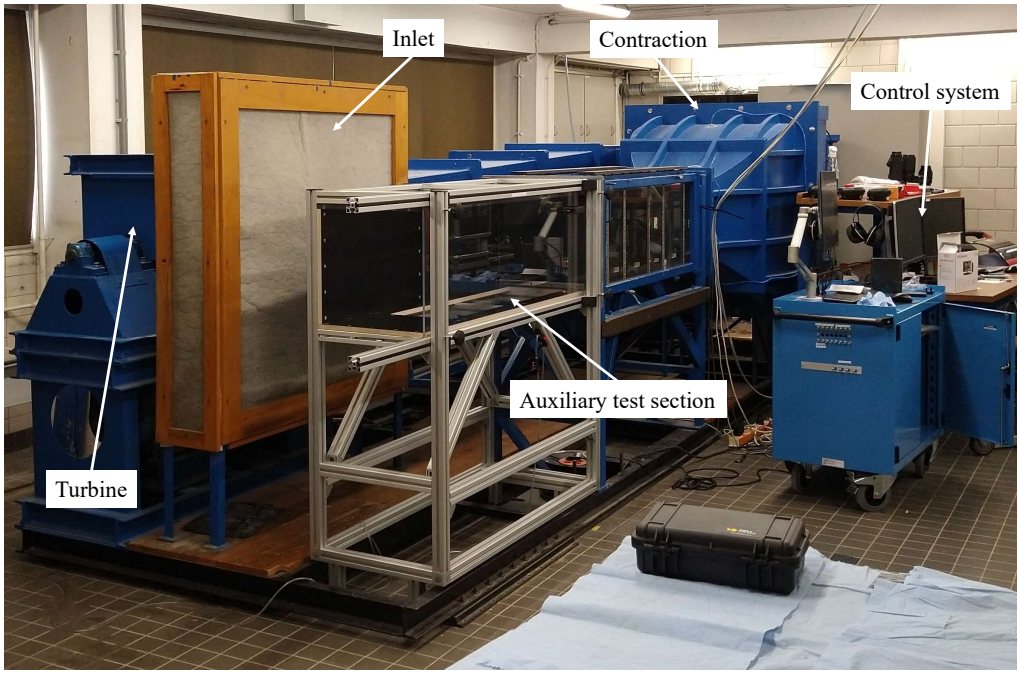

Figure 4.1: Components of the M-Tunnel

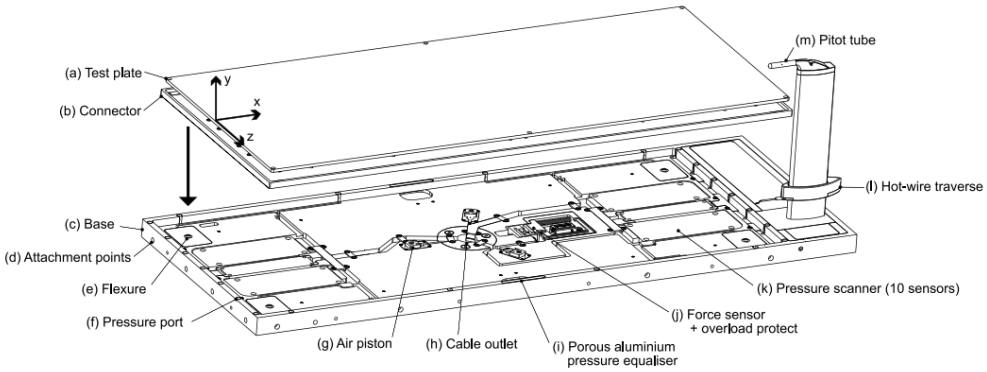

Figure 4.2: High-level architecture of the core element of The Hill (van Nesselrooij et al., 2022)

4.1.2. Measurement plan

Both the designed plates were to be tested in 2 configurations - one without any water droplets in the cavities and one with them. A smooth aluminium plate provided by Dimple Aerospace B.V. was used as the reference plate. In order to check for repeatability and account for outliers, each measurement was repeated thrice. Measurements were carried out in the sequence outlined in Table 4.1. Since the cavities would not dry up completely after water had been infused, it was decided to first perform all of the dry measurements, followed by the wet ones.

Table 4.1: Measurement sequence

Measurement name	Run	Test plate
Warm-up	0	Reference
Round 1	1	Reference
	2	Dry cavities
Round 2	3	Reference
	4	Dry cavities
Round 3	5	Reference
	6	Dry cavities
Round 4	7	Reference
	8	Wet cavities
Round 5	9	Reference
	10	Wet cavities
Round 6	11	Reference
	12	Wet cavities
Final run	13	Reference

Each run began and ended with a null force measurement at $U_\infty = 0$ m/s. Once the tunnel was started, a velocity sweep was carried out from 5 m/s to 25 m/s with 8 equally spaced velocity points between them. One run typically took around 8 minutes, following which a cooldown period of 5 minutes was allowed before performing the next test. The test plates were switched in and out of The Hill during this period. For the wet cavity measurements, spraying of the plates with water and removal of the excess water was carried out during the measurement of the reference plate.

4.1.3. Data processing

The data that is generated by The Hill is accessible as `.csv` files that contain information about the pressure, force and ambient conditions. This is processed in MATLAB to calculate ΔC_D, which is the difference between the drag coefficients of the reference plate and the designed plates. Corrections based on the null force and pressure tap readings are also quantified. Instead of plotting ΔC_D as a function of Re_τ, this is done as a function of Re_1, which is the unit Reynolds number. The reason for doing so is the variation of Re_τ across the length of the test plate, meaning that it cannot be linked to a unique value for a particular freestream velocity. In order to calculate the flow velocity and Re_1 for a particular measurement point, the ambient data and the empirical relation of vapour pressure formulated by Buck (1981) is used.

The drag coefficient is calculated as:

$$C_D = \frac{F - F_p - \Delta F_{\text{null}}}{qS} \tag{4.1}$$

Here, F is the total mesaured force, F_p is the pressure force correction, ΔF_{null} is the null force correction, q is the dynamic pressure and S is the surface area of a test plate.

4.2. Particle image velocimetry

In order to characterise the alteration of turbulent airflow caused by LISHySs, the flow visualisation technique of Particle image velocimetry (PIV) is employed. An important objective in this study is to identify whether a slip velocity exists at the wall.

PIV is non-intrusive and quantitative, providing data about the instantaneous state and the mean properties of the flow. The displacement of small tracer particles carried by the flow is used as a measure of the local velocity. A laser sheet, which is created using a powerful light source and a combination of optical lenses, is used to illuminate the particles in the region of interest. The motion of the particles is captured by a high-speed camera and a precise timing system. A few hundred images are captured in pairs and segmented into

blocks known as interrogation windows. Cross-correlation is then carried out between image pairs in order to calculate the mean displacement and, in turn, the velocity of the flow in the interrogation window. Putting the computed velocities from all the windows together results in instantaneous flow fields, from which parameters such as the mean velocity profile and the Reynolds stresses can be calculated.

4.2.1. Setup

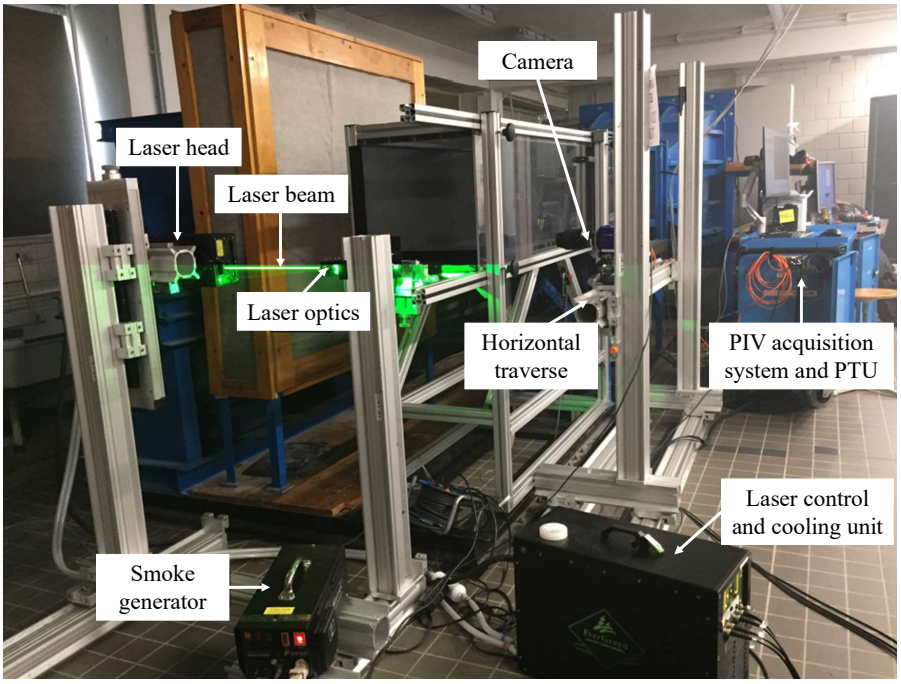

Figure 4.3: Setup used for PIV measurements, adapted from Jawahar (2022)

Figure 4.3 shows the setup installed to carry out PIV measurements. A SAFEX Fog 2010+ smoke generator was used to generate tracer particles approximately 1μm in diameter. This was placed near the inlet of the wind tunnel and controlled manually. The particles were illuminated using a Quantel EverGreen laser, which is a 200mJ double-pulsed ND:YAG laser that emits a light beam of wavelength 532 nm. Since the plane of interest is the streamwise wall-normal plane, a series of lenses and a mirror, as shown in Figure 4.4, was used to convert the beam into a laser sheet of thickness approximately equal to 1.5 mm. A knife-edge was used to trim the laser height of the laser sheet, thus allowing for the reflections off the surface to be reduced. A view of the laser sheet formed in the test section is shown in Figure 4.5.

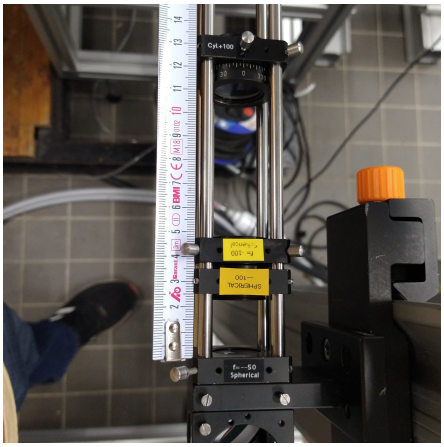

Figure 4.4: Arrangement of optics

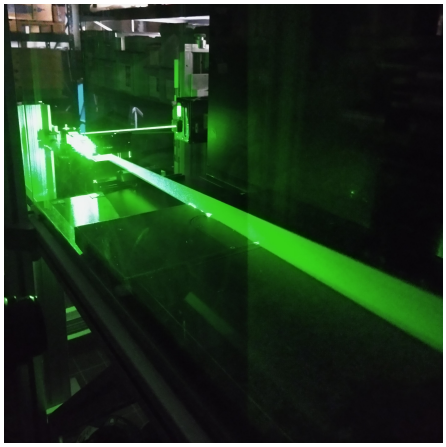

Figure 4.5: Resulting laser sheet

In order to capture images to track the motion of the tracer particles, an sCMOS CLHS camera, manufactured by LaVision GmbH, was used. This has a pixel size of 6.5 μm and a sensor size of 2560 px × 2160 px. A 105mm AF Micro Nikkor lens with an f-stop (f#) of 8 was fitted to it. Attaching the camera to a three-axis mount on a horizontal traverse allowed for the identification of a suitable streamwise location to record images. The averaging effect caused by the incidence angle of light was minimised by placing the camera at the same vertical level as the top surface of the test plate and tilting it slightly upward to record the the entire boundary layer. Graph paper with millimeter markings was used to calibrate the images. To synchronise the laser pulses with image capturing, a LaVision Programmable Timing Unit (PTU) was used. DaVis 10.2.0 was the software used to control the operation of the lighting and imaging systems. This was also used to store and process the images.

Since the same test plates were to be used for the PIV campaign and The Hill could not be used to used due to possible damage from seeding and laser light, a mount called The PHill (PIV Hill), designed by Lai (2021), was utilised. The PHill's holder resembles The Hill's connector tray and ensures that the flow conditions are similar to that of the drag measurements. However, the depth of the PHill is more than 5mm so aluminium spacers were needed underneath the test plates to keep them level with the floor of the test section.

4.2.2. Measurement plan

The variables of interest from the PIV measurements were the mean velocity profiles, velocity fluctuations and Reynolds stresses. Since the plates were designed for operation at $U_\infty \approx 15$ m/s, three freestream velocities were chosen for investigation - 10 m/s, 15 m/s and 20 m/s - to analyse the flow over the surface below, at and above the design velocity. Measurements at two intermediate velocities (12.5 m/s and 17.5 m/s) were also performed. Both plates were to be tested in their dry and wet configurations. In order to decrease the effects of water evaporating or being carried away with the flow over time, the plates were resprayed before every run. The streamwise location being recorded was kept as close to the trailing edge as possible in order to obtain a thick and developed boundary layer. However, it was required to be moved some distance upstream as the tile near the leading edge of P-SC had become slightly inclined. The position of the FOV is shown in Figure 4.6. The parameters that were used during the campaign have been listed in Table 4.2.

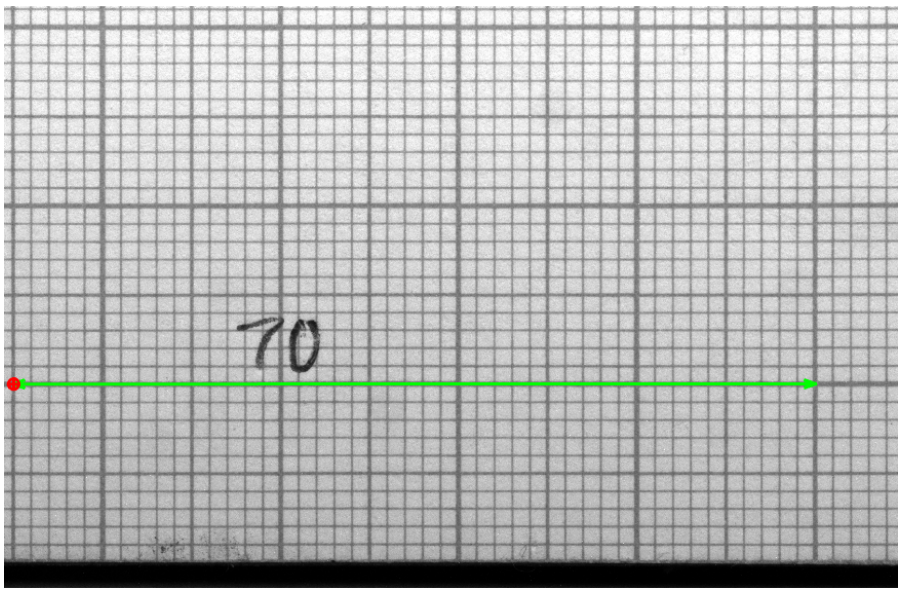

Figure 4.6: Calibration for PIV processing, indicating FOV and its position from the leading edge (marked in black ink) with the direction of flow from right to left

Table 4.2: Parameters defined for the PIV experiments

Parameter	Dimensions	Value
FOV (w x h)	mm x mm	50.41 x 32.61
f#	-	8
U_∞	m/s	10, 12.5, 15
Δt	μs	40, 34, 27
Trigger rate	Hz	30
Exposure time	μs	10
Resolution	px/mm	50.78
Particle displacement	px/image pair	20
Number of image pairs	-	600
Laser intensity	%	70

4.2.3. Data processing

Processing PIV data is a 3 step procedure. Firstly, the raw images need to be made made more suitable for further analysis using a pre-processing routine. Next, correlation is carried out to obtain velocity vector fields. Finally, this is post-processed to compute TBL properties.

Pre-processing

Due to the manner in which the laser sheet is incident on the test plates, reflections are obtained and captured by the camera. The presence of the coating and water droplets on the top surface further worsens reflections in the image. In order to decrease them, a subtraction operation is carried out in DaVis. This uses a Butterworth high-pass filter with a filter length of seven images. While reflections cannot be completely eliminated, their magnitude can be considerably decreased, as seen in the difference between the images in Figures 4.7a and 4.7b.

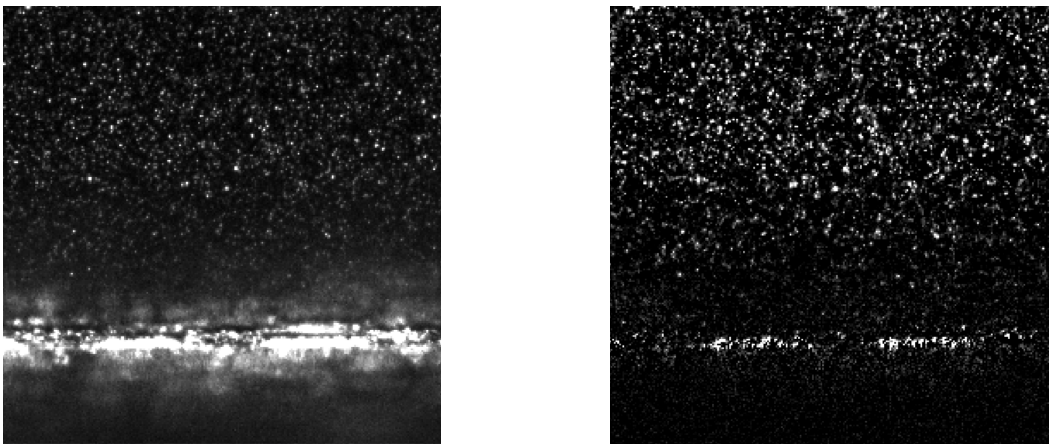

(a) Raw image

(b) After image subtraction

Figure 4.7: Zoomed-in images demonstrating the effect of the Butterworth filter

Processing

The conversion of the filtered image files into vector field data is a four step process (Scarano, 2013) as outlined below:

1. **Image windowing**: The captured image is partitioned into interrogation windows, each with several tracer particles. The local velocity is evaluated for each of these windows.

2. **Cross-correlation**: The cross-correlation function is applied to corresponding windows of an image pair, which produces a discrete cross-correlation map. The peak position within this map relative to the origin gives the average particle displacement.
3. **Correlated peak sub-pixel interpolation**: The position of the highest peak is naturally found at the closest integer pixel shift. For a more accurate peak position estimate, an interpolation near the peak is performed.
4. **Time division and scaling**: The velocity of the flow in the interrogation window is obtained by dividing the pixel shift by the time separation between laser pulses, multiplying by the size of the pixel and dividing by the magnification factor.

The settings defined for vector calculations are listed in Table 4.3. These were determined on the basis of a benchmarking test carried out by Hartog (2021) and trial runs with similar settings and variations to the window size and number of passes.

Table 4.3: Vector calculation settings for cross-correlation

Parameter	Value
Maximum expected particle displacement	22 px
Spatial resolution of vectors	16 px
Initial pass	
Window size	96 × 96
Window shape	Elliptical 2:1
Overlap	75%
Number of passes	1
Final pass	
Window size	16 × 16
Window shape	Elliptical 2:1
Overlap	75%
Number of passes	2

Post-processing

In order to plot the mean velocity profiles and obtain characteristic BL properties, vector field data obtained after cross-correlation was exported from DaVis in the form of `.dat` files. The properties that are included in these files are the velocity components u and v, the Reynolds stress $-\overline{u'v'}$ and the standard deviation of the velocities σ_u and σ_v.This was subsequently processed in MATLAB using codes created by Hartog (2021). The steps involved in the calculation of the profiles were as follows:

1. The exported `.dat` files from DaVis were imported into MATLAB and stored as matrices.
2. The wall location was estimated over the selected range within the FOV by determining the point of minimum mean velocity at every streamwise coordinate. For the wall profile, a double sliding median was applied and fitting was carried out using a third-degree polynomial.
3. The horizontal tilt in the wall was corrected by projecting the boundary layer profile at every x coordinate onto a new vector with the y location of the wall estimate being the first point. This correction was used to trim data below the estimated wall from the stored matrices.
4. Spatial averaging was performed over specific streamwise locations within the FOV. This was necessary in order to avoid regions on the test plate with bright reflections.
5. Integral boundary layer properties (δ, δ^* and θ) were calculated using the relations listed in Section 2.1.
6. The friction velocity (u_τ) was calculated by performing BL fitting using the composite method (Rodríguez-López et al., 2015). This method was chosen over Clauser's and Spalding's methods as it fit a larger portion of the velocity profile and was less susceptible to bias in the near-wall region. The skin friction coefficient was subsequently calculated using Equation (2.13).

4.3. Liquid motion visualisation

A fundamental part of the drag reduction mechanism envisioned for LISHyS is the steady rolling motion of the liquid volumes in the spherical or cylindrical cavities. An experimental campaign was thus formulated to physically observe this motion.

4.3.1. Setup

Since the objective of this test is to study the motion of the liquid within the cavities, the ideal test surfaces would be transparent in nature. Additionally, there was no need to create an entire test plate as having a surface with a few distinct liquid interfaces would suffice. While an attempt was made to create and study small transparent LISHySs, they could not be made transparent to the degree of being able to observe motion inside the cavities. Additionally, the coating itself creates a hazy white texture, further hindering observations. Details of these have been discussed in Appendix C.

Since the main feature of interest was the spherical or cylindrical droplets and these were quite small in the test plates due to the need to increase the liquid fraction, it was decided to increase their size for this test. This was done with the constraint of keeping the protrusion height of the features within 100 μm. Miniature tiles of dimensions 30 mm × 29.5 mm × 5 mm, one with spherical cavities and one with cylindrical cavities, were thus created with a cavity depth twice as large as the cavities in the test plates used for the drag measurement and PIV campaigns. They were produced using the same technique as the test plates with the assembly step not being necessary.

The Knoll was designed to pick up the existing boundary layer present on the floor of the wind tunnel and pass it over the designed LISHySs. As an attempt was made to view liquid motion through the side (streamwise wall-normal plane), one side of the space that holds the mini tile was left open. Its dimensions have been provided in Figure 4.8a. A zig-zag strip (Hansjörg Streifeneder, 0.79 mm thick) was placed 700 mm ahead of the leading edge of the tile to trip the boundary layer. This was considered to be the starting point of the turbulent boundary layer. A metal halide lamp was used to illuminate the liquid-air interface. While chalk dust and ink were initially considered as tracer particles, it was observed during the tests that specks of dust provided an accurate representation of motion at the interface. A view of this setup can be seen in Figure 4.8b.

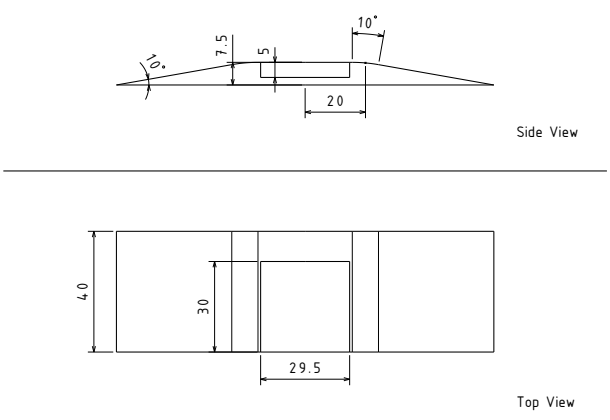

(a) Dimensions of The Knoll

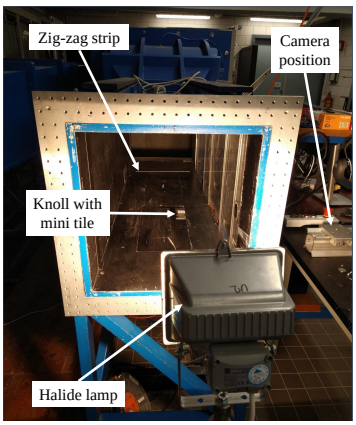

(b) Setup

Figure 4.8: Setup for liquid motion visualisation

In order to capture the motion of the liquid, an imaging system that is able to view the liquid interface up-close was necessary. A Micro Alignment Telescope (MAT) manufactured by Taylor Hobson was used to capture images with a high degree of magnification. However, this had no feature to record videos. Additionally, the MAT's high exposure time meant that the motion of particles near the interface appeared to be discontinuous. Thus, a Canon 750D Digital Single-Lens Reflex (DSLR) camera with a resolution of 6240 px × 4160 px was also used. Videos were captured through a Canon EF-S 18-135 mm USM wide angle lens. Photos were also captured with a Canon EF-S 55-250 mm Telephoto lens to supplement the images captured with the MAT.

4.3.2. Measurement plan

The two mini tiles were to be fitted one after the other into the Knoll. Three velocities were chosen for this study - 5 m/s, 10 m/s and 15 m/s. The behaviour of the interface at speeds higher than these was not investigated due to the difficulty in observing particle motion. Static images were taken with the MAT at these velocities. This procedure was then repeated using the DSLR camera. Images were captured first, followed by the recording of videos for both tiles.

5

Results and discussion

This chapter presents the results of the experimental campaigns performed on the manufactured liquid-infused superhydrophobic surfaces and then discusses the observations. The results of the experimental campaigns are presented in the first three sections - DFM in Section 5.1, PIV in Section 5.2 and LMV in Section 5.3. This is followed by a discussion on the potential sources of drag based on the results of the three campaigns in Section 5.4.

5.1. Direct force measurements

The results of the direct force measurements on P-SC have been presented in Figure 5.1. Measurements were not made for P-CC due to the risk of damage to the measurement device. This is because filling the plate, which could be done only after it had been placed in the device, carried the risk of sensitive electronics coming into contact with water. Additionally, if the larger droplets held in this plate were removed from the cavities due to the shear force exerted by the freestream flow, there was a high risk of water entering the space between the test plate and the device, and thus harming it.

In order to verify that the plate was approximately equally filled initially and lost a similar amount of water during every test run, the plate was weighed before and after the runs. The dry weight of the test plate was measured to be 1606.5 g. Section 5.1 shows the weights of the plate for the runs. After making 3 runs, it was observed that the initial weight of the plate in Run 1 was significantly lower than during the following two, which is why a fourth run was performed.

Table 5.1: Weight of P-SC before and after drag measurement runs

Run	**Weight of test plate (g)**		**Weight of water**
number	**Before**	**After**	**lost (g)**
1	1688.7	1671.1	17.6
2	1707.7	1691.5	16.2
3	1711.3	1694.2	17.1
4	1711.4	1695.7	15.7

In the figures, the "Dry" lines represent the results of the cavity-laden plate without any water and the "Wet" lines represent those after liquid infusion. In Figure 5.1a, the solid lines in the figure represent the values of drag of the cavity-laden test plate while the dotted lines represent those for the smooth reference plate. Two observations that can be made from this figure are:

1. The wet plate produces higher drag than the dry plate at all freestream velocities.

2. The dry plate produces higher drag than the reference plate at all freestream velocities.

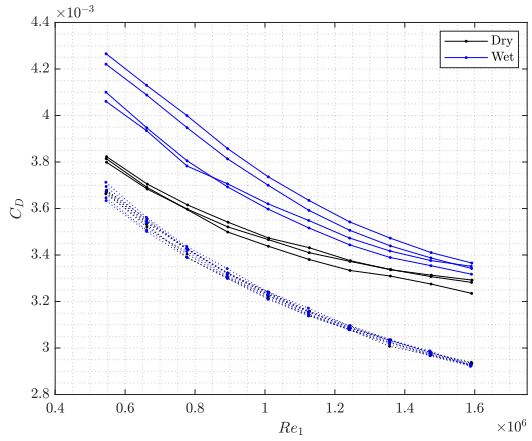

(a) Drag coefficient

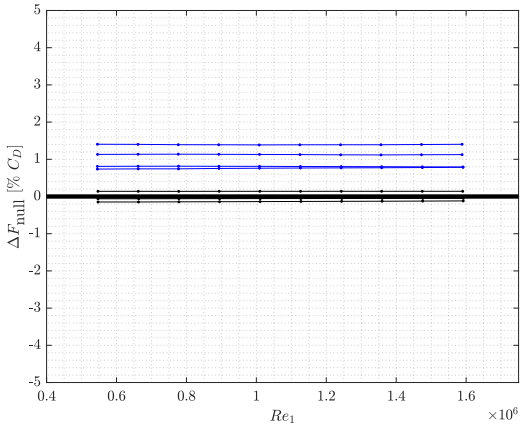

(b) Null force correction

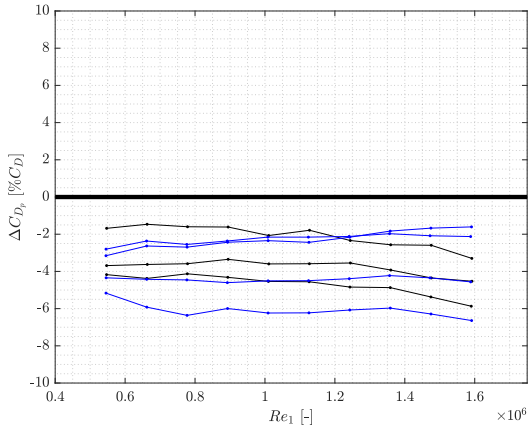

(c) Pressure drag correction

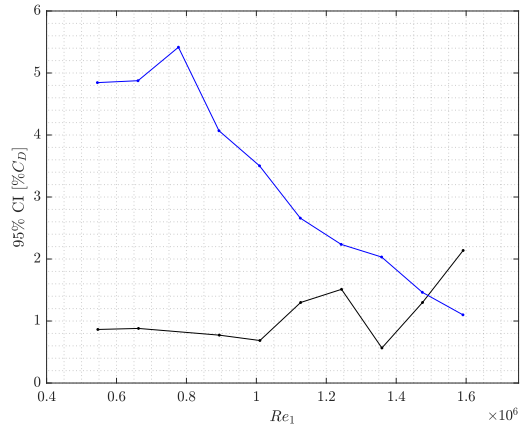

(d) Measurement uncertainty expressed as RMSE

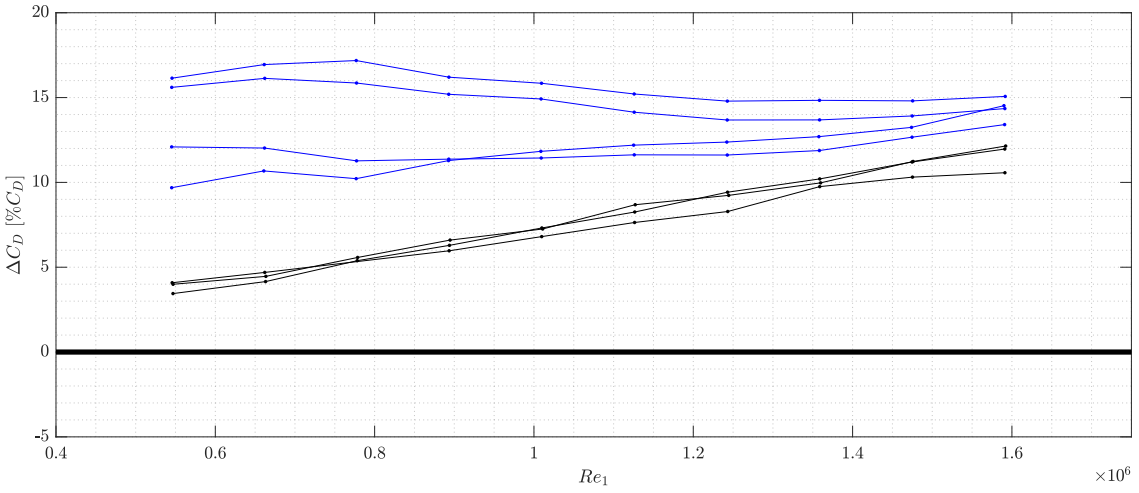

(e) Difference in drag coefficient, measured with respect to the reference plate

Figure 5.1: Direct force measurement results for P-SC

Figure 5.1b shows the null force correction necessary. This adjusts for changes to the null force value brought about by the force sensor's sensitivity to temperature and creep. For the dry plate, this value is observed to be within $\pm 0.2\% C_D$. The wet plate shows higher values between 0.7 and 1.4 $\% C_D$. In the context of the values of the drag coefficients observed, this is deemed acceptable.

Figure 5.1c depicts the correction needed to account for pressure drag. The values are observed to be within 7% C_D for both the configurations of the plate, which is acceptable given the C_D values obtained.

Figure 5.1d shows the uncertainty in the root-mean-square error in the measured values. In general, the wet plate exhibits higher uncertainty than the dry one. The variation in the amount of water infused into the plate prior to the runs could be one of the reasons for this high uncertainty.

The differences between the drag coefficients, corrected for pressure and null force shift, obtained for the wet and dry plates in the selected velocity range are depicted in Figure 5.1e. The wet plate is seen to have higher ΔC_D than the dry plate for all values of Re_1. The difference between the two is as large as 10% at low Re_1, and decreases with increasing Re_1. The wet and dry lines appearing to be on a converging path could be the result of water being drained from the cavities, which is accelerated at higher freestream velocities.

An outlier point was observed for one of the measurements made using the dry plate at $Re_1 = 0.78 \times 10^6$. This corresponded to $C_D = 4.35 \times 10^{-3}$. Potential causes for this include resonance in the measuring system or a brief disturbance outside the wind tunnel that was picked up by the force sensor.

Apart from these, the following visual observations were made during the tests:

- Some droplets of water that did not enter cavities and were not blown away using the air blow gun stayed on the top surface refused to be blown away even at the highest velocity of 25 m/s.
- One of the tiles had a large wet patch (approximately half of its area), that is the surface did not exhibit superhydrophobicity here. After spraying, a liquid film was seen over this region which was present after the test run as well.
- Water appeared to adhere to the strips of acrylic kit in between tiles instead of being repelled by them.

5.2. Particle image velocimetry

For the PIV experiments, it was possible to test both of the manufactured plates. Examples of the raw images captured are shown in Figure 5.2. However, there was trouble with obtaining clear near-wall data due to reflections even after filtering, as seen in Figure 5.3. These reflections were aggravated by 2 factors - the texture of the coating and the presence of water in the cavities. They were observed to be worse in the case of P-CC. Additionally, in the case of this plate, particles were not observed in a sizeable region close to the wall ($y^+ \leq 20$) across the FOV. This negatively impacts the post-processed results for this design.

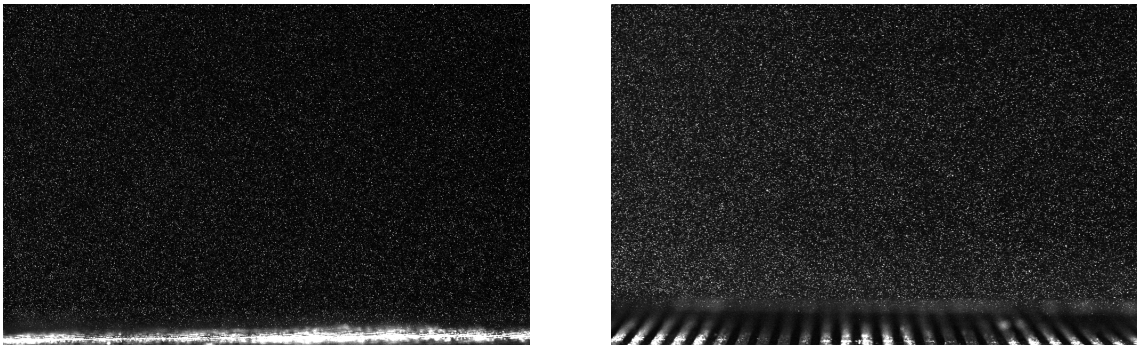

(a) P-SC (b) P-CC

Figure 5.2: Raw images captured during the PIV campaign

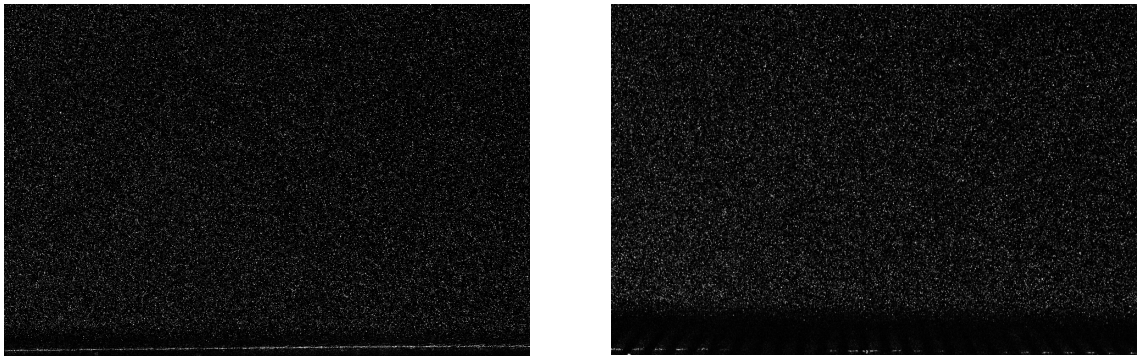

(a) P-SC (b) P-CC

Figure 5.3: Raw images after application of the Butterworth filter

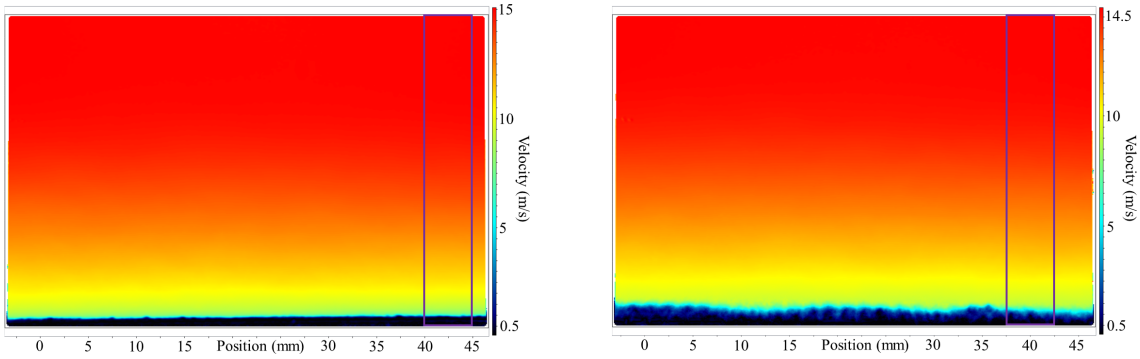

(a) P-SC (b) P-CC

Figure 5.4: Mean velocity fields after cross-correlation, exported from DaVis. The portion of the FOV over which spatial averaging of the wall-normal profiles were performed is enclosed in purple.

5.2.1. Uncertainty quantification

Determining the uncertainty in a measurement is necessary to assess the quality of data obtained. For the PIV experiments, uncertainty is calculated as the standard error and is determined for the instantaneous velocity (Equation (5.1)), the mean velocity (Equation (5.2)), the velocity fluctuation (Equation (5.3)) and the Reynolds stress components (Equation (5.4)). These equations have been derived from the works of Benedict and Gould (1996) and Raffel et al. (1998).

$$\epsilon_u = \epsilon_{\text{corr}} \frac{\Delta x_{\text{px}}}{\Delta t} \tag{5.1}$$

$$\epsilon_{\overline{u}} = \frac{\sigma_u}{\sqrt{N}} \tag{5.2}$$

$$\epsilon_{\sigma_u} = \frac{\sigma_u}{\sqrt{2(N-1)}} \tag{5.3}$$

$$\epsilon_{R_{xy}} = \sigma_u \sigma_v \sqrt{\frac{1+\rho_{uv}^2}{N-1}} \tag{5.4}$$

Here, ϵ_{corr} is the pixel correlation error, equal to 0.1. N is the number of sample points, which in this case is equal to the number of image pairs in a measurement (600). ρ_{uv} is the cross-correlation coefficient, calculated as:

$$\rho_{uv} = \frac{\overline{u'v'}}{\sigma_u \sigma_v}$$

Table 5.2 displays the uncertainty estimations for the parameters of interest. These are defined for the spatially averaged boundary layer profiles, calculated by averaging these quantities in the streamwise direction within a selected region of the entire FOV. The uncertainty of spatially averaged profiles is decreased proportionally to the inverse of the square root of the number of uncorrelated data points (Sciacchitano and Wieneke, 2016). As the data was processed with a 75% overlap of the interrogation windows, every fourth data point in the streamwise direction is uncorrelated.

It is observed that the uncertainties in the quantities of interest are low, being below 1%. However, it is seen that the uncertainties in the measurements made on P-CC are notably higher than those for P-SC and the reference plate.

Table 5.2: Mean uncertainties of the spatially averaged wall-normal profiles. Values are represented as a percentage of the corresponding local value.

Test plate	U_∞	ϵ_u (m/s)	$\epsilon_{\overline{u}}$ (%)	ϵ_{σ_u} (%)	ϵ_{σ_v} (%)	$\epsilon_{R_{xy}}$ (%)
Reference	10	0.049	0.15	0.10	0.07	0.08
	15	0.073	0.21	0.15	0.09	0.18
	20	0.099	0.27	0.19	0.12	0.32
P-SC: Dry	10	0.049	0.15	0.11	0.07	0.08
	15	0.073	0.22	0.16	0.10	0.19
	20	0.099	0.29	0.21	0.13	0.36
P-SC: Wet	10	0.049	0.15	0.11	0.07	0.08
	15	0.073	0.20	0.14	0.09	0.18
	20	0.099	0.26	0.19	0.12	0.33
P-CC: Dry	10	0.049	0.22	0.16	0.10	0.24
	15	0.073	0.31	0.22	0.14	0.49
	20	0.099	0.37	0.26	0.17	0.79
P-CC: Wet	10	0.049	0.23	0.16	0.11	0.30
	15	0.073	0.30	0.22	0.14	0.54
	20	0.099	0.38	0.27	0.18	0.86

5.2.2. Velocity profiles and turbulent statistics

Figure 5.5 displays the dimensional boundary layer velocity profiles of the flow over the test plates at a freestream velocity of 15 m/s. The profiles of the wet and dry configurations of the test plates are compared against those of the reference plate.

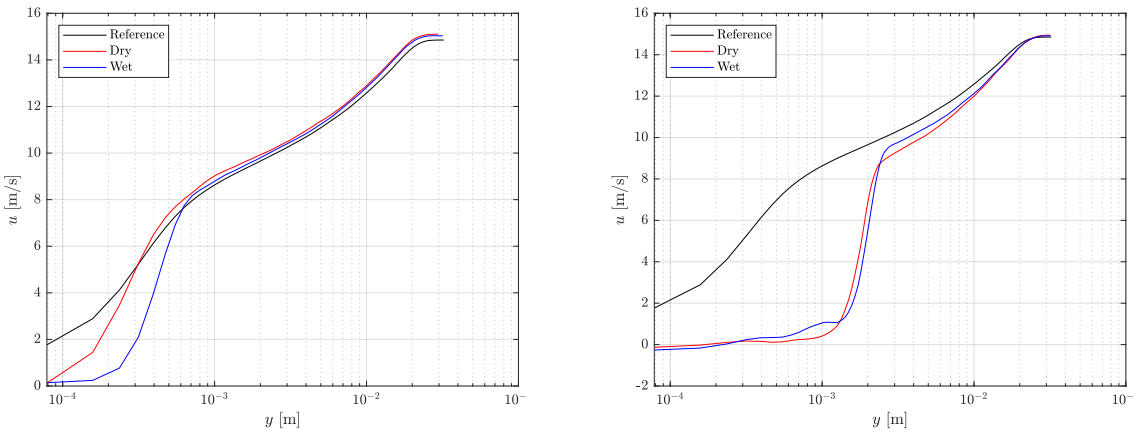

(a) P-SC

(b) P-CC

Figure 5.5: Dimensional velocity profiles at $U_\infty = 15$ m/s

From Figure 5.5b, it is evident that a significant portion of the velocity profile for P-CC is inaccurate due to the lack of information close to the wall. Thus, meaningful non-dimensional profiles could not be extracted from the PIV data for the flow over this surface and have been excluded from this section. For the data associated with P-CC, values corresponding to $y^+ < 30$ have been trimmed as the trends in this region appeared to be erratic.

Figure 5.6a shows the mean streamwise velocity profile for P-SC. Due to the lack of near-wall data, a non-zero slip velocity at the wall cannot be confirmed. Beyond $y^+ = 30$, the profiles collapse neatly onto the one for the reference plate. For $y+ > 70$, the mean velocity over P-SC in its wet configuration is observed to be higher than in the other cases. An upward shift in the logarithmic profile with respect to a smooth surface is typically indicative of a decrease in local skin friction.

Figures 5.6b and 5.6c depict the fluctuations of streamwise and wall-normal velocity. The close to the wall are quite misleading with a decrease in the properties expected (Schlatter and Örlü, 2010), possibly due to aforementioned reasons. The profiles for points higher in the overlap layer ($y^+ > 70$) seem to converge with the wet configuration showing the lowest fluctuations in the outer region.

Figure 5.6d shows the Reynolds stress profile. The Reynolds stress for both configurations of P-SC is observed to be notably higher than that for the reference plate for $y^+ < 230$, indicating higher turbulent energy. The peak is also observed to be just outside the buffer layer in the case of P-SC while it is higher in the boundary layer for the reference plate. In the overlap layer beyond this, excluding $400 < y^+ < 500$, the Reynolds stress for the P-SC is lower with the wet configuration having marginally lower turbulent energy than the dry configuration.

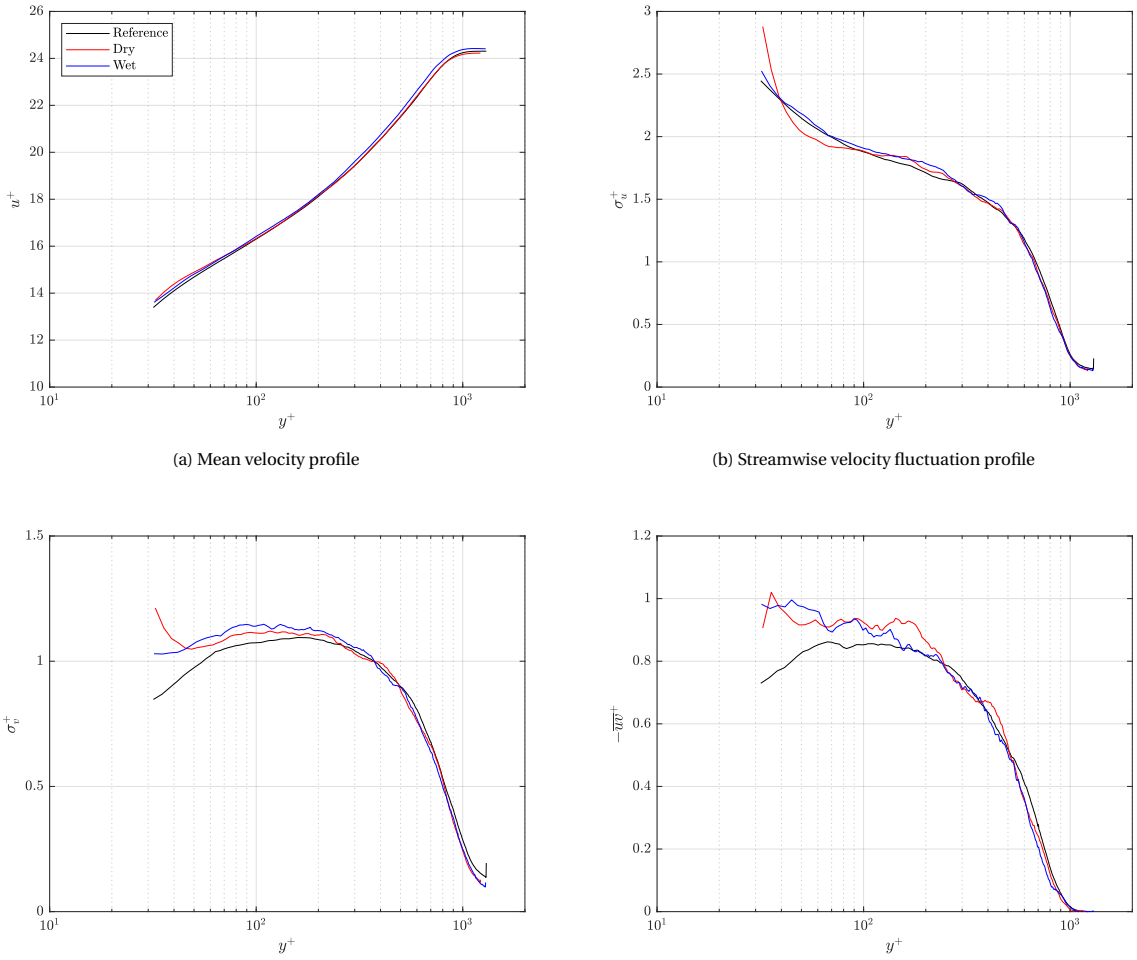

(a) Mean velocity profile

(b) Streamwise velocity fluctuation profile

(c) Wall-normal velocity fluctuation profile

(d) Reynold's stress profile

Figure 5.6: Boundary layer profiles for P-SC at $U_\infty = 15$ m/s

5.2.3. Integral boundary layer properties

Figure 5.7 shows the variation in the boundary layer properties of the flow over P-SC with freestream velocity. The general trend agrees with theory, showing a decrease in these properties with increasing freestream velocity.

The thickness of the boundary layer is very similar, as seen in Figure 5.7a. There is little difference in these values until 15 m/s, after which the wet plate shows smaller δ. The displacement thickness of the flow over the wet surface, plotted in Figure 5.7b, is seen to be higher than that over the dry surface at all tested velocities. With regards to the momentum thickness, Figure 5.7c shows that it decreases more rapidly for the wet plate than for the dry plate with increasing freestream velocity.

From Figure 5.7d, excluding what appears to be an outlier at 12.5 m/s, the skin friction coefficient for the wet configuration is observed to be lower than that of the dry configuration. This is calculated from the frictional velocity as per Equation (2.13). However, the closeness of the obtained values lies within the bounds of uncertainty, meaning that skin friction reduction over the wet LISHyS cannot be ascertained.

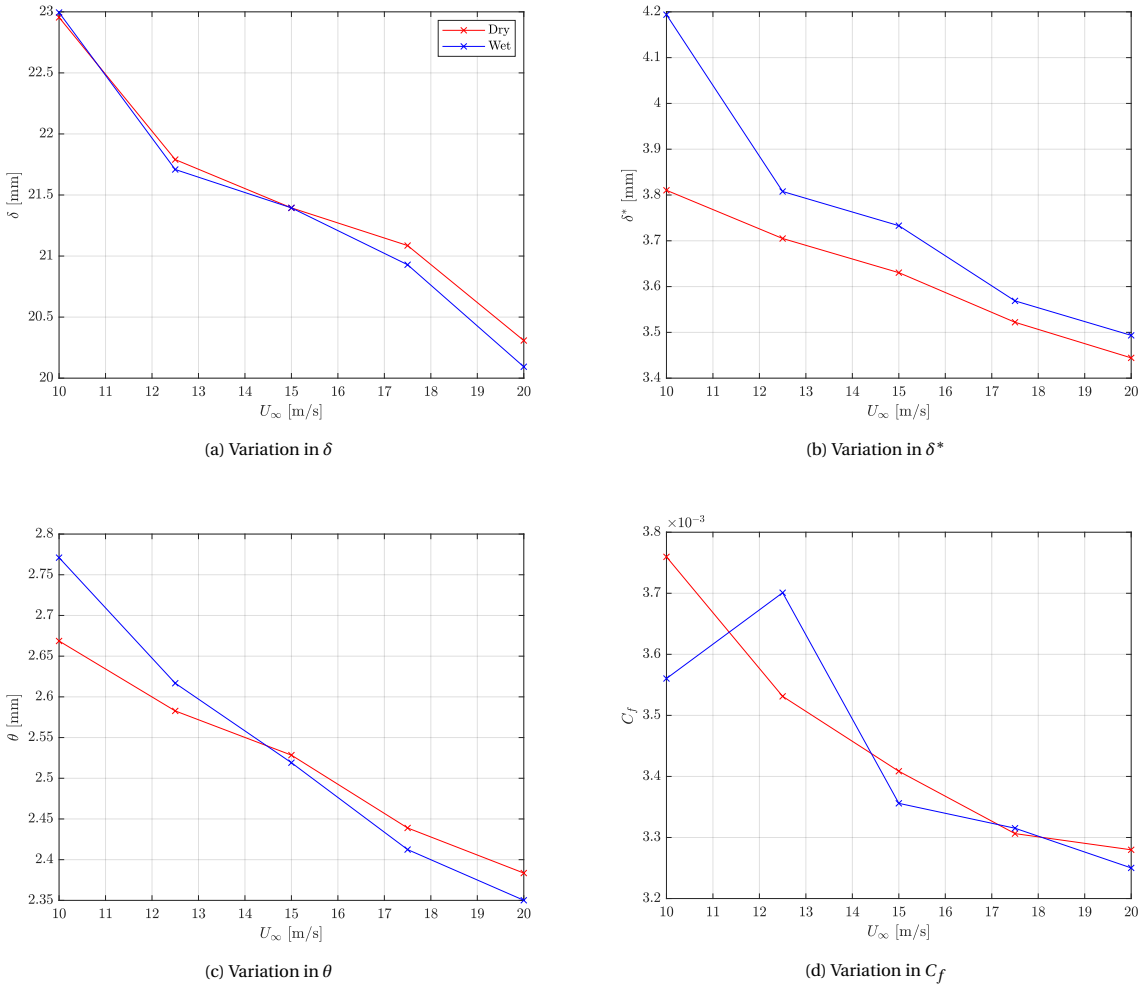

(a) Variation in δ

(b) Variation in δ^*

(c) Variation in θ

(d) Variation in C_f

Figure 5.7: Boundary layer properties for P-SC

5.3. Liquid motion visualisation

Figure 5.8 shows images of the liquid-air interface of the mini tile with spherical cavities at different freestream velocities, captured using the Micro Alignment Telescope (MAT). The perpendicular lines visible in these images are the cross-hairs of the MAT, and are not of relevance for this experiment. One of the immediate observations made during the test was that the liquid volumes in the case of this mini tile were far too small

to discern motion of the interface. Nonetheless, in the images captured, 3 regions of interest were identified, which have been highlighted using red, blue and green boxes.

The red box focuses on a liquid interface in the foreground. This was visible at 0 m/s and 5 m/s, (noticeable through the liquid being reflective) in these locations. At higher velocities, this area was no longer reflective, showing a decrease in the level of liquid. The blue box also indicates similar behaviour with a liquid surface being visible at 5 m/s, less so at 10 m/s and disappearing at 15 m/s.

The green box shows a spherical droplet in the background. As the freestream velocity was increased, this was observed to "sink" into the cavity. While there was almost no difference in its position at 0 m/s and 5 m/s, it was lower at 10 m/s and almost disappeared at 15 m/s. The difference in the heights of the interface between the three boxes also showed that the cavities were not evenly filled, with some being overfilled and others being underfilled.

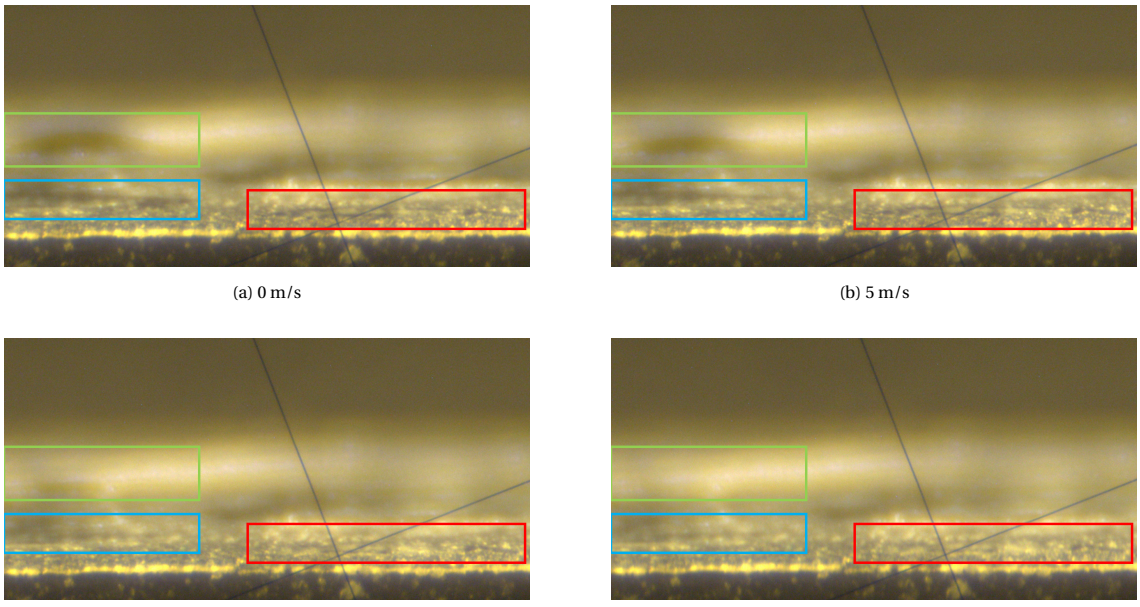

(a) 0 m/s

(b) 5 m/s

(c) 10 m/s

(d) 15 m/s

Figure 5.8: Images of the mini tile with spherical cavities at different freestream velocities, as observed through the MAT

The video captured using the DSLR camera provided further insights into the behaviour of the liquid-air interface at different freestream velocities. Figure 5.9 shows a still image from the video taken of the mini tile with cylindrical cavities. As static images from the clip do not clearly indicate the direction of motion, drawings have been made of the observed motion. These are presented in Figure 5.10.

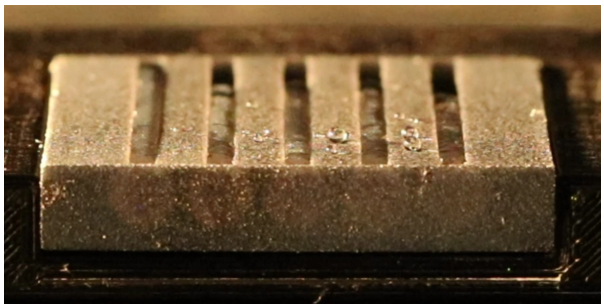

Figure 5.9: An image from the video recorded of flow over the mini tile with cylindrical cavities. The direction of the freestream is from the right to the left.

(a) 5 m/s (b) 10 m/s (c) 15 m/s

Figure 5.10: Drawings indicating the direction of liquid motion observed

At U_∞ = 5 m/s, a steady rolling motion of the cylindrical droplets was observed in all the cavities. The speed of rotation was estimated to be between 1.5 and 2 mm/s.

Once the freestream velocity was set to 10 m/s, the motion of the droplets was seen to be faster in the streamwise direction. Their speed of rotation was gauged to be around 4 mm/s. At this speed, some amount of spanwise flow was also observed.

Increasing the freestream velocity to 15 m/s further accelerated the speed of rotation of the droplets. This was accompanied by a significant amount of spanwise motion that was chaotic in nature, moving in a random pattern across the exposed portion of the droplet.

Similar to the observation made during the drag measurement campaign, droplets on the surface of the mini-tile were observed to stay in place. Directly behind the surface droplet, the steady rolling motion of the infused droplet was observed to be locally disturbed, especially at higher velocities.

5.4. Potential sources of drag

The previous sections provide evidence that the manufactured surfaces were incapable of producing drag reduction at and around the design velocity. This was observed in the cases of both the dry and wet configurations of the test plates. For the dry plates, the following reasons have been identified as contributors to increased drag forces:

- **Spaces between tiles**

  Although acrylic kit was used to seal the space between the tiles of the test plates, it was observed that this was not able to flow into spaces thinner than approximately 1 mm. This created narrow gaps between some tiles. When these gaps are oriented in the spanwise direction, the exposed faces of the tiles add to pressure drag.

- **Changes in the flatness of the plate**

  The 3D printed tiles were bonded to the acrylic base using tape and were pressed down by placing similarly shaped solid aluminium plates onto it to produce a flat surface. However, over time, the adhesive force between the tiles and the base weakened unevenly, causing portions of some tiles to lift up. This was noticed more severely in the tiles with spherical cavities. There are thus 2 components that contribute to drag, one being the part of the front of the tile that is exposed to the flow and the other being the "waviness" in the plate due to the tiles having an inclination in the streamwise direction. While ordered wavy surfaces have the potential to reduce skin friction (Balasubramanian and Orszag, 1980), the random waviness created by the tiles is expected to be detrimental to the drag reduction capabilities of the plates due to the increased pressure drag.

Another reason for the higher drag observed in the dry configuration is the presence of open cavities on the surface. This, along with the other factors contributing to the increase in drag for the wet configuration of the test plates, is described below:

- **Loss of water from the cavities**

  The loss of water from the cavities directly leads to the failure of the hypothesised working mechanism because of the absence of the fluid-fluid interface. This is caused by 2 factors - natural evaporation and shear-driven drainage. As the freestream velocity is increased, the rate of evaporation is increased due to the drop in humidity close to the air-water interface. Evaporation is of higher concern in P-SC due to the low volume of individual droplets. The higher shear force at the interface also removes water from

the cavities, and increases with increasing freestream velocity. In the case of P-CC, it was noticed that water expelled from one cavity could "pull" water out from other cavities due to the larger contact area and the stronger cohesive force between water droplets than the adhesive force between water and the superhydrophobic base. This further accelerates the removal of water.

The effect of surfaces with cavity arrays has been studied numerically and experimentally (Silvestri et al., 2017; Bhat et al., 2021) with a reduction in turbulence energy close to the wall and a subsequent reduction in skin friction being observed. However, these studies do not account for the accompanying increase in pressure drag, which results in a net drag increase (Jawahar, 2022). Additionally, with the cavities in the LISHySs being optimised for liquid area and not the size of the coherent structures, as was the case with cavity array studies, the surfaces with open cavities are even more unlikely to produce drag reduction.

- **Droplets acting as roughness elements**

  The droplets infused into the test plates were designed to protrude only to the extent of the viscous sublayer. However, the imprecise technique of spraying that was employed meant that some of these droplets exceeded their desired size. By protruding further into the boundary layer, these effectively increase the roughness of the surface, thereby increasing the associated skin friction (Acharya et al., 1986; Tani, 1987; Chung et al., 2021).

  Apart from the infused droplets, some of the excess droplets that could not be removed from the top surface were found to strongly adhere to tiny patches that were not superhydrophobic. Not only are these responsible for skin friction and pressure drag of their own, but they also disrupt the motion of the liquid behind them. This is of higher consequence to the plate with cylindrical cavities because it disrupts the uniform rolling motion of the entire droplet. Regions behind the droplet on the surface would turn at a different speed as compared to the rest of the liquid volume, causing instabilities at the interface which could propagate into the flow, increasing turbulent fluctuations in the boundary layer.

- **Presence of spanwise slip**

  In the case of cylindrical droplets, particularly at and above the design velocity, the motion of the liquid-air interface is observed to be not only rotational but also along the length of the cavity. For SHSs and LISs, a reduction in skin friction was observed when fluid volumes were oriented in the streamwise direction. Streamwise slip was seen to suppress the formation of near-wall structures (Jelly et al., 2014) or by shifting them further away from the wall (Martell et al., 2010), thereby decreasing turbulence intensities and Reynolds stress in this region. On the other hand, spanwise slip countered drag reduction due to the strengthening of streamwise streaky structures (Min and Kim, 2004; Fukagata et al., 2006).

- **Wetting of superhydrophobic features**

  There are two ways in which wetting of the superhydrophobic cavities could occur:

  1. Non-uniform application of the coating within the cavities
     With cylindrical cavities, it is easier to ensure that the coating covers all parts of the cavities since more of it is exposed. This is tougher to guarantee with spherical cavities because there is only a small area through which the coating can enter the cavity. While cavities in sectioned test pieces were seen to be hazy white, indicating the presence of the coating, it cannot be said with certainty that the coating was spread evenly into each of the thousands of spherical cavities on the designed surfaces.
  2. Failure of superhydrophobic features at higher liquid rotation speeds
     As the speed of rotation of the droplet increases, the shear stress at the interface between the droplet and the microscopic air pockets inside the cavity also increases. Studies on SHSs (Samaha et al., 2012b; Aljallis et al., 2013) reported an increase in plastron depletion with increasing Re_τ, leading to the wetting of the features. Due to the shallow depth of the features, the hydrostatic pressure cannot be a reason for failure.

  When the superhydrophobic features are wetted, the skin friction experienced by the liquid in the cavity is significantly increased. As discussed in Section 2.6, there is a direct relation between the frictional force experienced by the droplet inside the cavity and the skin friction at the interface with the external flow. Thus, wet cavities would result in a net drag increase for the surfaces.

- **Wet patches on the surface**

  For one of the tiles of P-SC, it was observed that the top surface of a notable portion of it (roughly half the tile) did not exhibit superhydrophobicity. This could be due to improper cleaning or drying after the tile was printed. Thus, water that was sprayed in this region was seen to adhere to the top surface instead of going inside the cavities due to greater surface adhesion. This leads to an increase in drag due to the large unstable air-water interface that is exposed to the external flow. Smaller wet patches (covering tens of cavities) were also observed on a few other tiles.

6

Conclusions and recommendations

6.1. Conclusions

Slip-inducing surfaces, such as superhydrophobic surfaces and liquid-infused surfaces, have been shown to have drag reducing capabilities in turbulent flows (Fu et al., 2017; Park et al., 2021). This is achieved by the presence of a non-zero slip velocity at the fluid-fluid interface and the suppression or shift of near-wall turbulent structures. Inspired by these surfaces, a novel technique for drag reduction in aerodynamic applications was conceptualised, which employed the usage of liquid volumes trapped in superhydrophobic features. After designing and manufacturing two types of such surfaces, three experimental campaigns were formulated to test their drag reduction capabilities. However, no drag reduction was observed, with increases in both the skin friction and pressure drag components. The reasons for this are attributed to the liquid lost from the surface, droplets increasing the roughness of the suface and slip components that are not aligned with the direction of flow. While boundary layer profiles indicated reduced fluctuations in the overlap layer, this could not be confirmed closer to the wall. The answers to the research questions that were determined in Section 1.4 are provided below:

1. **The key factors in the theoretical framework for drag reduction are the superhydrophobicity of the surface and the geometrical parameters of the cavities.**

   The development of the theoretical framework is based on a comparison between the frictional forces acting on a smooth surface and a LISHyS. By balancing the torque equation to obtain a steady rolling motion for a liquid volume and accounting for the net force created by the frictional forces from the external flow and the resistance inside the cavity, a condition is derived for drag reduction, expressed by Equation (2.38). The key parameters involved are the superhydrophobicity of the cavity, the exposed area of the droplet, the area of the surface that has an air-liquid interface and the area of the superhydrophobic cavity in contact with the liquid. While the first three parameters are directly proportional to the friction produced, the last one is inversely proportional to it. With increasing superhydrophobicity and decreasing droplet size, the maximum expected drag reduction approaches the percentage of the area of the surface that has an air-liquid interface with respect to the total area.

2. **LISHySs can be manufactured in a three stage process - producing the cavity-laden surfaces, making them superhydrophobic and adding liquid into them**

   Due to the need for the liquid to rotate in place, the most promising designs involve the usage of liquid volumes trapped in either spherical cavities or cylindrical cavities. An analysis of available manufacturing techniques showed that a 3D printed surface with cavities that had been made superhydrophobic with the help of an industrial coating was the most viable option. Water was chosen to be the liquid used for the surfaces as it yielded the highest contact angle with the surface while having the lowest rate of evaporation. The manufactured surfaces were verified using a 3D measurement system and flat surface contact angle measurements.

3. **Direct force measurements and PIV were used to characterise drag over the produced surfaces. The results showed an increase in drag while also revealing issues with the measurement processes.**

Experimental campaigns were formulated to measure the total drag force of the manufactured surfaces and to quantify the flow field over them. For both tests, a smooth plate of equal dimensions was used as reference. The tests were also performed without the infusion of water for comparison. Drag measurements were performed for a velocity sweep between 5 m/s and 25 m/s. No drag reduction was observed throughout this range, with ΔC_D varying between 10% and 17% for the infused surface with spherical cavities. Particle image velocimetry was used to generate boundary layer profiles and determine integral boundary layer properties. An increase in the mean streamwise velocity and decrease in turbulent statistics were observed in the overlap layer. However, strong reflections at the surface were detrimental to the quality of results obtained, preventing the accurate study of near-wall data. Along with the decision to not test the cylindrical cavity design in the drag measurement test, this was also why a direct comparison of the drag produced by both of the designed surfaces could not be made. Pressure drag due to droplets acting as roughness elements, among other reasons, further contributes to the drag produced by the surface. In the matter of liquid retention, the surface with spherical droplets lost water more easily due to the lower volume of liquid in these droplets.

4. **The hypothesised working principle was verified at low velocities through observations of the air-liquid interface.**

   In order to observe the motion of the liquid inside a cavity, new surfaces were created with a larger liquid-air interface area. A fixture to secure it, dubbed the Knoll, was created and placed downstream of a zigzag strip to trip the boundary layer. A Micro Alignment Telescope and a DSLR camera were used to capture images and videos of the flow over the surface with dust particles acting as tracers in the water droplets. A steady rolling motion of the droplets was observed at 5 m/s and this was accelerated with increasing freestream velocity. However, there was a corresponding growth in spanwise and other chaotic motion.

In an ideal scenario, the expected drag reduction approaches the value of the percentage of the wetted area (as high as 37% for cylindrical droplets) as the surface's hydrophobicity and the exposed area of the droplet are increased. However, due to the unfavourable area ratio (exposed area to area submerged in the cavity) in the framework, the size of the droplets required becomes more minuscule. Coupled with the greater significance of evaporation on individual droplets and the increased difficulty in manufacturing superhydrophobic surfaces with thousands or millions of ordered microscopic cavities, pursuing further research on LISHySs with spherical droplets is likely to be futile. In the current implementation, it would be interesting to conduct further analysis on surfaces with cylindrical droplets, as outlined in the following section.

6.2. Recommendations for further research

Having carried out the very first study on the design, production and assessment of LISHySs, the author recommends that the following factors be considered while carrying out further research on these surfaces.

- **Utilising streamwise droplets**

  Since studies on SHSs and LISs found the highest degree of drag reduction in the case of streamwise grooves, orienting the cylindrical droplets in a streamwise orientation instead of in the spanwise direction could be fruitful. This is because streamwise droplets would promote streamwise slip, decreasing near-wall turbulence intensities and Reynolds stress.

  An idea for such a surface has been shown in Figure 6.1. Apart from facilitating the rolling motion, a reason to use spanwise cylindrical droplets was to improve retention. If these droplets had been oriented in the streamwise direction, due to the lack of adhesion between the liquid and the base surface, rapid drainage was expected. Thus, streamwise droplets would need to be created with a mechanism to recirculate the liquid. As seen in the figure, the part of the droplet that is not aligned with the direction of the freestream should be covered so that it does not affect the flow. To avoid creating multiple channels for recirculation, the cavities could drain into and draw fluid from a reservoir under them. This would allow for a larger portion of the surface to have an air-liquid interface. Additionally, a system could be introduced to pump water into the reservoir to account for the depletion in liquid due to evaporation or shear drainage. Note that the shape of the droplet no longer needs to be cylindrical as the motion of the droplet is altered from rotational to linear.

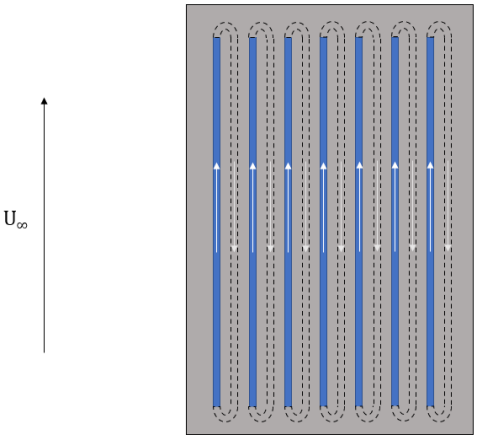

Figure 6.1: LISHyS with streamwise-oriented liquid volumes

- **Alternative production process for the superhydrophobic base surface**

  While the superhydrophobic coating that was used could produce contact angles of up to 165°, spraying the coating evenly and ensuring that all portions of the cavity-laden surface were covered was challenging. Processes such as photolithography (Maynes et al., 2007) and gas-plasma etching (Checco et al., 2014) could be used to produce surfaces with ordered microscopic roughness that traps air, allowing the surface to exhibit uniform superhydrophobicity. Electrospinning, which involves the electrification of liquid polymer droplets to generate a jet that is stretched to make fibres, has been able to create SHSs with contact angles as high as 169°(Oktay et al., 2015). The main disadvantages of these techniques over the coating are the time and cost of production, especially on large samples such as the test plates created in this study. It is thus important to stay updated with advances in manufacturing non-wettable surfaces.

- **Liquid infusion process**

  The spraying of water into the cavities was observed to be imprecise, resulting in both underfilled and overfilled cavities. This was a greater issue in the case of the surface with spherical cavities. In order to control the height of the air-liquid interface, liquid should be directed into the cavities in a controlled manner. This would be simpler to execute with the aforementioned surface with a reservoir, wherein the total volume of liquid in the system can be regulated.

- **Alternative quantification and visualisation techniques**

  During the DFM test, it was not possible to test P-CC due to the risk of damage to the measurement device. Additionally, measurements on this test plate were tricky during the PIV campaign due to the magnitude of reflections on the surface. Observing the interface confirmed rolling motion in the case of cylindrical droplets but this could not be observed with spherical droplets due to the small sizes of the interfaces. Developing transparent superhydrophobic samples, which was unsuccessful during this study, would provide insights into the actual motion inside the cavity. While altering the surface production method could result in one that is more suited to PIV tests, it is worth analysing the available measurement techniques to find or build upon one that is more suited to LISHySs.

- **Direct numerical simulations on the flow over and inside LISHySs**

  As discussed above, limitations created by the properties of the surface and the test setup prevented accurate measurements being made of flow near the wall and fluid motion inside the cavity. DNS studies could provide more insight into these aspects. One study on a similar type of surface was performed by Hemeda and Tafreshi (2016), who explored drag reduction on liquid-infused surfaces with trapped air. Building upon the concept of LISs, a layer of air trapped under the infused liquid was introduced to reduce the frictional forces. A drag reduction of 20% to 37% was expected in cases wherein the viscosity of the liquid exceeded that of the bulk medium. However, realistically creating such a surface (one that selectively wets a lubricant while trapping air underneath) brings its own set of challenges.

- **Replacing liquid droplets with solid moving surfaces**

  Liquid droplets on the surface exist to provide slip at the wall. While a fluid interface with the bulk medium offers high slip in a passive manner, using a liquid to create slip brings issues with it, as has been seen in this study. Infusing the liquid and retaining it are challenging due to the fine size of the cavities, the lack of adhesion with the base surface, the shear force of the freestream and evaporation. Thus, replacing the air-liquid interface with a moving solid-air interface, either passive or active, could be a more lucrative implementation. Olivucci et al. (2021) performed a numerical study on half discs rotating at a finite angular velocity, aligned with the direction of the freestream. They observed a large reduction of turbulence activity and skin-friction drag over the spinning portion of the discs with a maximum total drag reduction of 5.6%.

- **Testing in the laminar regime**

  As the broader goal for this thesis was concerned with sustainability in aviation, wherein the boundary layer over most of an aircraft is turbulent, this thesis explored an application of this novel idea in the turbulent regime. However, LISHySs cannot be used in aviation because the high shear stress would cause rapid depletion of the lubricant. Also, water in the cavities would be frozen at cruise altitudes. At lower altitudes, during manoeuvres, liquid would be moving around, causing additional disturbances in the flow while also hindering the balance of the aircraft. The liquid motion visualisation campaign indicated that steady rolling motion, without spanwise motion, was observed at low velocities. Without the presence of fluctuations close to the wall, the likelihood for this steady motion to continue is greater. Thus, it will be interesting to test whether this technique could achieve drag reduction in the laminar regime. This is also more likely to succeed in the case of streamwise-oriented droplets as the difference in velocity over the wet and dry areas in surfaces with spanwise-oriented droplets could trigger transition to turbulence.

Bibliography

Acharya, M., Bornstein, J., & Escudier, M. P. (1986). Turbulent boundary layers on rough surfaces. *Experiments in Fluids*, *4*(1), 33–47. https://doi.org/10.1007/BF00316784

Aljallis, E., Sarshar, M. A., Datla, R., Sikka, V., Jones, A., & Choi, C.-H. (2013). Experimental study of skin friction drag reduction on superhydrophobic flat plates in high reynolds number boundary layer flow. *Physics of Fluids*, *25*(2), 025103. https://doi.org/10.1063/1.4791602

Arenas, I., Garciá, E., Fu, M. K., Orlandi, P., Hultmark, M., & Leonardi, S. (2019). Comparison between superhydrophobic, liquid infused and rough surfaces: A direct numerical simulation study. *Journal of Fluid Mechanics*, *869*, 500–525. https://doi.org/10.1017/jfm.2019.222

Balasubramanian, R., & Orszag, S. A. (1980). *Drag reduction effects in turbulent boundary layers over wavy walls* (Contractor Report No. 159305). NASA. https://ntrs.nasa.gov/citations/19800019808

Benedict, L. H., & Gould, R. D. (1996). Towards better uncertainty estimates for turbulence statistics. *Experiments in Fluids*, *22*(2), 129–136. https://doi.org/10.1007/s003480050030

Berghout, P., Bullee, P. A., Fuchs, T., Scharnowski, S., Kähler, C. J., Chung, D., Lohse, D., & Huisman, S. G. (2021). Characterizing the turbulent drag properties of rough surfaces with a taylor–couette set-up. *Journal of Fluid Mechanics*, *919*, A45. https://doi.org/10.1017/jfm.2021.413

Bhat, S. S., Silvestri, A., Cazzolato, B. S., & Arjomandi, M. (2021). Mechanism of control of the near-wall turbulence using a micro-cavity array. *Physics of Fluids*, *33*(7), 075114. https://doi.org/10.1063/5.0051375

Bhushan, B., & Jung, Y. C. (2011). Natural and biomimetic artificial surfaces for superhydrophobicity, self-cleaning, low adhesion, and drag reduction. *Progress in Materials Science*, *56*(1), 1–108. https://doi.org/https://doi.org/10.1016/j.pmatsci.2010.04.003

Bidkar, R. A., Leblanc, L., Kulkarni, A. J., Bahadur, V., Ceccio, S. L., & Perlin, M. (2014). Skin-friction drag reduction in the turbulent regime using random-textured hydrophobic surfaces. *Physics of Fluids*, *26*(8), 085108. https://doi.org/10.1063/1.4892902

Bohn, H. F., & Federle, W. (2004). Insect aquaplaning: *Nepenthes* pitcher plants capture prey with the peristome, a fully wettable water-lubricated anisotropic surface. *Proceedings of the National Academy of Sciences*, *101*(39), 14138–14143. https://doi.org/10.1073/pnas.0405885101

Brinkman, H. (1949). A calculation of the viscous force exerted by a flowing fluid on a dense swarm of particles. *Appl. Sci. Res*, *1*(27). https://doi.org/10.1007/BF02120313

Brocher, F. (1913). Recherches sur la respiration des insectes aquatiques (imagos). nèpe, hydrophile, notonecte, dyticidés, haemonia, elmidés. *Internationale Revue der gesamten Hydrobiologie und Hydrographie*, *6*(2-3), 250–256. https://doi.org/https://doi.org/10.1002/iroh.19130060207

Brown, P., & Mazumder, P. (2021). Current progress in mechanically durable water-repellent surfaces: A critical review. *Reviews of Adhesion and Adhesives*, *9*, 123–152. https://doi.org/10.7569/RAA.2021.097301

Buck, A. L. (1981). New Equations for Computing Vapor Pressure and Enhancement Factor. *Journal of Applied Meteorology and Climatology*, *20*(12), 1527–1532. https://doi.org/10.1175/1520-0450(1981)020<1527:NEFCVP>2.0.CO;2

Busse, A., & Sandham, N. D. (2012). Influence of an anisotropic slip-length boundary condition on turbulent channel flow. *Physics of Fluids*, *24*(5), 055111. https://doi.org/10.1063/1.4719780

Cassie, A. B. D., & Baxter, S. (1944). Wettability of porous surfaces. *Transactions of the Faraday Society*, *40*, 546–551. https://doi.org/10.1039/tf9444000546

Ceccio, S. L. (2010). Friction drag reduction of external flows with bubble and gas injection. *Annual Review of Fluid Mechanics*, *42*(1), 183–203. https://doi.org/10.1146/annurev-fluid-121108-145504

Chang, J., Jung, T., Choi, H., & Kim, J. (2019). Predictions of the effective slip length and drag reduction with a lubricated micro-groove surface in a turbulent channel flow. *Journal of Fluid Mechanics*, *874*, 797–820. https://doi.org/10.1017/jfm.2019.468

Chauhan, K. A., Monkewitz, P. A., & Nagib, H. M. (2009). Criteria for assessing experiments in zero pressure gradient boundary layers. *Fluid Dynamics Research*, *41*(2), 021404. https://doi.org/10.1088/0169-5983/41/2/021404

Checco, A., Rahman, A., & Black, C. T. (2014). Robust superhydrophobicity in large-area nanostructured surfaces defined by block-copolymer self assembly. *Advanced Materials*, *26*(6), 886–891. https://doi.org/https://doi.org/10.1002/adma.201304006

Choi, C. H., & Kim, C. J. (2006). Large slip of aqueous liquid flow over a nanoengineered superhydrophobic surface. *Physical review letters*, *96*, 066001. https://doi.org/10.1103/PhysRevLett.96.066001

Chung, D., Hutchins, N., Schultz, M. P., & Flack, K. A. (2021). Predicting the drag of rough surfaces. *Annu. Rev. Fluid Mech. 2021*, *53*, 439–471. https://doi.org/10.1146/annurev-fluid-062520

Daniello, R. J., Waterhouse, N. E., & Rothstein, J. P. (2009). Drag reduction in turbulent flows over superhydrophobic surfaces. *Physics of Fluids*, *21*(8), 085103. https://doi.org/10.1063/1.3207885

Darcy. (1856). *H. les fontaines publiques de la ville de dijon.recherche*.

Deng, Y., Mager, D., Bai, Y., Zhou, T., Liu, Z., Wen, L., Wu, Y., & Korvink, J. G. (2018). Inversely designed microtextures for robust cassie–baxter mode of super-hydrophobicity. *Computer Methods in Applied Mechanics and Engineering*, *341*, 113–132. https://doi.org/https://doi.org/10.1016/j.cma.2018.06.034

Fairhall, C. T., Abderrahaman-Elena, N., & García-Mayoral, R. (2019). Turbulent flows over superhydrophobic surfaces: Flow-induced capillary waves, and robustness of air-water interfaces. *Journal of Fluid Mechanics*, *835*, 45–85. https://doi.org/10.1017/jfm.2017.733

Fu, M. K., Arenas, I., Leonardi, S., & Hultmark, M. (2017). Liquid-infused surfaces as a passive method of turbulent drag reduction. *Journal of Fluid Mechanics*, *824*, 688–700. https://doi.org/10.1017/jfm.2017.360

Fukagata, K., Kasagi, N., & Koumoutsakos, P. (2006). A theoretical prediction of friction drag reduction in turbulent flow by superhydrophobic surfaces. *Physics of Fluids*, *18*(5), 051703. https://doi.org/10.1063/1.2205307

Gad-el-Hak, M. (2000). *Flow control: Passive, active, and reactive flow management*. Cambridge University Press. https://doi.org/10.1017/CBO9780511529535

Gloukhovski, R., Freger, V., & Tsur, Y. (2018). Understanding methods of preparation and characterization of pore-filling polymer composites for proton exchange membranes: A beginner's guide. *Reviews in Chemical Engineering*, *34*(4), 455–479. https://doi.org/10.1515/revce-2016-0065

Gómez-de-Segura, G., Fairhall, C. T., MacDonald, M., Chung, D., & García-Mayoral, R. (2018). Manipulation of near-wall turbulence by surface slip and permeability. *Journal of Physics: Conference Series*, *1001*, 012011. https://doi.org/10.1088/1742-6596/1001/1/012011

Gose, J. W., Golovin, K., Boban, M., Mabry, J. M., Tuteja, A., Perlin, M., & Ceccio, S. L. (2018). Characterization of superhydrophobic surfaces for drag reduction in turbulent flow. *Journal of Fluid Mechanics*, *845*, 560–580. https://doi.org/10.1017/jfm.2018.210

Grau, J. C. (2022). *Chevron-shaped protrusions for turbulent drag reduction* (Master's thesis). Delft University of Technology. http://resolver.tudelft.nl/uuid:b4d38b0a-2e60-48b1-a2a6-8a5c8a3bbdb2

Haibao, H., Peng, D., Feng, Z., Dong, S., & Yang, W. (2015). Effect of hydrophobicity on turbulent boundary layer under water. *Experimental Thermal and Fluid Science*, *60*, 148–156. https://doi.org/10.1016/j.expthermflusci.2014.08.013

Hartog, F. H. (2021). *Turbulent boundary layers over surfaces with streamwise-preferential permeability: Experimental investigation into the drag and flow mechanics* (Master thesis). Delft University of Technology. http://resolver.tudelft.nl/uuid:0797d3d4-ff30-460c-a5b6-6ff732eb6ffd

Hemeda, A. A., & Tafreshi, H. V. (2016). Liquid–infused surfaces with trapped air (lista) for drag force reduction. *Langmuir*, *32*(12), 2955–2962. https://doi.org/10.1021/acs.langmuir.5b04754

Henoch, C., Krupenkin, T., Kolodner, P., Taylor, J., Hodes, M., Lyons, A., Peguero, C., & Breuer, K. (2006). Turbulent drag reduction using superhydrophobic surfaces. *AIAA Paper*. https://doi.org/10.2514/6.2006-3192

Huhtamäki, T., Tian, X., Korhonen, J. T., & Ras, R. H. (2018). Surface-wetting characterization using contact-angle measurements. *Nature protocols*, *13*(7), 1521–1538.

Hussain, A. K. M. F. (1983). Coherent structures—reality and myth. *The Physics of Fluids*, *26*(10), 2816–2850. https://doi.org/10.1063/1.864048

IEA. (2022a). *Aviation tracking report*. https://www.iea.org/reports/aviation

IEA. (2022b). *Transport tracking report*. https://www.iea.org/reports/transport

Im, H. J., & Lee, J. H. (2017). Comparison of superhydrophobic drag reduction between turbulent pipe and channel flows. *Physics of Fluids*, *29*(9), 095101. https://doi.org/10.1063/1.5000729

Israelachvili, J. (2011). *Polymer interface and adhesion*. Elsevier, New York. https://doi.org/10.1016/C2011-0-05119-0

Jawahar, S. (2022). *Wall-normal pores for turbulent drag reduction: Experimental investigation into drag performance and flow mechanics* (Master thesis). Delft University of Technology. http://resolver.tudelft.nl/uuid:dea317b8-57ba-4072-bd36-fd9408c7a5c8

Jelly, T. O., Jung, S. Y., & Zaki, T. A. (2014). Turbulence and skin friction modification in channel flow with streamwise-aligned superhydrophobic surface texture. *Physics of Fluids*, *26*(9), 095102. https://doi.org/10.1063/1.4894064

Jhmadden. (2015). *Wikimedia Commons*. https://commons.wikimedia.org/wiki/File:Spherical_cap_diagram.tiff

Johnson, R. E. (1993). Wetting of low-energy surfaces. In J. C. Berg (Ed.), *Wettability*. Marcel Dekker Inc., New York. https://doi.org/10.1201/9781482277500

Kim, H. N., & Lee, S. J. (2021). Shear-driven drainage of lubricant in a spherical cavity of lubricant-infused surface. *Physics of Fluids*, *33*, 122011. https://doi.org/10.1063/5.0074107

Kornilov, V. (2015). Current state and prospects of researches on the control of turbulent boundary layer by air blowing. *Progress in Aerospace Sciences*, *76*, 1–23. https://doi.org/10.1016/j.paerosci.2015.05.001

Lafuma, A., & Quéré, D. (2003). Superhydrophobic states. *Nature materials*, *2*(7), 457–460. https://doi.org/10.1038/nmat924

Lai, Y.-J. (2021). *Turbulent Viscous Drag Reduction in Air by Compliant Surfaces* (Master thesis). Delft University of Technology. http://resolver.tudelft.nl/uuid:a470acae-1238-4e47-a986-11fc69378f6b

Lee, C., Choi, C., & Kim, C. (2008). Structured surfaces for a giant liquid slip. *Physical Review Letters*, *101*(6). https://doi.org/10.1103/PhysRevLett.101.064501

Ling, H., Katz, J., Fu, M., & Hultmark, M. (2017). Effect of reynolds number and saturation level on gas diffusion in and out of a superhydrophobic surface. *Phys. Rev. Fluids*, *2*, 124005. https://doi.org/10.1103/PhysRevFluids.2.124005

Liu, Y., Wexler, J. S., Schönecker, C., & Stone, H. A. (2016). Effect of viscosity ratio on the shear-driven failure of liquid-infused surfaces. *Physical Review Fluids*, *1*. https://doi.org/10.1103/PhysRevFluids.1.074003

Martell, M. B., Rothstein, J. P., & Perot, J. B. (2010). An analysis of superhydrophobic turbulent drag reduction mechanisms using direct numerical simulation. *Physics of Fluids*, *22*(6), 065102. https://doi.org/10.1063/1.3432514

Maynes, D., Jeffs, K., Woolford, B., & Webb, B. W. (2007). Laminar flow in a microchannel with hydrophobic surface patterned microribs oriented parallel to the flow direction. *Physics of Fluids*, *19*(9), 093603. https://doi.org/10.1063/1.2772880

Min, T., & Kim, J. (2004). Effects of hydrophobic surface on skin-friction drag. *Physics of Fluids*, *16*(7), L55–L58. https://doi.org/10.1063/1.1755723

Mohammadi, A., & Smits, A. (2016). Stability of two-immiscible-fluid systems: A review of canonical plane parallel flows. *Journal of Fluids Engineering, Transactions of the ASME*, *138*(10). https://doi.org/10.1115/1.4033969

Monkewitz, P. A., Chauhan, K. A., & Nagib, H. M. (2007). Self-consistent high-reynolds-number asymptotics for zero-pressure-gradient turbulent boundary layers. *Physics of Fluids*, *19*(11), 115101. https://doi.org/10.1063/1.2780196

Murai, Y. (2014). Frictional drag reduction by bubble injection. *Experiments in Fluids*, *55*. https://doi.org/10.1007/s00348-014-1773-x

Musker, A. J. (1979). Explicit expression for the smooth wall velocity distribution in a turbulent boundary layer. *AIAA Journal*, *17*(6), 655–657. https://doi.org/10.2514/3.61193

Oktay, B., Toker, R., & Kayaman-Apohan, N. (2015). Superhydrophobic behavior of polyimide–siloxane mats produced by electrospinning. *Polymer Bulletin*, *72*. https://doi.org/10.1007/s00289-015-1438-9

Olivucci, P., Wise, D. J., & Ricco, P. (2021). Reduction of turbulent skin-friction drag by passively rotating discs. *Journal of Fluid Mechanics*, *923*, A8. https://doi.org/10.1017/jfm.2021.533

Ou, J., Perot, J., & Rothstein, J. (2004). Laminar drag reduction in microchannels using ultrahydrophobic surfaces. *Physics of Fluids*, *16*, 4635–4643. https://doi.org/10.1063/1.1812011

Park, H., Choi, C. H., & Kim, C. J. (2021). Superhydrophobic drag reduction in turbulent flows: A critical review. *Experiments in Fluids*, *62*. https://doi.org/10.1007/s00348-021-03322-4

Park, H., Sun, G., & Kim, C.-J. “ (2014). Superhydrophobic turbulent drag reduction as a function of surface grating parameters. *Journal of Fluid Mechanics*, *747*, 722–734. https://doi.org/10.1017/jfm.2014.151

Park, H., Park, H., & Kim, J. (2013). A numerical study of the effects of superhydrophobic surface on skin-friction drag in turbulent channel flow. *Physics of Fluids*, *25*(11), 110815. https://doi.org/10.1063/1.4819144

Piao, L. (2015). Two-dimensional analysis of air–water interface on superhydrophobic grooves under fluctuating water pressure. *Langmuir: the ACS journal of surfaces and colloids, 31*. https://doi.org/10.1021/acs.langmuir.5b01847

Poetes, R., Holtzmann, K., Franze, K., & Steiner, U. (2010). Metastable underwater superhydrophobicity. *Phys. Rev. Lett., 105*, 166104. https://doi.org/10.1103/PhysRevLett.105.166104

Prandtl, L. (1904). Ueber flussigkeitsbewegung bei sehr kleiner reibung. *Verhandl. III, Internat. Math.-Kong., Heidelberg, Teubner, Leipzig, 1904*, 484–491. https://cir.nii.ac.jp/crid/1573105976183769600

Raffel, M., Willert, C. E., & Kompenhans, J. (1998). *Particle Image Velocimetry: A Practical Guide*. Springer. https://books.google.nl/books?id=enOLTmfYVPQC

Rastegari, A., & Akhavan, R. (2015). On the mechanism of turbulent drag reduction with super-hydrophobic surfaces. *Journal of Fluid Mechanics, 773*, R4. https://doi.org/10.1017/jfm.2015.266

Ritchie, H. (2020). *Climate change and flying: What share of global co2 emissions come from aviation?* Our World in Data. https://ourworldindata.org/co2-emissions-from-aviation

Rodríguez-López, E., Bruce, P. J. K., & Buxton, O. R. H. (2015). A robust post-processing method to determine skin friction in turbulent boundary layers from the velocity profile. *Experiments in Fluids, 56*. https://doi.org/10.1007/s00348-015-1935-5

Rosenberg, B. J., van Buren, T., Fu, M. K., & Smits, A. J. (2016). Turbulent drag reduction over air- and liquid-impregnated surfaces [Important paper - manufacturing techniques for SHP and LIS]. *Physics of Fluids, 28*. https://doi.org/10.1063/1.4939272

Rosti, M. E., & Brandt, L. (2017). Numerical simulation of turbulent channel flow over a viscous hyper-elastic wall. *Journal of Fluid Mechanics, 830*, 708–735. https://doi.org/10.1017/jfm.2017.617

Samaha, M., Tafreshi, H., & Gad-el-Hak, M. (2012a). Effects of hydrostatic pressure on the drag reduction of submerged aerogel-particle coatings. *Colloids and Surfaces A: Physicochemical and Engineering Aspects, 399*, 62–70. https://doi.org/10.1016/j.colsurfa.2012.02.025

Samaha, M. A., Tafreshi, H. V., & Gad-el-Hak, M. (2012b). Superhydrophobic surfaces: From the lotus leaf to the submarine [Biomimetic flow control]. *Comptes Rendus Mécanique, 340*(1), 18–34. https://doi.org/10.1016/j.crme.2011.11.002

Scarano, F. (2013). *Ae4180 experimental aerodynamics* (1st ed., Course reader). Delft University of Technology.

Schlatter, P., & Örlü, R. (2010). Assessment of direct numerical simulation data of turbulent boundary layers. *Journal of Fluid Mechanics, 659*, 116–126. https://doi.org/10.1017/s0022112010003113

Schönecker, C., Baier, T., & Hardt, S. (2014). Influence of the enclosed fluid on the flow over a microstructured surface in the cassie state. *Journal of Fluid Mechanics, 740*, 168–195. https://doi.org/10.1017/jfm.2013.647

Schrauf, G., Gölling, B., & Wood, N. (2006). Katnet - key aerodynamic technologies for aircraft performance improvement. *Fifth Community Aeronautical Days, Vienna, Austria*. https://trimis.ec.europa.eu/sites/default/files/project/documents/20121105_140611_34998_2006_aerodays_KATnet.pdf

Seo, J., García-Mayoral, R., & Mani, A. (2015). Pressure fluctuations and interfacial robustness in turbulent flows over superhydrophobic surfaces. *Journal of Fluid Mechanics, 783*, 448–473. https://doi.org/10.1017/jfm.2015.573

Silvestri, A., Ghanadi, F., Arjomandi, M., Cazzolato, B., & Zander, A. (2017). Attenuation of sweep events in a turbulent boundary layer using micro-cavities. *Experiments in Fluids, 58*. https://doi.org/10.1007/s00348-017-2345-7

Srinivasan, S., Kleingartner, J. A., Gilbert, J. B., Cohen, R. E., Milne, A. J. B., & McKinley, G. H. (2015). Sustainable drag reduction in turbulent taylor-couette flows by depositing sprayable superhydrophobic surfaces. *Phys. Rev. Lett., 114*, 014501. https://doi.org/10.1103/PhysRevLett.114.014501

Suga, K., Matsumura, Y., Ashitaka, Y., Tominaga, S., & Kaneda, M. (2010). Effects of wall permeability on turbulence. *International Journal of Heat and Fluid Flow, 31*(6), 974–984. https://doi.org//10.1016/j.ijheatfluidflow.2010.02.023

Sun, H., Lei, F., Li, T., Han, H., Li, B., Li, D., & Sun, D. (2021). Facile fabrication of novel multifunctional lubricant-infused surfaces with exceptional tribological and anticorrosive properties. *ACS Applied Materials and Interfaces, 13*, 6678–6687. https://doi.org/10.1021/acsami.0c21667

Tani, I. (1987). Turbulent boundary layer development over rough surfaces. In H. U. Meier & P. Bradshaw (Eds.), *Perspectives in turbulence studies* (pp. 223–249). Springer Berlin Heidelberg. https://doi.org/10.1007/978-3-642-82994-9_9

Tian, H., Zhang, J., Wang, E., Yao, Z., & Jiang, N. (2015). Experimental investigation on drag reduction in turbulent boundary layer over superhydrophobic surface by TRPIV. *Theoretical and Applied Mechanics Letters*, *5*(1), 45–49. https://doi.org/10.1016/j.taml.2015.01.003

Truesdell, R., Mammoli, A., Vorobieff, P., van Swol, F., & Brinker, C. J. (2006). Drag reduction on a patterned superhydrophobic surface. *Phys. Rev. Lett.*, *97*, 044504. https://doi.org/10.1103/PhysRevLett.97.044504

Vajdi Hokmabad, B., & Ghaemi, S. (2016). Turbulent flow over wetted and non-wetted superhydrophobic counterparts with random structure. *Physics of Fluids*, *28*(1), 015112. https://doi.org/10.1063/1.4940325

van Buren, T., & Smits, A. J. (2017). Substantial drag reduction in turbulent flow using liquid-infused surfaces. *Journal of Fluid Mechanics*, *827*, 448–456. https://doi.org/10.1017/jfm.2017.503

van Nesselrooij, M., van Campenhout, O. W., van Oudheusden, B. W., Schrijer, F. F., & Veldhuis, L. L. (2022). Development of an experimental apparatus for flat plate drag measurements and considerations for such measurements. *Measurement Science and Technology*, *33*. https://doi.org/10.1088/1361-6501/ac527f

van Oudheusden, B. W. (2020). Viscous Flows - Incompressible Turbulent Flow.

von Kármán, T., & Rubach, H. (1912). Über den mechanismus des flüssigkeits-und luftwiderstandes phys. *Phys. Z.*, *13*(2), 49–59.

Wenzel, R. N. (1936). Resistance of solid surfaces to wetting by water. *Industrial & Engineering Chemistry*, *28*(8), 988–994. https://doi.org/10.1021/ie50320a024

Wexler, J. S., Jacobi, I., & Stone, H. A. (2015). Shear-driven failure of liquid-infused surfaces. *Phys. Rev. Lett.*, *114*, 168301. https://doi.org/10.1103/PhysRevLett.114.168301

White, F. M. (2006). *Viscous Fluid Flow* (Vol. 3). McGraw-Hill New York. https://books.google.nl/books?id=fl6wPwAACAAJ

Wong, T. S., Kang, S. H., Tang, S. K., Smythe, E. J., Hatton, B. D., Grinthal, A., & Aizenberg, J. (2011). Bioinspired self-repairing slippery surfaces with pressure-stable omniphobicity. *Nature*, *477*, 443–447. https://doi.org/10.1038/nature10447

Woolford, B., Prince, J., Maynes, D., & Webb, B. W. (2009). Particle image velocimetry characterization of turbulent channel flow with rib patterned superhydrophobic walls. *Physics of Fluids*, *21*(8), 085106. https://doi.org/10.1063/1.3213607

Wu, D., Zhang, D., Ye, Y., Ma, L., Minhas, B., Liu, B., Terryn, H. A., Mol, J. M., & Li, X. (2019). Durable lubricant-infused anodic aluminum oxide surfaces with high-aspect-ratio nanochannels. *Chemical Engineering Journal*, *368*, 138–147. https://doi.org/10.1016/J.CEJ.2019.02.163

Wu, S. (1982). *Polymer interface and adhesion*. Marcel Dekker Inc., New York.

Xu, M., Grabowski, A., Yu, N., Kerezyte, G., Lee, J.-W., Pfeifer, B. R., & Kim, C.-J. " (2020). Superhydrophobic drag reduction for turbulent flows in open water. *Phys. Rev. Applied*, *13*, 34–56. https://doi.org/10.1103/PhysRevApplied.13.034056

Xu, M., Yu, N., Kim, J., & Kim, C.-J. (2021). Superhydrophobic drag reduction in high-speed towing tank. *Journal of Fluid Mechanics*, *908*. https://doi.org/10.1017/jfm.2020.872

Yeginbayeva, I. A., & Atlar, M. (2018). An experimental investigation into the surface and hydrodynamic characteristics of marine coatings with mimicked hull roughness ranges. *Biofouling*, *34*(9), 1001–1019. https://doi.org/10.1080/08927014.2018.1529760

Young, T. (1805). III. An essay on the cohesion of fluids. *Philosophical Transactions of the Royal Society of London*, *95*, 65–87. https://doi.org/10.1098/rstl.1805.0005

Zhang, J., Tian, H., Yao, Z., Hao, P., & Jiang, N. (2015). Mechanisms of drag reduction of superhydrophobic surfaces in a turbulent boundary layer flow. *Experiments in Fluids*, *56*. https://doi.org/10.1007/s00348-015-2047-y

Zhao, J.-P., Du, X.-D., & Shi, X.-H. (2007). Experimental research on friction-reduction with super-hydrophobic surfaces. *Journal of Marine Science and Application*, *6*(3), 58–61. https://doi.org/10.1007/s11804-007-7007-3

A

Renderings of surfaces produced through various manufacturing techniques

A.1. Milled surfaces

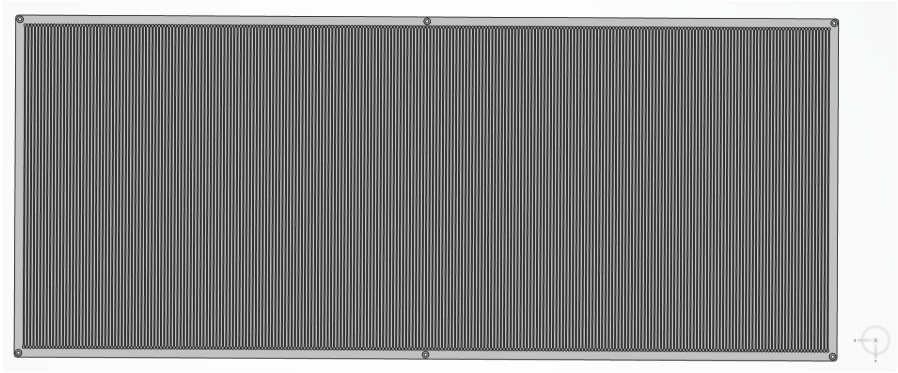

Figure A.1: Rendering of a milled plate with cylindrical cavities

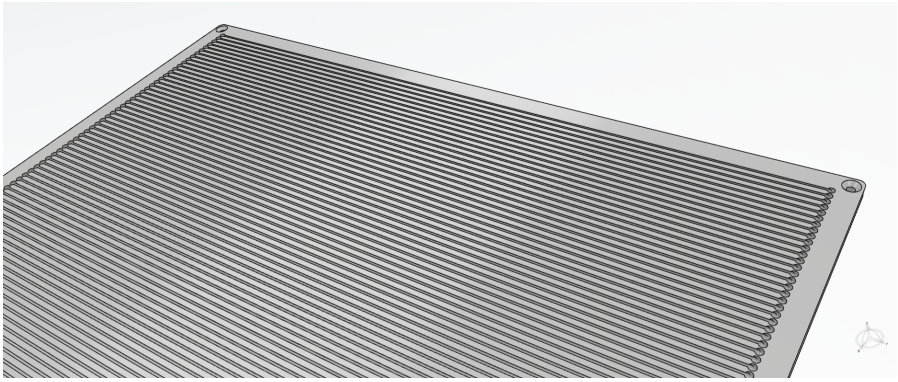

Figure A.2: A closer view of the grooves

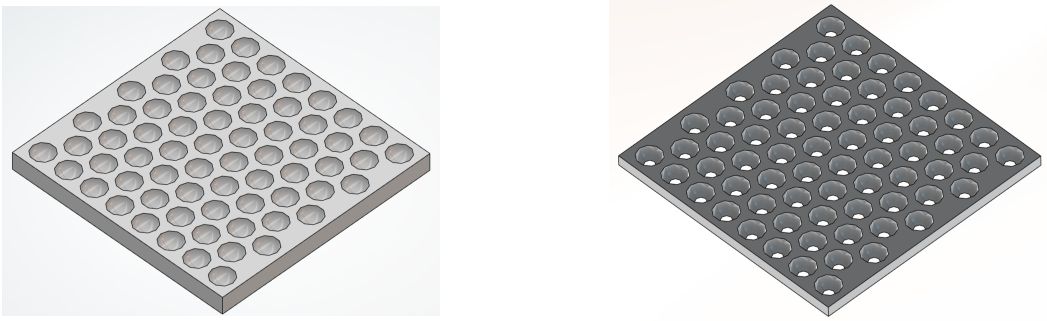

(a) Lower surface, viewed from above

(b) Upper surface, viewed from below

Figure A.3: Rendering of a portion of the 2-piece milled test plate with spherical cavities

A.2. Etched surfaces

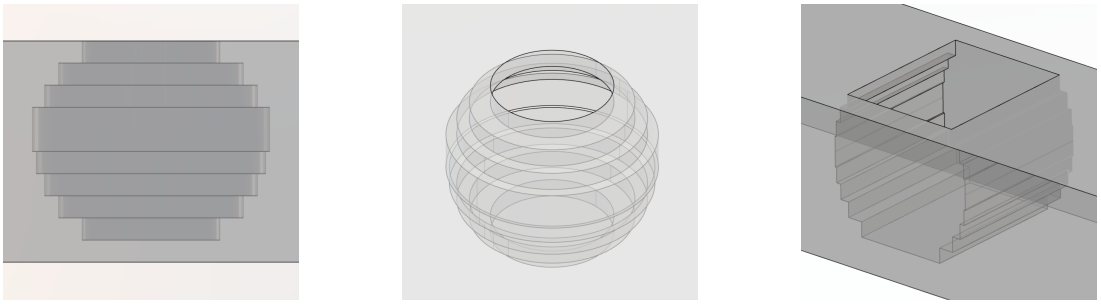

(a) Cross-sectional view

(b) Spherical cavity

(c) Cylindrical cavity

Figure A.4: Renderings of spherical and cylindrical cavities assembled by stacking etched sheets

A.3. Laser-cut surfaces

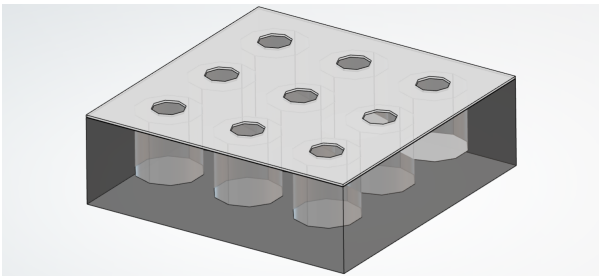

Figure A.5: Rendering of two stacked laser cut surfaces (black: base, white: lid)

B

Sandpaper tests for hydrophobicity

In order to find out whether rough surfaces could be used to increase the contact angle of water droplets, sandpaper strips with different grit sizes (240, 400 and 800 grit) were tested. Since the marine spray did not exhibit hydrophobicity on a flat surface, this was not tested. Droplets of distilled water were placed with a syringe onto the surfaces and images were taken using a DSLR camera.

B.1. Uncoated samples

Figure B.1 shows the water droplets that were formed on uncoated sandpaper strips.

(a) 240 grit (b) 400 grit (c) 800 grit

Figure B.1: Water droplets on uncoated sandpaper strips

B.2. Samples coated with clothing spray

Figure B.2 shows the water droplets that were formed on sandpaper strips that were coated with SMW Anti-Rain Protector.

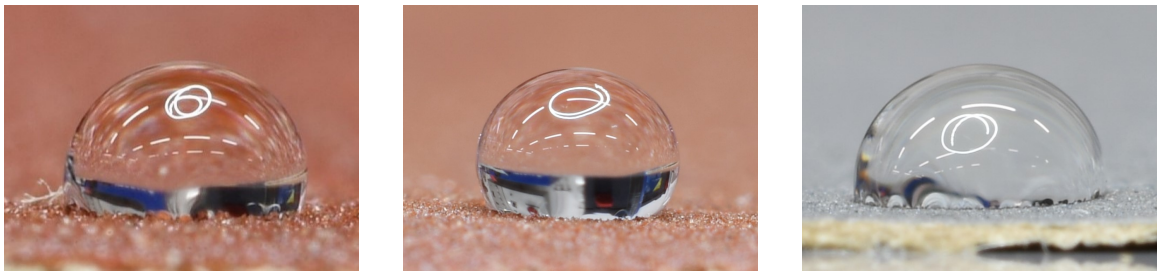

(a) 240 grit (b) 400 grit (c) 800 grit

Figure B.2: Water droplets on sandpaper strips coated with clothing spray

B.3. Samples coated with automotive spray

Figure B.3 shows the water droplets that were formed on sandpaper strips that were coated with Wowo's Crystal Sealant.

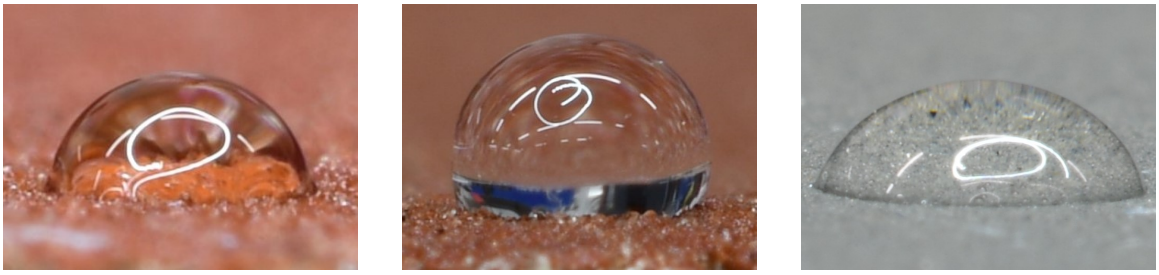

(a) 240 grit (b) 400 grit (c) 800 grit

Figure B.3: Water droplets on sandpaper strips coated with automotive spray

B.4. Observations

From Figure B.1, it is evident that the sandpaper strips do not exhibit superhydrophobicity. More spherical droplets can be seen in Figure B.2b and Figure B.3b, indicating that 400 grit sandpaper and a superhydrophobic coating had the potential to produce droplets as desired. However, the effectiveness of Ultra Ever Dry on flat surfaces and the difficulties in incorporating a layer of sandpaper into the surface manufacturing process led to this idea being dropped.

C

Tests on transparent LISHySs

The transparent samples were printed using the Form 3+ SLA printer. Miniature tiles with spherical and cylindrical cavities were designed on CATIA 3DEXPERIENCE and exported as STL files. After configuring the settings of the print on PreForm, they were printed using Formlab's Clear Resin. The prints were then post-processed using the procedure described in Section 3.4.1.

In order to make the sides of the tile clear, the mini-tiles were sanded with progressively finer grits of sandpaper (800, 1000 and 3000 grit). A wax-based polish (Meguiar's Plast-X Clear Plastic Cleaner & Polish) was then rubbed over them to reveal clearer external faces. After this, they were coated with Ultra Ever Dry. The tiles were subsequently infused with water and then placed in the setup described in Section 4.3.

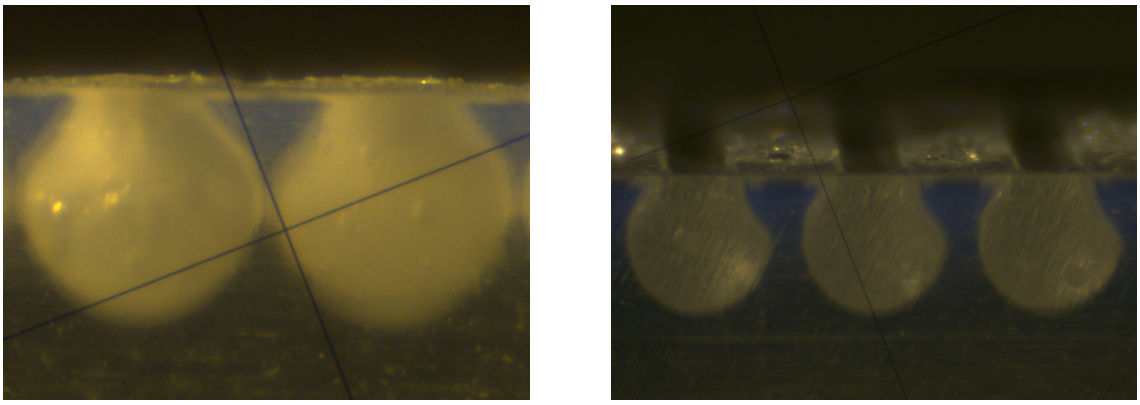

(a) Spherical cavities

(b) Cylindrical cavities

Figure C.1: Miniature transparent tiles viewed through the MAT

Figure C.1 shows images of the tiles as observed from the MAT. Figure C.1a shows that the tile with cylindrical cavities do not have the intended circular cross-section. This is possibly due to the orientation in which the prints were created (at an angle of 45° to the build platform). The spherical cavity tile, as seen in Figure C.1b, shows a more circular cross-section but there is some concavity on the left sides of the cavities near the top surface. In both cases, air pockets appear to be seen inside the cavities. However, when the wind tunnel is started, there is no clearly observable liquid motion visible through the walls of the tiles.


TUDelft
DIMPLE